The Solar Signal in OSIRIS Ozone and Aerosol Measurements

A Thesis Submitted to the
College of Graduate and Postdoctoral Studies
in Partial Fulfillment of the Requirements
for the degree of Master of Science
in the Department of Physics and Engineering Physics
University of Saskatchewan
Saskatoon

By
Kimberlee Dubé

Permission to Use

In presenting this thesis in partial fulfilment of the requirements for a Postgraduate degree from the University of Saskatchewan, I agree that the Libraries of this University may make it freely available for inspection. I further agree that permission for copying of this thesis in any manner, in whole or in part, for scholarly purposes may be granted by the professor or professors who supervised my thesis work or, in their absence, by the Head of the Department or the Dean of the College in which my thesis work was done. It is understood that any copying or publication or use of this thesis or parts thereof for financial gain shall not be allowed without my written permission. It is also understood that due recognition shall be given to me and to the University of Saskatchewan in any scholarly use which may be made of any material in my thesis.

Requests for permission to copy or to make other use of material in this thesis in whole or part should be addressed to:

Head of the Department of Physics and Engineering Physics
116 Science Place
University of Saskatchewan
Saskatoon, Saskatchewan
Canada
S7N 5E2
Or
Dean
College of Graduate and Postdoctoral Studies
University of Saskatchewan
116 Thorvaldson Building, 110 Science Place
Saskatoon, Saskatchewan
S7N 5C9
Canada

Abstract

The intensity of solar radiation reaching the Earth's atmosphere varies over the 25 to 35 day solar rotation period and the 11-year solar cycle. Tropical ozone and aerosol profiles from the Optical Spectrograph and InfraRed Imager System (OSIRIS) are used to investigate the effect of changes in solar ultraviolet flux on stratospheric ozone concentrations and aerosol extinction levels from 2002 to 2015. This time range covers the end of solar cycle 23 and the beginning of solar cycle 24.

A solar rotation signal in the OSIRIS ozone time series is observed above 40 km. The maximum correlation between ozone and solar flux is 0.33 during solar cycle 23 and 0.15 during solar cycle 24. Results from solar cycle 23 were consistent with those from other instruments, confirming the validity of using OSIRIS data to study the effect of solar rotation on stratospheric ozone. This provides a larger data set and insight into the relatively weak solar cycle 24 that can be used in future climate modelling. A clear effect of solar UV irradiance on OSIRIS aerosol extinction levels was not found.

Galactic cosmic rays (GCRs) are thought to affect the aerosol extinction level and aerosol particle size by ionizing the atmosphere to produce more and smaller particles. The effect of GCRs on OSIRIS aerosol parameters was considered by looking at the effect of sudden decreases in the GCRs measured at the Earth called Forbush decreases (FDs). A significant response in the aerosol data to FDs was not observed.

Acknowledgements

I would like to thank...

My supervisors Dr. Adam Bourassa and Dr. Kathryn McWilliams for all of their feedback and assistance throughout this process.

All of the people who have called rooms 312 and 315 home over the past three years for making it fun to show up everyday and for answering my many questions, especially Chris Roth, Daniel Zawada, Landon Regier, and Caelia Gardiner.

My family, Donna, Norbert, and Cameron, for providing constant support and encouragement.

My cat, Texas.

Contents

List of Tables

List of Figures

List of Abbreviations

AERONET	Aerosol Robotic Network
AMSU	Advanced Microwave Sounding Unit
CCN	Cloud Condensation Nuclei
CWT	Continuous Wavelet Transform
ECMWF	European Centre for Medium-Range Weather Forecasts
FD	Forbush Decrease
FFT	Fast Fourier Transform
GCR	Galactic Cosmic Ray
GOME	Global Ozone Monitoring Experiment
HALOE	Halogen Occultation Experiment
ISCCP	International Satellite Cloud Climatology Project
IZMIRAN	Institute of Terrestrial Magnetism, Ionosphere and Radio Wave Propagation
MISR	Multi-angle Imaging SpectroRadiometer
MLS	Microwave Limb Sounder
MODIS	Moderate-resolution Imaging Spectroradiometer
NCEP	National Centers for Environmental Prediction
NOAA	National Oceanic and Atmospheric Administration
OSIRIS	Optical Spectrograph and InfraRed Imager System
QBO	Quasi Biennial Oscillation
SAGE	Stratospheric Aerosol and Gas Experiment
SAMS	Stratospheric and Mesospheric Sounder
SBUV	Solar Backscattered UltraViolet instrument
SCIAMACHY	SCanning Imaging Absorption spectroMeter for Atmospheric CHartographY
SOLSTICE	Solar-Stellar Irradiance Comparison Experiment
SSI	Solar Spectral Irradiance
SSU	Stratospheric Sounding Unit
TSI	Total Solar Irradiance
UARS	Upper Atmospheric Research Satellite
UV	UltraViolet

Chapter 1

Introduction

The Earth's atmosphere is a complex and ever-changing system. Properties like pressure, temperature, and the concentrations of chemical constituents are all intricately linked with one another to control the state of the atmosphere. The lower level of the middle atmosphere, called the stratosphere, is of particular interest when considering variations over climatic time scales. The stratosphere is home to the ozone layer, the main absorber of ultraviolet (UV) radiation from the Sun, and to the stratospheric aerosol layer, which affects climate by modifying the amount of solar radiation that reaches the Earth. Aerosols are currently the largest source of uncertainty in the climate system, and although a large fraction of this uncertainty comes from tropospheric aerosols, the variability in stratospheric aerosols is also an important element. Satellite observations over the past 30 years have made it possible to link changes in the Sun with the amount and size of stratospheric aerosol particles and with the concentration of stratospheric ozone. Further examination and quantification of this connection will allow it to be appropriately included in global climate models. This thesis investigates the connection between solar variability and stratospheric ozone concentration and aerosol extinction using satellite measurements.

Variations in solar irradiance influence the chemistry of the atmosphere. Solar radiation varies over 11-year and 27-day cycles, with the effect being most pronounced at UV wavelengths. Fluctuations in the amount of solar UV radiation are caused by changing activity levels on the Sun. The Sun goes through an 11-year cycle in the number of sunspots: periods with more sunspots correspond to higher activity levels and an increase in emitted radiation. The sunspots rotate with the Sun and are directed towards the Earth approximately every 27 days, resulting in a nearly month-long periodicity within the 11-year solar cycle. Solar radiation is measured directly by satellite instruments and is also quantified by ground and

space based proxies.

One of the main effects of changing solar radiation on the atmosphere is observed in the ozone layer. Ozone is produced when the photolysis of molecular oxygen (O_2) at UV wavelengths releases two oxygen atoms that can each combine with other oxygen molecules to form ozone. It is through this process that an increase in solar UV radiation during periods of high solar activity results in an increase in the observed ozone density. The relatively weak solar magnetic field during periods of low activity allows more galactic cosmic rays (GCRs) to reach the Earth's atmosphere. It is thought that an increase in GCRs can increase the rate of aerosol formation through increased ionization of the atmosphere.

Information about stratospheric ozone and aerosol is regularly derived from observations taken by satellite instruments. One such instrument, the Optical Spectrograph and InfraRed Imager System (OSIRIS), a Canadian instrument designed and operated at the University of Saskatchewan, has been in orbit and gathering data since 2001. OSIRIS measures solar radiation as it scatters through the atmospheric "limb": the side view of the atmosphere from space. From these measurements it is possible to retrieve profiles of the ozone concentration, aerosol extinction level, and Ångstrom exponent (a measure of particle size) using different parts of the observed spectra. These data products are regularly produced by the OSIRIS operations team at the University of Saskatchewan and distributed to the world-wide community.

Previous studies have looked at the effect of solar variability on stratospheric ozone during solar cycles 21 (March 1976 to September 1986), 22 (September 1986 to August 1996), and 23 (August 1996 to December 2008), as measured by a variety of instruments (e.g., Hood (1986), Hood and Zhou (1998), Dikty et al. (2010)). The ozone is always found to increase during periods of higher solar activity, but the magnitude of the increase varies. These studies found that the percent change in ozone per one percent change in solar flux at 205 nm was calculated as 0.5 during solar cycle 21, 0.4 during solar cycle 22, and 0.2 during solar cycle 23. These studies also found that the degree of correlation between the ozone anomaly and a proxy for solar UV flux has changed similarly with time. More recently Dikty et al. (2010) and Bossay et al. (2015) have used Fourier and Wavelet analysis to search for a solar rotation signal in an ozone time series. Both studies found there was occasionally a signal

with periods from 25 to 35 days, but its existence varied over time.

All earlier works have relied on only three years' of observations, or six in the case of Dikty et al. (2010). OSIRIS provides more than 16 years' of measurements. This is the longest single instrument time series available amongst any satellites observing the stratosphere. The observations cover the declining phase of solar cycle 23 and the majority of solar cycle 24, which presents the opportunity to compare changes in ozone during solar cycle 23 to changes in ozone during solar cycle 24 measured by a single instrument. A portion of the OSIRIS measurements directly overlap with measurements from the SCanning Imaging Absorption spectroMeter for Atmospheric CHartographY (SCIAMACHY) instrument used in Dikty et al. (2010) and the Microwave Limb Sounder (MLS) used in Bossay et al. (2015). The results from these studies are compared with OSIRIS observations and extended to include solar cycle 24, which has not been examined elsewhere.

All existing studies of the solar influence on aerosol have focused on the effect of a sudden decrease in GCR flux (called a Forbush decrease) on clouds in the troposphere. It is possible that the effect of a Forbush decrease could also be observed on aerosols in the stratosphere. This is a more direct connection, as it does not rely on the derivation of any cloud parameters. Theoretically a decrease in particle nucleation due to a decrease in GCRs would result in a decrease in aerosol optical depth and an increase in the particle size. A cursory analysis is applied to the OSIRIS aerosol extinction data to see if a solar signal exists. The effect of GCRs on aerosol extinction and particle size is investigated by looking for the signature of Forbush decreases in the OSIRIS aerosol profiles. There has been some debate over whether or not GCRs actually produce a noticeable effect on clouds and aerosol particles, so the goal is to provide further evidence to one side of the conversation.

Chapter 2 contains details regarding solar activity and the chemistry and processes that govern ozone and aerosol in the stratosphere. It also provides further detail on relevant previous studies and the analysis techniques that are to be used. Chapter 3 includes descriptions of the data sources and initial processing. Chapters 4 and 5 contain the results of the ozone and aerosol analyses, respectively, while in chapter 6 the implications of the results are discussed and a conclusion to the work is provided.

Chapter 2

Background

2.1 Solar Irradiance

Solar radiation originates with the energy produced by nuclear fusion reactions occurring in the core of the Sun. The energy is transferred to the solar surface through radiative transfer and convection (Koskinen, 2011). It is absorbed by the innermost layer of the solar surface, the photosphere, and re-emitted as black body radiation. This is the source of the visible radiation we see at the Earth (Liou, 2002). The next layer of the solar atmosphere is the chromosphere. The chromosphere absorbs radiation emitted by the photosphere. This radiation excites atoms in the chromosphere to produce the solar spectrum, including the calcium and magnesium absorption lines that are commonly used as proxies for the solar activity level (Liou, 2002).

Solar irradiance variability arises from fluctuating activity levels within the Sun. An active Sun is defined by surface features like sunspots and faculae in the photosphere, and plages in the chromosphere. Sunspots are dark regions with high magnetic flux. The strong magnetic field inhibits convection from within the Sun, resulting in cooler, dark spots (Koskinen, 2011). Faculae are bright, higher temperature areas found near sunspots, while plages are bright regions in the chromosphere that overlay the photospheric sunspots (Fröhlich and Lean, 2004). While individual sunspots have lifetimes of days to weeks, active regions on the Sun often last for months (Radick, 2004).

The solar cycle is an 11-year cycle in the number of sunspots. It is controlled by the 22-year cycle in the orientation of the Sun's magnetic field (McIntosh et al., 2014). During periods of low solar activity the Sun has a dipolar magnetic field. Over the course of an 11-year solar cycle the polarity of the magnetic field changes direction, taking 22 years to

return to its original orientation. At the beginning of each solar cycle new sunspots appear at mid-latitudes on the Sun. As the cycle progresses the sunspots are found closer to the solar equator (Koskinen, 2011). The movement of the sunspots is caused by the shifting solar magnetic field. Historically the solar cycle has been quantified by astronomers who would count the number of sunspots. The current solar cycle started in December, 2008: it is the 24th solar cycle since consistent observations began.

The rotation of the Sun can be observed by tracking sunspots, which reappear in the same location approximately every 27 days from the perspective of an observer on the Earth. The exact rotation rate depends on solar latitude due to the transport of angular momentum within the Sun: the rotation rate ranges from 25 days at the solar equator to 35 days at the poles (Thompson et al., 1996).

The darkening effect of sunspots during periods of high solar activity is counteracted by the brightening effect of faculae and plages. The result is a net increase in solar irradiance during the solar cycle maxima (Lean, 1987). This increase in total solar irradiance (TSI) from solar minimum to solar maximum was found to be on the order of 0.1% over each of solar cycles 21, 22, and 23 (Fröhlich, 2013). TSI is defined as the power per unit area over all wavelengths that is incident on the upper atmosphere (taken to be the average Earth-Sun distance) (Foukal et al., 2006). The variation in irradiance over a solar cycle is more pronounced at shorter wavelengths. This has been observed in measurements of the solar spectral irradiance (SSI), which is the power per unit area for a given wavelength. One study found variations in the irradiance from solar minimum to solar maximum of 20% at 140 nm, 8% at 200 nm, and 3% at 250 nm (Fröhlich and Lean, 2004). Variations in solar irradiance over the solar rotation period decrease similarly as wavelength increases (Brasseur and Solomon, 2005).

TSI has been monitored from space since 1978. Differences in calibration between instruments and degradation within individual instruments has made the production of a composite data set capable of displaying long term trends challenging (Heath and Schlesinger, 1986). This has resulted in the use of both ground and space based proxies for quantifying changes in solar irradiance. The most common proxies are the F10.7 radio flux, the Ca II K line, and the Mg II index.

The F10.7 proxy is determined from measurements of chromospheric radio emissions at a wavelength of 10.7 cm (Tapping, 2013). This emission varies with solar activity and has been measured daily in Canada since 1946. The Ca II K index is based on the singly-ionized calcium absorption line at 393.37 nm. Faculae in the chromosphere produce emissions in the core of the Ca absorption line that vary in magnitude with the level of solar activity (Donnelly et al., 1994). The Ca II K line has been recorded for over 100 years with ground-based measurements at the Mount Wilson Observatory in California (Bertello et al., 2010). The Mg II index is the ratio of emissions in the chromospheric Mg h and k absorption lines at 280.35 nm and 279.63 nm (the core), to peaks in the photospheric flux on either side (the wing) (Heath and Schlesinger, 1986). As with TSI, the Mg II index has been measured by various space borne instruments since 1978. Unlike TSI, the Mg II index is a ratio so it is relatively independent of the instrumentation used. Each of these proxies shows clear 11-year and 27-day modulations.

The Mg II index is the proxy used to represent changes in solar irradiance throughout this work, and it will be described further in chapter 3. It was chosen for being a consistent value measured from space, as well as to match previous studies (e.g. Dikty et al. (2010)). The Mg II index is also the only proxy that directly represents radiation at UV wavelengths, which are the most important when considering effects on the stratosphere.

2.2 Radiative Transfer

As solar radiation travels from the Sun it interacts with molecules in the Earth's atmosphere through the process of radiative transfer. The radiative transfer equation is used to convert the solar irradiance spectra measured by satellite instruments into aerosol extinction and ozone concentration profiles.

Gases and aerosol particles attenuate light through absorption and scattering. Figure 2.1 shows the transmission of light with initial intensity $I_\lambda(s_0)$ through a medium. Over an infinitesimal path length ds the extinction of light as it passes through the atmosphere is

described by the Lambert-Beer law (Petty, 2006),

$$dI_\lambda(s) \equiv I_\lambda(s+ds) - I_\lambda(s) = -I_\lambda(s)\beta_e(s)ds, \tag{2.1}$$

where $I_\lambda(s)$ is the intensity of the light as a function of wavelength λ at location s and $\beta_e(s)$ is a coefficient for the extinction of light through absorption and scattering at location s, $\beta_e(s) = \beta_a(s) + \beta_s(s)$ (Petty, 2006). The extinction coefficient can also be written as $\beta_e(s) = \sigma_e(\lambda)n(s)$, where $\sigma_e(\lambda)$ is the extinction cross section of a species as a function of wavelength and $n(s)$ is the number density of that species at point s. For a mixture of gases the values of $\beta_e(s)$ can be added together (Petty, 2006). The path length ds must be small enough so that $\beta_e(s)$ is constant in the interval $s + ds$.

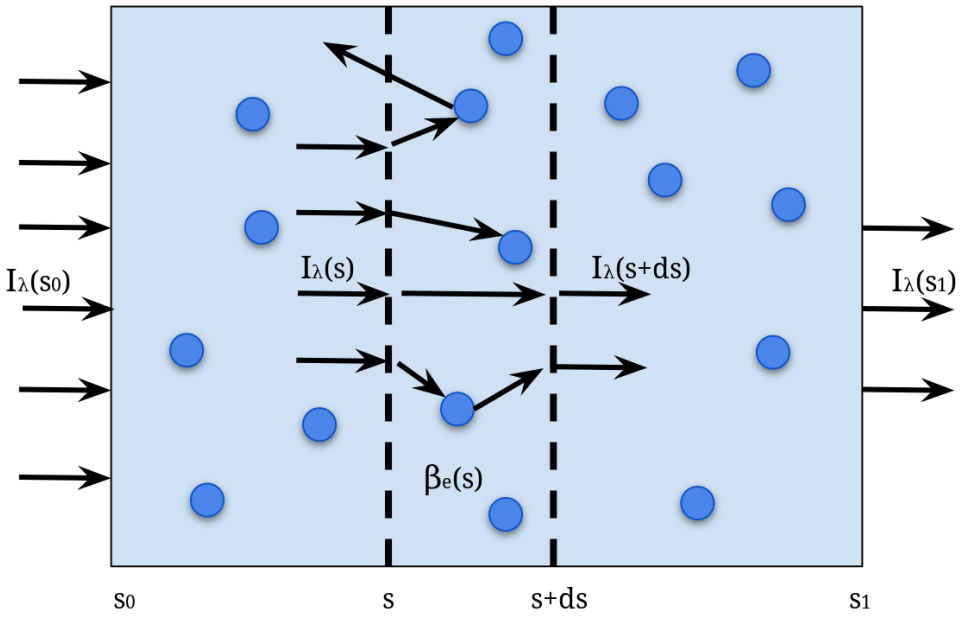

Figure 2.1: Diagram showing the extinction of radiation due to scattering and absorption by particles over a path length ds.

Solving equation 2.1 for intensity gives

$$\frac{dI_\lambda(s)}{I_\lambda(s)} = -\sigma_e(\lambda)n(s)ds, \tag{2.2}$$

$$I_\lambda(s_1) = I_\lambda(s_0)\exp\left(-\int_{s_0}^{s_1}\sigma_e(\lambda)n(s)ds\right). \tag{2.3}$$

The integral is over the region in figure 2.1 from s_0 to s_1. The term inside the exponential is the definition of the optical depth, $\tau(s, \lambda)$,

$$I_\lambda(s_1) = I_\lambda(s_0) \exp(-\tau(s, \lambda)). \tag{2.4}$$

The optical depth is the distance that radiation of wavelength λ can travel along a path before being completely absorbed (Petty, 2006). The optical depth $\tau(s, \lambda)$ depends upon the angle of the incident radiation. Atmospheric density $n(s)$ depends on pressure, which varies with altitude.

It is also necessary to consider emissions into the line of sight ds of the measuring instrument by including a source term $J_\lambda(s)$ in equation 2.1,

$$dI_\lambda(s) = -I_\lambda(s)\beta_e(s)ds + J_\lambda(s)\beta_e(s)ds. \tag{2.5}$$

The complete equation for radiative transfer is

$$\frac{dI_\lambda(s)}{ds} = -\beta_e(s)[J_\lambda(s) - I_\lambda(s)]. \tag{2.6}$$

The source term $J_\lambda(s)$ includes the intensity of blackbody radiation from the Sun and of light that has been scattered into the line of sight.

Equation 2.6 describes the change in intensity of radiation along the line of sight ds due to emission, absorption, and scattering. Solving this equation for a real atmosphere is extremely complex because the solution depends on scattered radiation from multiple directions so the equation must be solved at every point in the atmosphere.

2.3 The Stratosphere and the Ozone Layer

Figure 2.2 shows the temperature profile of the Earth's atmosphere below 65 km. The stratosphere is the region of the atmosphere extending from approximately 15 to 50 km above the surface. The base height of the stratosphere is defined by a temperature inversion, called the tropopause, above which temperature increases with altitude. The stratosphere

contains 90% of the atmospheric ozone, and it is the absorption of solar UV radiation by ozone that creates the temperature inversion. Above about 50 km the density of ozone is inadequate to continue heating the atmosphere so temperature begins to decrease with altitude. This temperature inversion can be seen in figure 2.2. It is called the stratopause, and defines the lower boundary of the next atmospheric layer, the mesosphere.

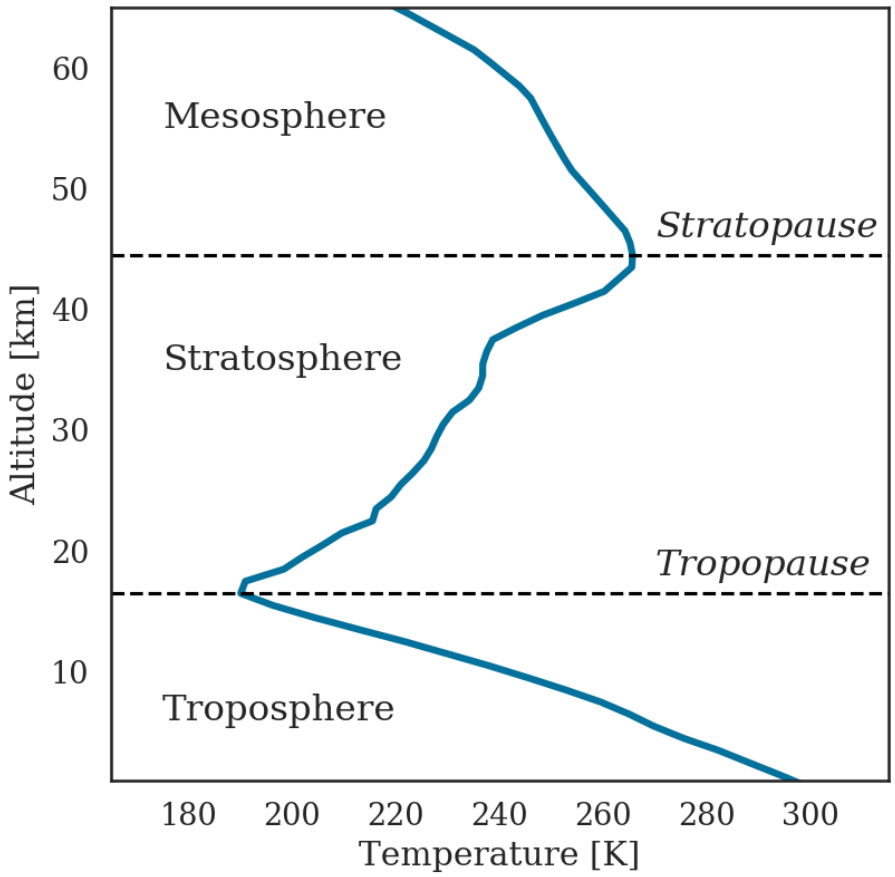

Figure 2.2: Sample atmospheric temperature profile from 1 to 65 km with the regions of the atmosphere labelled. Temperature values from ECMWF.

The distribution of stratospheric ozone is affected by many factors. These include not only the amount of incoming solar radiation, but also the presence of other gases, transport processes, and temperature. This section explores the chemical and physical processes that influence stratospheric ozone concentration so that the effect of solar variability can be isolated.

The chemical life cycle of ozone is controlled by six important chemical reactions. The first four reactions (2.7 to 2.10) produce a closed system called the Chapman cycle (Chapman, 1930). Initially ozone is produced through the photolysis of O_2 by radiation with wavelengths shorter than 242 nm (Brasseur and Solomon, 2005),

$$O_2 + h\nu \rightarrow O + O. \tag{2.7}$$

In chemical equations the term $h\nu$ represents a photon. The rate of oxygen photodissociation depends on both the intensity of incoming radiation and the absorption cross section of the O_2 molecule. The absorption cross section is the probability that a particle will absorb radiation at a particular wavelength. In the case of stratospheric O_2 the most important wavelengths to consider for photodissociation are from 175 to 205 nm (the Schumann-Runge bands) and from 195 to 242 nm (the Herzberg continuum) (Brasseur and Solomon, 2005).

The photolysis of O_2 releases two oxygen atoms that can each react with other O_2 molecules to produce ozone. This reaction requires a collision with a third body M so that energy is conserved,

$$O + O_2 + M \rightarrow O_3 + M. \tag{2.8}$$

The necessity of a third molecule means that reaction 2.8 is more likely to occur at lower altitudes where the density of the atmosphere is greater.

Ozone can be destroyed through photolysis by radiation with wavelengths from 240 to 320 nm (Hartley and Huggins bands) or 400 to 600 nm (Chappuis bands) (Seinfeld and Pandis, 2006),

$$O_3 + h\nu \rightarrow O_2 + O. \tag{2.9}$$

Reaction 2.9 has a minimal effect on the total amount of ozone, especially at lower altitudes, as the products can quickly recombine to produce more O_3. It is nonetheless an important reaction for the stratosphere as ozone absorption of radiation in the Hartley band from 200 to 310 nm and the Huggins bands from 310 to 350 nm is responsible for the heating of the stratosphere (Brasseur and Solomon, 2005).

A more long-lasting form of ozone destruction is the combination of ozone and atomic

oxygen to produce O_2,

$$O + O_3 \rightarrow 2O_2. \tag{2.10}$$

This reaction closes the Chapman cycle: the two O_2 molecules produced by reaction 2.10 can be used by reaction 2.7.

Ozone is also destroyed through reactions with a catalyst X,

$$O_3 + X \rightarrow XO + O_2, \tag{2.11}$$

$$XO + O \rightarrow X + O_2. \tag{2.12}$$

Common catalysts are free radicals such as NO, Cl, Br, and OH. These molecules destroy both O and O_3 without being depleted themselves. They are the most important factor contributing to long term ozone loss (Brasseur and Solomon, 2005).

Variations in solar irradiance over both the solar cycle and the solar rotation period are more pronounced at shorter wavelengths. It is therefore expected that the photodissociation of O_2 by radiation with wavelengths less than 242 nm and subsequent production of O_3 (reactions 2.7 and 2.8) will have a larger response to changes in solar irradiance than the photodissociation of ozone by wavelengths longer than 240 nm (reaction 2.9). This will result in an increase in the ozone concentration during periods of greater solar activity, when the level of UV irradiance is higher. O_2 photolysis occurs at wavelengths from 175 to 242 nm, for which solar radiation varies by up to 10% over the course of a solar cycle (section 2.1).

The temperature in the stratosphere is largely determined by the absorption of radiation at wavelengths from 200 to 350 nm. The irradiance at these wavelengths varies by 8% at 200 nm to 0.5% at 270 nm from solar minimum to maximum. Variations in solar irradiance are negligible at wavelengths greater than 300 nm (Fröhlich and Lean, 2004). Based on this, it is expected that any change in temperature over the solar cycle or solar rotation period would be due to the increase in ozone production and absorption rather than directly from ozone photodissociation (reaction 2.9) as the increase in ozone production is caused by changes in irradiance at shorter wavelengths which vary by greater amounts. Model results from Gray et al. (2009) show that below about 35 km, i.e., in the region of maximum ozone concentration,

increases in temperature from solar minimum to solar maximum are due to greater photon absorption by ozone, while in the upper stratosphere increases in temperature are due to direct heating caused by the increase in radiation.

The stratospheric temperature is also linked to ozone through the temperature dependence of the rates for reactions 2.8 and 2.10. Mlynczak and Solomon (1991) found that reaction 2.8 has a rate proportional to $T^{-2.4}$, which means that an increase in temperature decreases the rate of ozone production. They also found that reaction 2.10 has a rate proportional to $\exp(-1/T)$, which means that an increase in temperature increases the rate of ozone depletion through combination with atomic oxygen. The net effect of this is an anti-correlation between ozone and temperature in chemically controlled regions. Ozone destruction also depends on reactions with catalysts, however including the temperature dependence of these reactions has a minimal effect on the net relationship between ozone and temperature (Brasseur and Solomon, 2005).

Above 30 km the state of the stratosphere is mostly determined by chemical reactions. The effect of solar irradiance on ozone photochemistry should be greatest in this region. At lower altitudes the chemical lifetime of ozone becomes long so the abundance of ozone becomes controlled by transport processes. The Chapman cycle chemistry is less relevant at these lower altitudes so the temperature dependence of reaction rates no longer determines the relationship between temperature and ozone, resulting in a correlation of ozone and temperature below 30 km (Finger et al., 1995).

The majority of ozone production occurs in low latitude regions, i.e., in the tropics, due to the amount of direct solar radiation. Figure 2.3 shows the average stratospheric ozone density during March, 2008. The bright region of high density is the ozone layer. The peak altitude of the ozone layer depends on latitude. The ozone density is greatest at high latitudes in the winter hemisphere. This discrepancy in the expected region of maximum ozone is caused by a circulation process in which air from the tropics rises then flows towards the winter pole and downward (Brewer, 1949; Dobson, 1956). This Brewer-Dobson circulation produces a seasonal cycle in the ozone density at a given latitude.

In addition to general circulation processes, the stratosphere is modulated by the quasi-biennial oscillation (QBO). The QBO is a change in direction of the zonal winds from easterly

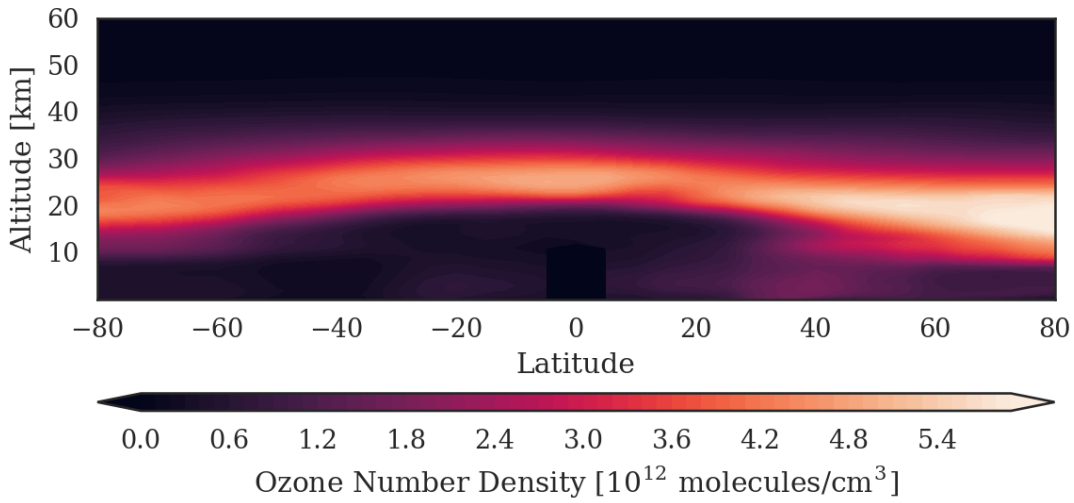

Figure 2.3: Mean ozone concentration as a function of latitude and altitude during March, 2008. Values from OSIRIS.

to westerly that occurs every 22 to 34 months in the lower tropical stratosphere (Baldwin et al., 2001). The QBO signal can be found in both temperature and ozone measurements. The temperature anomaly in the tropical stratosphere caused by the QBO is ±4K, while the variation in column ozone (the total ozone concentration above a point on the Earth) due to the QBO is about 4% (Baldwin et al., 2001). Changes in temperature, ozone, and other atmospheric constituents over the QBO time scale must be taken into account in order to isolate the effect of changes in solar irradiance on the stratosphere.

2.4 The Effect of Solar Variability on Stratospheric Ozone

Past studies have examined the influence of solar variability on stratospheric ozone and temperature during solar cycles 21, 22, and 23. The earliest studies relied on column ozone measurements taken by the Solar Backscatter Ultraviolet Radiometer (SBUV) that operated on the Nimbus-7 satellite from 1978 to 1990, and the multiple SBUV/2 instruments that have been in operation on various National Oceanic and Atmospheric Administration (NOAA) satellites since 1985. More recent studies have made use of the limb instruments

MLS on the Upper Atmospheric Research Satellite (UARS), MLS on Aura, SCIAMACHY, and the occultation instrument the Stratospheric Aerosol and Gas Experiment (SAGE) II. Many of these instruments retrieve ozone concentration on pressure levels instead of altitude levels. Figure 2.4 shows the approximate relationship between pressure and altitude in the middle stratosphere to aid in interpreting the subsequent results. The pressure decreases non-linearly with altitude. The exact pressure at a given altitude changes depending on the air temperature.

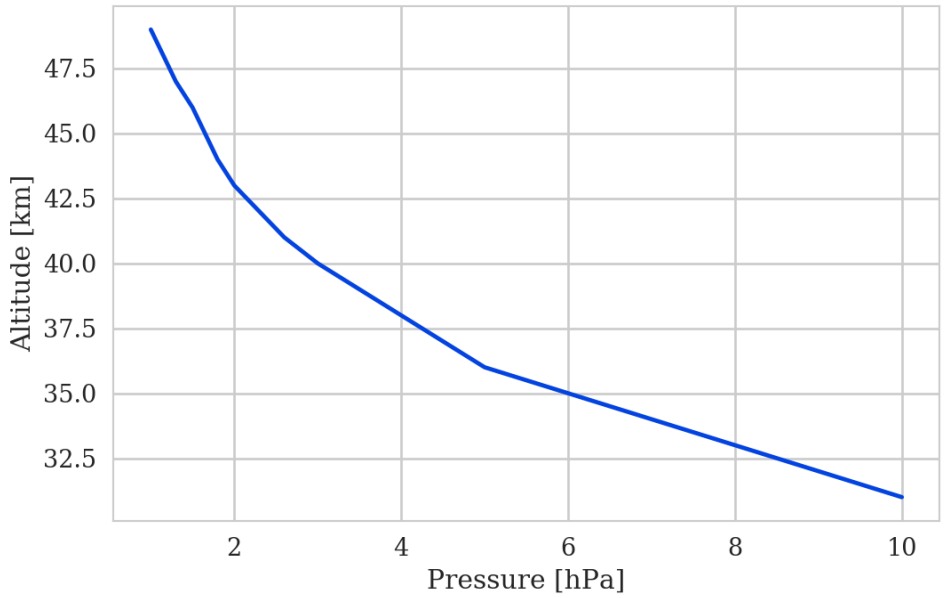

Figure 2.4: Approximate altitude versus pressure in the middle stratosphere. Values from ECMWF.

2.4.1 27-Day Period

Previous analyses of the 27-day period in stratospheric ozone concentration have focused on cross correlations and linear regressions with solar flux. Table 2.1 contains an overview of these results. The linear regression provides the percent change in ozone per 1% change in solar flux: this value is called the sensitivity.

Hood (1986) studied column ozone from SBUV for the period from December, 1978 to October, 1980. The ozone mixing ratio (ratio of ozone density to air density) data for latitudes

Table 2.1: Summary of maximum correlation coefficients between stratospheric ozone and 205 nm flux and sensitivity of ozone to 1% change in 205 nm flux. Values in table do not consider the effect of temperature. The Max. Correlation and Max. Sensitivity values are given along with the altitude at which the maximum occurred.

Study	Period	Solar Cycle	Instrument	Max. Correlation	Max. Sensitivity
Hood 1986	1978-80	21	SBUV	0.6, 3 hPa	0.5, 3 hPa
Zhou 2000	1980-82	21	SBUV/2	0.63, 5 hPa	0.5, 2 hPa
Zhou 2000	1982-85	21	SBUV/2	0.37, 5 hPa	0.55, 2 hPa
Zhou 2000	1989-91	22	SBUV/2	0.61, 5 hPa	0.45, 2 hPa
Zhou 2000	1991-94	22	SBUV/2	0.37, 5 hPa	0.35, 2 hPa
Hood 1998	1991-94	22	UARS/MLS	0.35, 4.6 hPa	0.4, 4.6 hPa
Bossay 2015	1991-94	22	UARS/MLS	0.29, 4.6 hPa	0.4, 4.6 hPa
Dikty 2010	2003-08	23	SCIAMACHY	0.25, 35 km	0.17, 35 km
Bossay 2015	2004-07	23	Aura/MLS	0.16, 6.8 hPa	0.2, 4.6 hPa
Fioletov 2009	1979-2005	21-23	SBUV/2	N/A	0.4, 40 km

from 25°N to 25°S were averaged, smoothed with a 7-day running mean, and filtered with a 35-day running mean. The maximum correlation coefficient between the ozone mixing ratio and solar 205 nm flux (also measured by SBUV) was determined to be 0.6 at an altitude of 3 hPa. The maximum correlation occurred at zero lag, so the solar flux and ozone mixing ratio were in phase. The correlation coefficient was found to be insignificant at latitudes poleward of ±40°. The ozone sensitivity reached a maximum of 0.5%/% at 3 hPa.

Hood and Zhou (1998) analyzed ozone mixing ratios from UARS/MLS averaged over latitudes from 30°N to 30°S for a 1000-day period from October 20, 1991 to July 15, 1994. MLS provides better altitude resolution than SBUV, however night-time measurements are also included in the Hood and Zhou (1998) analysis, which could cause some differences when comparing with other instruments. The ozone mixing ratio was smoothed with a 7-day running mean and filtered with a 35-day running mean. The maximum correlation coefficient with the 205 nm solar flux measured by the Solar-Stellar Irradiance Comparison Experiment (SOLSTICE) on UARS was determined to be 0.35 at zero lag and an altitude of 4.6 hPa. Very low correlations were found above 1.5 hPa. The maximum sensitivity was 0.4%/%

at an altitude of 4.6 hPa. The time series was then divided into two 500-day intervals to analyze separately. The correlation coefficient at 4.6 hPa was 0.25 in the first half and 0.5 in the second half, even though the first 500 days were closer to the solar cycle maximum. Hood and Zhou (1998) also examined temperature measurements from the Stratospheric and Mesospheric Sounder (SAMS). They found a maximum correlation coefficient of 0.2 between temperature and the 205 nm flux at zero lag near 1 hPa in altitude, and a maximum sensitivity of 0.07%/%, also near 1 hPa.

Zhou et al. (2000) investigated SBUV ozone mixing ratios for two 2000-day periods: January 12, 1980 to July 3, 1985 (solar cycle 21) and January 23, 1989 to July 15, 1994 (solar cycle 22). Each of these periods was divided in half for the analysis. Temperature data from the National Centers for Environmental Prediction (NCEP) was used to control for the effect of temperature on ozone chemistry. The ozone and temperature were averaged over latitudes from 30°N to 30°S, smoothed with a 7-day running mean, and filtered with a 35-day running mean. The partial correlation coefficients between the ozone mixing ratio and Mg II index when the effect of temperature was considered were generally greater than the correlation coefficients between ozone and Mg II when temperature was not considered. For example during the first 1000 days of the first analysis period the maximum total correlation was 0.63 at an altitude of 5 hPa, while the maximum partial correlation was 0.79 at 5 hPa. Both of these values had a lag of 3 days (it took 3 days for ozone to reach its maximum response to an increase in UV radiation). All correlations were larger during solar maximum intervals. Zhou et al. (2000) examined the ozone sensitivity with both a linear regression model including only UV flux and ozone, and with a multi-variable linear regression model that also included temperature. The ozone sensitivity to 205 nm flux in the model with temperature was as much as 0.1%/% larger than the ozone sensitivity in the model without temperature at heights from 2 to 5 hPa. The effect of temperature on the ozone sensitivity was larger during periods of lower solar activity.

Results from Dikty et al. (2010) and Bossay et al. (2015) are of main interest to the research presented in this thesis, as the time periods analyzed overlap with the OSIRIS data set. Dikty et al. (2010) examined SCIAMACHY ozone number density profiles from 2003 to 2008. The profiles were averaged from 20°N to 20°S in latitude, smoothed with a

6-day running mean, and filtered with a 35-day running mean. The maximum correlation coefficient with the Mg II index was 0.25 near zero lag and 35 km. The maximum sensitivity to a change in 205 nm flux was 0.17%/% at 35 km. Bossay et al. (2015) used ozone profiles from UARS/MLS during the period of October 1991 to September 1994, and Aura/MLS profiles during the period from September 2004 to August 2007. Profiles were averaged between latitudes of 20°N to 20°S, smoothed with a 7-day running mean, and filtered with a 35-day running mean. The maximum correlation was 0.29 at 4.6 hPa for UARS/MLS, and 0.16 at 6.8 hPa for Aura/MLS. The maximum sensitivities were 0.4%/% and 0.2%/% respectively, both at 4.6 hPa.

The overall result of these studies is that variations in solar flux have been shown to have an effect on stratospheric ozone concentration. However, the magnitude of this effect varies between the studies. Each of the presented studies used six or fewer years worth of ozone measurements from different instruments and solar cycles which makes it difficult to compare the results. Ozone data from the OSIRIS instrument will aid in producing stronger conclusions with regards to the magnitude of the effect of solar irradiance variability on ozone concentration as the OSIRIS data spans over 16 years and overlaps with the ozone measurements from SCIAMACHY and MLS used in Dikty et al. (2010) and Bossay et al. (2015), respectively.

2.4.2 11-Year Period

Although satellite data is only available for a few solar cycles, several studies have looked at the variation of ozone over the 11-year solar cycle. While many of these were modelling studies, this section will focus on works that made use of satellite measurements.

Studies of the 27-day solar rotation period commonly use a 35-day running mean filter to eliminate variations with periods longer than 35 days. Such a filter cannot be used when the period of interest is 11 years long, so variables that affect ozone concentration on longer time scales must be considered in addition to solar flux. McCormack and Hood (1996) used a multi-variable linear regression model to determine the percentage of change in ozone that could be linked to changes in solar UV flux. The model used the Mg II index to represent solar flux. Other terms took into account aerosols, the QBO, and seasonal trends. The ozone

mixing ratios were from the SBUV and SBUV/2 instruments during the years 1979 to 1993. The greatest response of ozone to UV flux was found between 42 and 47 km, with peak values of 5.9% near 40°S and 4.6% near 40°N. These values represent the percent change in ozone from solar minimum to solar maximum. When the ozone response was averaged over all latitudes from 60°N to 60°S the maximum ozone response was 5.5% near 45 km.

Soukharev and Hood (2006) performed a similar regression analysis using ozone measurements from various incarnations of the SBUV and SBUV/2 instruments (1979-2003), the SAGE II instrument (1984-2003), and the UARS Halogen Occultation Experiment (HALOE) (1991-2003). For all instruments the ozone response from solar minimum to maximum was determined to range from 2% to 4% both above 40 km and below 25 km. When the ozone data sets were averaged over from 25°N to 25°S in latitude the response from HALOE ozone was greatest in the lower stratosphere: approximately 5% near 20 km. The maximum response of SAGE II ozone to changes in solar irradiance from solar minimum to maximum was close to 4% from 40 km to 50 km. The maximum response from SBUV ozone was 2.5% near 50 km, which is 3% lower than was found by McCormack and Hood (1996) during their shorter analysis of SBUV measurements.

Fioletov (2009) took a different approach to calculate the ozone response to changes in solar irradiance over a solar cycle. First, the amplitude of the 27-day period was used to determine the ozone sensitivity to a 1% change in the 205 nm solar flux. The ozone data were from SBUV and SBUV/2 during the years 1979 to 2005, covering three solar cycles. The maximum sensitivity was 0.4%/% near 40 km. The increase in the Mg II index from solar minimum to maximum was approximated to be 0.015, corresponding to an increase of 10%. From this, the ozone response over a solar cycle was determined by scaling the 27-day sensitivity (percent change in ozone for a 1% change in solar flux) by the amount of variation in the solar flux over a solar cycle (10% change in solar flux). The resulting ozone change over a solar cycle reached a maximum of 2% near 40 km. This result is comparable to that found by Soukharev and Hood (2006) with SBUV ozone.

These studies show that the maximum variation of ozone over a solar cycle and the altitude at which this maximum occurs are not consistent between studies. OSIRIS provides a single instrument time series covering over one solar cycle. This is long enough to determine

an additional estimate for the percent variation of ozone concentration from solar minimum to solar maximum. The OSIRIS data cover portions of solar cycles 23 and 24, which occurred after the previous studies ended, so an analysis of OSIRIS data will also show if the solar cycle variation of ozone changes over time.

2.5 Stratospheric Aerosol

An aerosol is a collection of solid or liquid particles suspended in a gas (Hinds, 1999). The particles range in size from nanometres to 10 micrometers. Aerosol particles arrive in the atmosphere through both anthropogenic and natural routes. Anthropogenic sources include biomass burning and combustion reactions, while natural sources include volcanic ash, sea spray, and meteor ablation. Aerosols in the stratosphere live in the Junge layer from 15 to 25 km above the Earth's surface (Junge et al., 1961).

Stratospheric aerosols usually consist of an $H_2SO_4 - H_2O$ solution that is produced through chemical reactions involving COS (carbonyl sulfide) and SO_2 (Brasseur and Solomon, 2005). COS enters the stratosphere through transport from the troposphere, while SO_2 enters the stratosphere primarily through direct injection by strong volcanic eruptions (Kremser et al., 2016). Past volcanic eruptions that are known to have greatly modified the sulfur content of the stratosphere include El Chichón in 1982 and Mount Pinatubo in 1991 (Kremser et al., 2016).

Carbonyl sulfide is primarily broken up in the stratosphere by UV photolysis (Brasseur and Solomon, 2005),

$$\mathrm{COS} + h\nu \rightarrow \mathrm{CO} + \mathrm{S}. \tag{2.13}$$

The sulfur reacts with molecular oxygen to form sulfur monoxide and atomic oxygen,

$$\mathrm{S} + \mathrm{O_2} \rightarrow \mathrm{SO} + \mathrm{O}. \tag{2.14}$$

Sulfur monoxide will most commonly react with molecular oxygen again to form sulfur dioxide,

$$\mathrm{SO} + \mathrm{O_2} \rightarrow \mathrm{SO_2} + \mathrm{O}. \tag{2.15}$$

Sulfur dioxide, either produced through the above set of reactions or directly injected by volcanoes, can be converted into sulfuric acid a few different ways. The most common route is through a reaction with hydroxyl (OH) in the following series of reactions (Brasseur and Solomon, 2005),

$$SO_2 + OH + M \rightarrow HSO_3 + M \tag{2.16}$$

$$HSO_3 + O_2 \rightarrow HO_2 + SO_3 \tag{2.17}$$

$$SO_3 + H_2O \rightarrow H_2SO_4. \tag{2.18}$$

The sulfuric acid can then form liquid aerosol droplets. Otherwise it can be destroyed by photolysis at visible wavelengths by the reaction (Kremser et al., 2016),

$$H_2SO_4 + h\nu \rightarrow SO_3 + H_2O. \tag{2.19}$$

Then the sulfur trioxide can be photodissociated,

$$SO_3 + h\nu \rightarrow SO_2 + O, \tag{2.20}$$

and the sulfur dioxide can be photodissociated by UV wavelengths in the range 200-230 nm,

$$SO_2 + h\nu \rightarrow SO + O. \tag{2.21}$$

Sulfuric acid molecules formed in the stratosphere are supersaturated and will quickly condense into liquid particles. New aerosol particles are then formed through nucleation, often with water. Nucleation is the clustering of molecules either with each other (homogeneous nucleation) or onto an existing surface (heterogeneous nucleation) (Hinds, 1999). The nucleation process is dependent on temperature, particle size, and relative humidity. Homogeneous nucleation with a combination of sulfuric acid and water molecules is the most likely process in the stratosphere (Kremser et al., 2016). Nucleation can also occur when clusters of molecules form around ions, such as those produced in the atmosphere by GCRs. The presence of ions has been found to increase the rate of nucleation, as the electrostatic force between the ion and molecules lowers the amount of energy required for condensation

to occur (Seinfeld and Pandis, 2006). It is through this process that GCRs are thought to affect stratospheric aerosol.

Aerosol particles grow through coagulation and condensation (Hinds, 1999). Coagulation occurs when aerosol particles collide with one another and merge together into a larger particle. The likelihood this will happen depends primarily on the number of particles. Condensation occurs when vapour molecules collide with the aerosol particle and condense into a liquid. Condensation depends on temperature and the level of air saturation. Aerosol particles are lost through evaporation and deposition (Hinds, 1999). Evaporation returns the particles to a vapour phase, decreasing the concentration. Deposition is the removal of particles from the air to a surface. In the stratosphere this is most likely to occur through sedimentation. With sedimentation gravity pulls the particles downwards, which can result in a loss of larger particles to the troposphere.

2.6 Cosmic Rays and Aerosol

GCRs are high energy particles originating outside the solar system. Cosmic rays from interstellar sources are known as primary cosmic rays. When primary cosmic rays enter the Earth's atmosphere they collide with air molecules to produce a "cascade" of secondary particles (Thomas et al., 2014). These particles, called secondary cosmic rays, include muons and neutrons that can be detected by ground-based monitors. The flux of GCRs observed at the Earth is anti-correlated with the solar cycle as the stronger heliospheric magnetic field during solar maximum deflects cosmic rays away from the Earth (Heber et al., 2006).

It has been hypothesized that GCRs can influence the Earth's climate through the ionization of the atmosphere (e.g. Svensmark and Friis-Christensen (1997)). The ions could lead to the nucleation of aerosol particles to act as cloud condensation nuclei (CCN), resulting in an increase in cloud cover. The nucleated aerosols initially consist of a small cluster of molecules, some of which can grow to CCN sizes (10-20μm) though coagulation and condensation (Kirkby, 2007). The most important atmospheric constituents for this process are sulfuric acid and water vapour.

The GCR-cloud connection has been examined during events known as Forbush decreases.

A Forbush decrease (FD) is a sudden decrease in the GCR flux observed at the Earth. They were discovered when Forbush (1938) noticed a decrease in GCR intensity coincident with the appearance of low-latitude aurora. FDs are almost always associated with solar coronal mass ejections. A coronal mass ejection has a strong magnetic field that deflects GCRs, temporarily shielding the Earth. The variation in GCRs during a FD is comparable in magnitude to the variation in GCRs over the course of a solar cycle (Krissansen-Totton and Davies, 2013). It is useful to use FDs to study GCRs and clouds as FDs are short and distinct, so longer term effects that could be causing any variations observed in the climate do not need to be considered. It is predicted that when an FD occurs there will be less ionization of the atmosphere, and therefore less aerosol nucleation and fewer, but larger, CCN. There is still some debate over whether this actually happens.

Studies that found evidence for the GCR-cloud link include those by Marsh and Svensmark (2000), Harrison and Stephenson (2006), and Svensmark et al. (2016). Marsh and Svensmark (2000) examined cloud coverage from the International Satellite Cloud Climatology Project (ISCCP). They found a strong correlation between low altitude cloud coverage and GCRs from 1980 to 1995. Svensmark et al. (2016) looked at cloud parameters from four instruments, including the Ångstrom exponent from the aerosol robotic network (AERONET) and cloud optical thickness from the Moderate-resolution Imaging Spectroradiometer (MODIS). They identified the 26 strongest FD events from 1987 to 2007 and used these events in an epoch analysis. A significant signal was identified in almost every cloud parameter examined, with a delay of 6 to 11 days from the FD. The magnitude of the cloud response was positively correlated to the magnitude of the FD.

Some examples of research that did not find a significant or physical connection between GCRs and clouds are Kristjánsson et al. (2008), Laken et al. (2011), and Krissansen-Totton and Davies (2013). Kristjánsson et al. (2008) used FD events defined as a decrease of 5% below the 90-day mean in neutron counts from Climax, Colorado. They correlated these FDs with various cloud parameters from MODIS, including optical depth and droplet radius. The cloud parameters were selected to be from regions in the Southern hemisphere where there were less likely to be anthropogenic aerosol sources. Overall, the correlations were found to be insignificant, meaning no correlation exists, although the correlation coefficients

were higher during the six strongest FDs. Krissansen-Totton and Davies (2013) chose 14 FD events detected by the Kerguelen neutron monitor and compared them to cloud albedo and cloud height from the Multi-angle Imaging SpectroRadiometer (MISR) instrument on the Terra satellite using correlations and superposed epoch analyses. They did not find any significant results, even when restricting the analysis to the strongest FDs or considering different latitude ranges.

Studies relating GCRs and clouds could be affected by changes in solar irradiance. Laken et al. (2011) noted that because FDs are associated with high levels of solar activity (i.e., times with many sunspots) any observed link between cloud properties could actually be caused by decreases in TSI. They performed a superposed epoch analysis with neutron counts from the Mount Washington neutron monitor, the F10.7 cm flux, TSI, and cloud coverage from the ISCCP. The TSI began decreasing five days before the neutron count started to decrease, which was hypothesized to be because light travels faster than the plasma of the solar wind. The correlation between TSI and GCRs was found to be greater during stronger FDs. These results suggest it might not be possible to discern the effect of GCRs from the effect of TSI on clouds during a FD.

2.6.1 Epoch Analysis and Significance Testing

A superposed epoch analysis consists of identifying multiple instances of some type of event in a dataset and averaging them together to produce a composite event. The goal of the averaging is to remove random background variability that might be obscuring main features of the event (Laken and Calogović, 2013). In order for the averaging to be meaningful it must be assumed that the events are all caused by the same mechanism. In the case of FDs the onset of each FD is identified as a decrease in a daily GCR time series below some threshold value. The data for each event, including a few days before and after the onset, are selected from the GCR dataset and the onset dates are aligned. This results in a matrix where each row is one event, or epoch, and each column represents one day from the event onset (day zero). Each column is averaged together to find the mean GCR value for each day. This average event is the superposed epoch.

A hypothesis test is used to determine whether or not the fluctuations in the superposed

epoch are distinguishable from the background variability. The null hypothesis is that the GCR decrease observed in the superposed epoch is indistinguishable from background variations, while the alternative hypothesis is that the decrease in GCRs is distinct from the background variations. In order to have a statistically significant GCR decrease the null hypothesis must be rejected in favour of the alternative hypothesis.

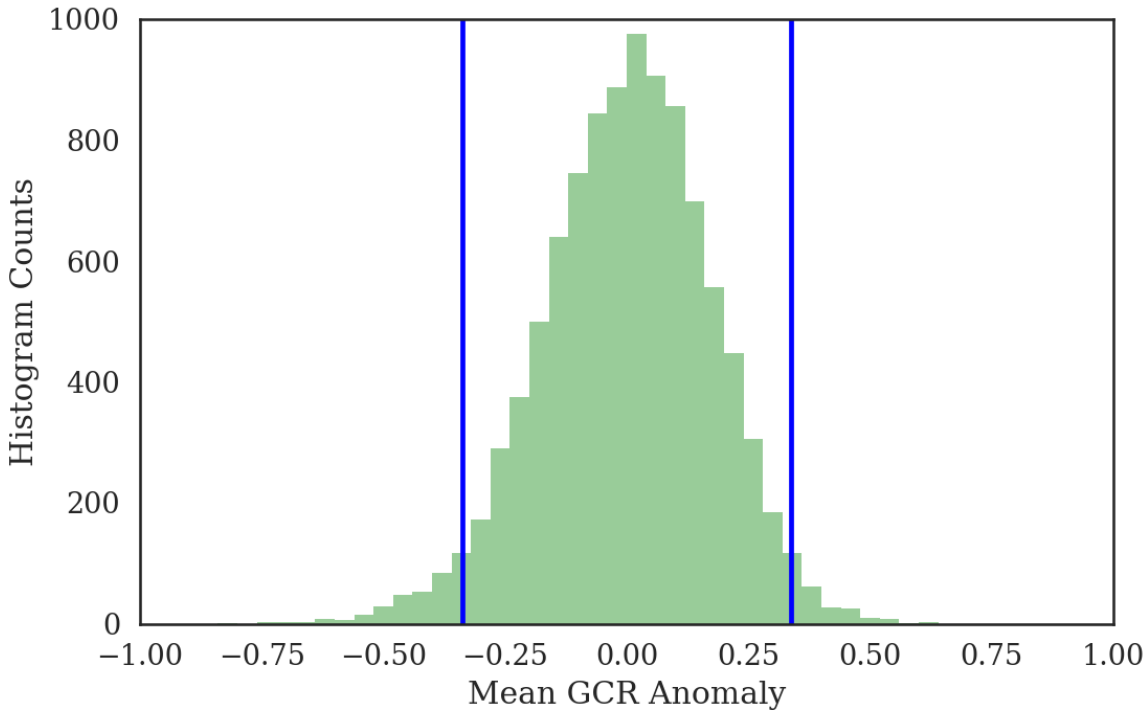

Figure 2.5: Distribution corresponding to average values for a single day after performing 10000 superposed epoch analyses with random GCR data. The blue vertical lines mark the 95% confidence level.

For a superposed epoch analysis Laken and Calogović (2013) suggest testing the null hypothesis using a Monte Carlo method. This method consists of randomly selecting a new set of events from the original data and repeating the epoch analysis on this set. The random event selection and epoch analysis is repeated many times (Laken and Calogović (2013) suggest at least 10000 iterations) to produce a set of mean values for each day in the epoch. A histogram of the 10000 mean values for a given day of the epoch will form a Gaussian probability distribution as long as the random events are independently selected (Rogerson, 2015). As an example, figure 2.5 shows the resulting distribution for one day in

the epoch after 10000 superposed epoch analyses were performed on randomly selected GCR data. The data are close to normally distributed with a mean of zero.

The blue lines in figure 2.5 mark the 95% confidence level. For a Gaussian distribution this corresponds to the means plus or minus 1.96 times the standard deviation (Rogerson, 2015). 95% of the values fall inside this range, while 5% of the values fall outside this range (2.5% on either side of the distribution). The result from the original superposed epoch analysis is compared to this range to test the null hypothesis. If the value falls outside the range the null hypothesis can be rejected in favour of the alternative hypothesis. There is only a 5% chance that the value would fall outside the range under the null hypothesis, so if this occurs the value is said to be significant at the 95% level.

2.7 Signal Processing

Some common signal processing techniques will be used to determine if and how variations in solar irradiance affect ozone, temperature, and aerosol in the stratosphere. This section will outline each technique and describe its application to the data used in this study.

2.7.1 Fast Fourier Transform

The Fourier transform decomposes a signal that is a function of time into a signal that is a function of frequency. Period is the inverse of frequency so applying a Fourier transform to any atmospheric time series is a quick way to check for frequencies with periods matching the solar rotation period. For numerical applications it is necessary to use the discrete Fourier transform, which is defined for a signal x_n as

$$\hat{x}_k = \sum_{n=0}^{N-1} x_n \exp\left(\frac{-2\pi i n k}{N}\right) \tag{2.22}$$

where k is an index representing discrete frequency values from 0 to $N-1$, i is the imaginary number, N is the signal length (number of elements in the time series), and n is the summation index, which in the case of a time series represents time. For a signal with a time step of one day the Fourier transform will have units of inverse days. The signal power is calculated as

$|\hat{x}_k|^2$ and is normalized through division by the signal length N (Press, 1988).

The frequencies corresponding to the values of the discrete Fourier transform depend on the signal spacing d and the signal length N. The signal spacing is the inverse of the sample rate, which is the number of measurements per unit time. The definition of the Fourier transform requires the sample rate be constant. For a real valued signal and an even-numbered signal length the frequencies are

$$f = [0, 1, 2, ..., (N/2) - 1, N/2]/Nd. \tag{2.23}$$

For an odd-numbered signal length the frequencies are

$$f = [0, 1, 2, ..., ((N-1)/2) - 1, (N-1)/2]/Nd. \tag{2.24}$$

In both cases there are $(N/2) + 1$ values corresponding to all of the positive frequencies associated with the signal.

The fast Fourier transform is an algorithm developed by J.W. Cooley and J.W. Tukey for efficient computation of the discrete Fourier transform (Press, 1988). It relies on the fact that a Fourier transform of N values can be written as the sum of the Fourier transforms of the odd and even elements to decrease the computation time (Press, 1988). The fast Fourier transform is used in the analysis to efficiently search for the presence of periodicities near the solar rotation period in ozone, aerosol, and temperature time series.

2.7.2 Continuous Wavelet Transform

The continuous wavelet transform (CWT) is used to show how a one dimensional signal varies in both the frequency and the time domains. This can be more useful than a Fourier transform as the CWT will show the dominant frequencies within a time series and how those frequencies evolve over time. This makes it possible to see if the solar rotation period is present in a data set only at certain times, for example during solar maximum. For an evenly sampled time series x_n the CWT is defined as the convolution between x_n and the

complex conjugate of a scaled wavelet $\psi(\eta)$,

$$W_n(s) = x_n * \psi(\eta) = \sum_{m=0}^{N-1} x_m \psi^* \left(\frac{(m-n)d}{s} \right). \tag{2.25}$$

In equation 2.25 η is the time parameter, n is the translation of the wavelet in time, s is the wavelet scale, and d is the signal spacing in time. The wavelet scale is related to the signal frequency: a lower scale corresponds to a more compressed wavelet in length, and therefore to a higher frequency. The wavelet transform is calculated for a series of predetermined scales. For ease of computation Torrence and Compo (1998) suggest using scales that are powers of two,

$$s_j = s_0 2^{j\delta j}, j = 0, 1, 2, ..., J \tag{2.26}$$

where s_0 is the smallest scale, j is an index from 0 to the largest scale J, and δj is the spacing between scales. These values are chosen through trial and error to find the set that gives adequate resolution to the output of the wavelet transform.

An appropriate wavelet must have a mean of zero and be localized in both the frequency and time domains (the infinite sine and cosine functions used in a Fourier transform are only localized in frequency) (Torrence and Compo, 1998). This analysis uses the Morlet wavelet with a dimensionless central frequency of $\omega_0 = 24$. This wavelet was chosen by Dikty et al. (2010) for providing a reasonable compromise between resolution in frequency and resolution in time. The Morlet wavelet in the time domain is

$$\psi(\eta) = \pi^{-0.25} \exp(i\omega_0 \eta - 0.5\eta^2), \tag{2.27}$$

where η is a dimensionless parameter corresponding to the location of the wavelet in time divided by the scale. In the frequency domain the Morlet wavelet is

$$\hat{\psi}(s\omega) = \pi^{-0.25} H(\omega) \exp(-0.5(s\omega - \omega_0)^2), \tag{2.28}$$

where $H(\omega)$ is the Heaviside step function and ω is the frequency (Torrence and Compo, 1998). The wavelet should be normalized so that it can be compared with other wavelet

transforms through multiplication by a factor of $\sqrt{2\pi s/d}$.

The CWT is most efficiently computed by using a Fourier transform and working in frequency space (Torrence and Compo, 1998). The convolution theorem for two functions f and g states that

$$f * g = \mathcal{F}\left[\mathcal{F}^{-1}(f) \cdot \mathcal{F}^{-1}(g)\right], \tag{2.29}$$

where $\mathcal{F} = \hat{x}_k$ is the Fourier transform given by 2.22 and $\mathcal{F}^{-1}$ is the inverse Fourier transform. By applying the convolution theorem to the CWT equation 2.25 becomes

$$W_n(s) = \sum_{k=0}^{N-1} \hat{x}_k \hat{\psi}^*(s\omega_k) \exp(i\omega_k n d) \tag{2.30}$$

The angular frequencies ω_k are the Fourier frequencies given in 2.23 multiplied by a factor of 2π. The wavelet power spectrum is calculated as $|W_n(s)|^2$.

It is necessary to assume that the input signal is periodic when applying the convolution theorem, however real data are finite and likely not periodic (Press, 1988). Applying equation 2.30 to real data can affect the amplitude of the CWT power spectrum at the edges. The cone of influence is the region in which edge effects must be considered when interpreting the CWT: regions outside the cone of influence might have inaccurate amplitudes. The cone of influence area depends on the length of the signal and the wavelet scale.

The CWT is used in the analysis to examine the time variations of periods similar to the solar rotation period in the ozone, aerosol, and temperature data, as well as in a solar proxy.

2.7.3 Correlation

The goal of correlation is to determine similarities between the variability within two data sets. In the case of cross correlations one data set is shifted relative to the other and the correlation is calculated at each time step, or lag. For two discrete signals f and g that are functions of time t the cross correlation is defined as

$$(f \star g)(t) = \sum_{i=0}^{n} f^*(i) g(i - t) \tag{2.31}$$

where n is the length of the shortest signal and $*$ represents the complex conjugate of $f(i)$. For a completely real signal f, as is the case when using atmospheric data, taking the complex conjugate is not necessary.

In order for the output values of a cross correlation to correspond to the standard Pearson correlation coefficient the input signals must be normalized by subtracting the mean and dividing by the standard deviation (Rogerson, 2015). The Pearson correlation coefficient is a measure of the linear relationship between two data sets. A value of 1 corresponds to the maximum possible correlation (the data sets are linearly related with a positive slope) and a value of -1 corresponds to the maximum anti-correlation (the data sets are linearly related with a negative slope) (Press, 1988). A low correlation coefficient does not necessarily mean the variables are not related, it just means they are not linearly related. A cross correlation is used in the analysis to determine if variations in a solar proxy associated with changes in solar activity also exist in the atmospheric parameters.

2.7.4 Linear Regression

Linear regression is a way to model a system in which a single variable y depends linearly on one or more independent variables $\{x_1, x_2, \ldots, x_n\}$. The linear regression equation is

$$\hat{y} = a_0 + a_1 x_1 + a_2 x_2 + \cdots + a_n x_n + \epsilon \tag{2.32}$$

where $\hat{y}$ is the modelled value of y and ϵ is the residual: the difference between the actual value of y and the modelled value, $\epsilon = y - \hat{y}$. Each a_i is a coefficient that defines how the dependent variable $\hat{y}$ changes when the associated independent variable x_i is changed by a unit amount. The goal of a linear regression is to solve for the coefficients. This is achieved by using a least squares method that minimizes the sum of the squared residuals (Devore and Berk, 2012).

When working with time series data the variables y and x_i are vectors containing the

values of that variable at each point in time so equation 2.32 can be written in matrix form,

$$\begin{bmatrix} \hat{y}_1 \\ \hat{y}_2 \\ \vdots \\ \hat{y}_n \end{bmatrix} = \begin{bmatrix} 1 & x_{11} & x_{12} & \cdots & x_{1m} \\ 1 & x_{21} & x_{22} & \cdots & x_{2m} \\ \vdots & \vdots & \vdots & \ddots & \vdots \\ 1 & x_{n1} & x_{n2} & \cdots & x_{nm} \end{bmatrix} \begin{bmatrix} a_0 \\ a_2 \\ \vdots \\ a_m \end{bmatrix} + \begin{bmatrix} \epsilon_1 \\ \epsilon_2 \\ \vdots \\ \epsilon_n \end{bmatrix} \tag{2.33}$$

where time is going from 1 to n and the number of independent variables is going from 1 to m. The coefficient a_0 and the column of ones represent the y-intercept of the linear equation.

In the subsequent analysis each time series is filtered to remove any trends with periods greater than 35 days. This allows ozone, for example, to be modelled as depending solely on solar flux, S. In that case equation 2.32 can be written simply as

$$[O_3] = a_0 + a_1[S] + \epsilon. \tag{2.34}$$

The sensitivity of ozone to changes in solar flux is given by the parameter a_1.

Ozone chemistry has a strong temperature dependence that can also be included in the model, as was done by Zhou et al. (2000), although doing so requires assuming that temperature, T, and solar flux are independent. In this case the regression model is

$$[O_3] = a_0 + a_1[S] + a_2[T] + \epsilon, \tag{2.35}$$

where a_2 is the sensitivity of ozone to changes in temperature.

Chapter 3

Data

3.1 OSIRIS

The OSIRIS instrument was launched on the Odin satellite in February, 2001. Odin is in a Sun-synchronous orbit with an inclination of 97.8° from the equator. In a Sun-synchronous orbit the satellite passes over each point on the Earth at the same local time. The orbit is dawn-dusk so OSIRIS crosses the equator at 6:00 and 18:00 local time (Llewellyn et al., 2004).

OSIRIS looks through the atmosphere in a direction that is tangential to the Earth so the instrument's line of sight is directed through the atmospheric limb. OSIRIS scans the limb from 10 km to 100 km, with a vertical resolution of 1 km. The instrument performs 60 scans per orbit. The optical spectrograph measures the back-scattered radiation at each altitude along the scan at wavelengths of 280 to 800 nm with a spectral resolution of 1 nm (Llewellyn et al., 2004). Figure 3.1 shows an example of the optical spectrograph measurements for four tangent point altitudes. The spectra clearly show the absorption of UV radiation by ozone in the Hartley bands (yellow region) and Huggins bands (pink region). The smoother part of the spectrum at wavelengths greater than 600 nm is used to retrieve the aerosol extinction.

Ozone and aerosol profiles are retrieved from OSIRIS limb-scatter measurements using the SASKTRAN radiative transfer framework (Bourassa et al., 2008). SASKTRAN solves the radiative transfer equation for an atmosphere modelled as a series of homogeneous spherical shells. The model fits OSIRIS measurements to different states of the atmosphere: the set of atmospheric parameters that provide the best fit are the retrieved values. The retrieved ozone parameter is the number density, while the retrieved aerosol parameters are the extinction and the Ångstrom exponent. The Ångstrom exponent relates aerosol extinction to wavelength

and is inversely related to particle size. Figure 3.2 shows the average ozone and aerosol extinction profiles retrieved from OSIRIS measurements in the tropics during June, 2008. The ozone number density has a maximum value near 25 km, while the aerosol extinction is greatest near 15 km.

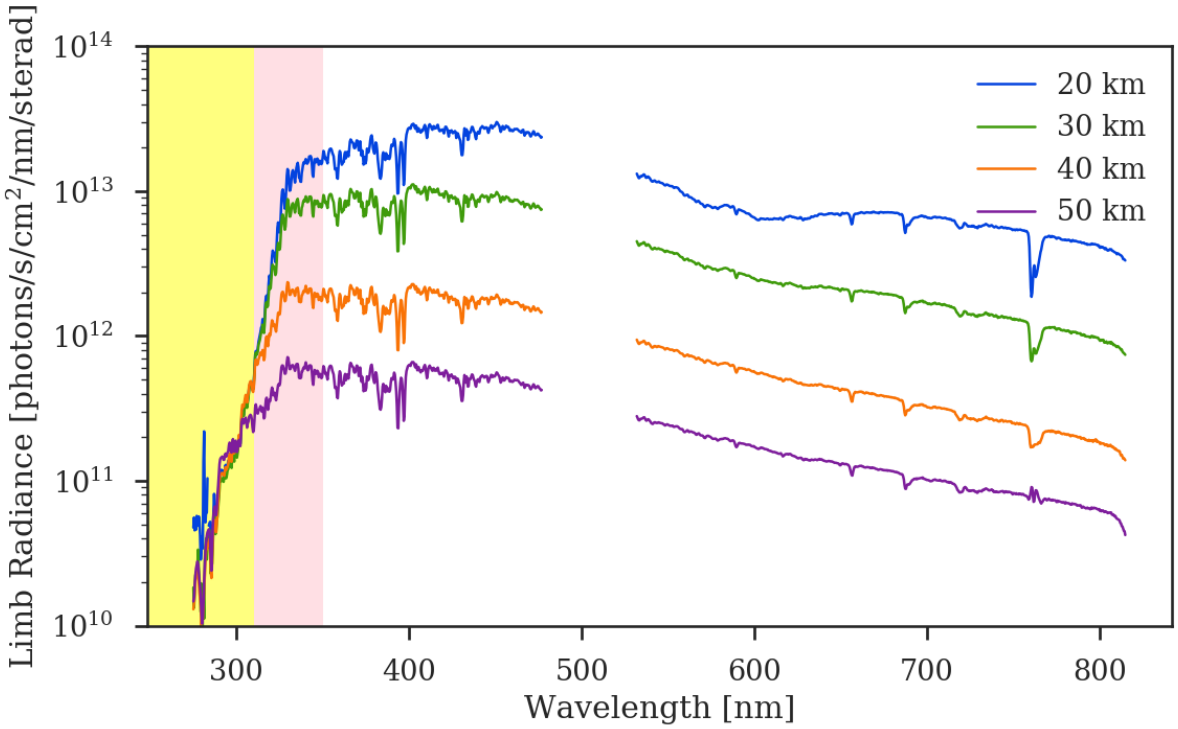

Figure 3.1: Sample of limb radiance measured by OSIRIS at 20, 30, 40, and 50 km. The yellow region marks the Hartley bands and the pink region marks the Huggins bands.

OSIRIS ozone profiles have previously been used to investigate long term trends in the stratosphere. Bourassa et al. (2014) combined OSIRIS measurements with those from SAGE II to produce an ozone time series spanning from 1984 to 2014. They used linear regression to model the variability in the merged SAGE-OSIRIS data set. The regression included variables representing the El Niño southern oscillation, the QBO, the tropopause pressure, and the solar cycle. The solar cycle variation was determined by the F10.7 cm radio flux. The regression model was fitted to the ozone anomaly for different altitudes and latitudes. The QBO is the main source of variability in the tropics, while the solar cycle effect was found to be comparatively small.

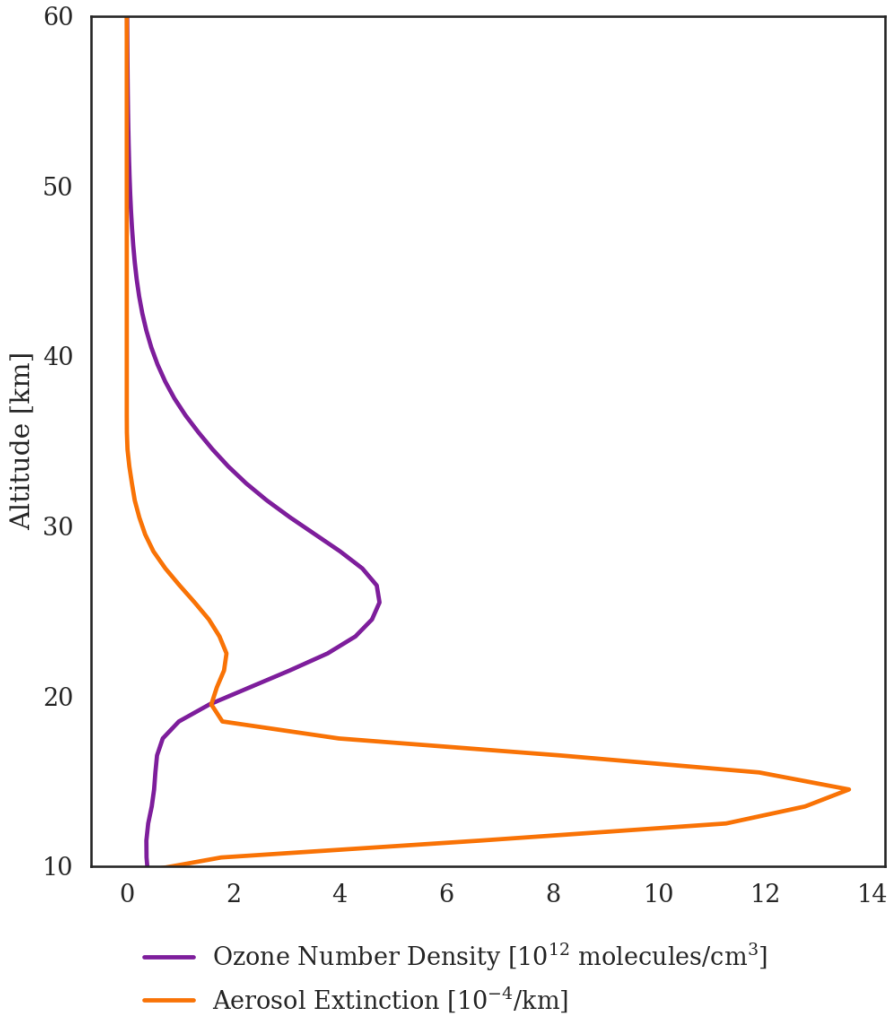

Figure 3.2: Average OSIRIS ozone number density and OSIRIS aerosol extinction profiles in the tropics during June, 2008.

3.2 GOMESCIA Mg II Index

For the purposes of this study solar irradiance is quantified by the GOMESCIA Mg II index. The Mg II index is a proxy for solar irradiance that is derived by comparing the irradiance of the photospheric background (the "wing") to the irradiance of the chromospheric Mg II doublet near 280 nm (the "core"). The GOMESCIA Mg II index is a composite solar proxy containing values from the Global Ozone Monitoring Experiment (GOME), GOME-2A, GOME-2B, and SCIAMACHY (Skupin et al., 2004). Data are available from 1995 to the present day.

GOME was in orbit from 1995 to 2011. It had a spectral resolution of 0.2 nm in the UV range, and measured wavelengths from 240 to 790 nm. An irradiance measurement of the Sun was taken once per day using a diffuser plate (Weber, 1999). The wing was calculated as the mean of the maxima of 4 parabolas fitted through the wavelength ranges 275.79-276.23 nm 276.34-276.79 nm, 282.92-283.25 nm, and 283.69-284.12 nm. The core value came from the integrated intensities of a cubic spline interpolant fit to the magnesium h and k lines at 280.35 nm and 279.63 nm, respectively (Weber, 1999). The Mg II index for a given day was then the ratio of the core to the wing values. Two sample spectra measured by GOME on May 24, 1996 and on December 1, 1998 are given in figure 3.3. The core wavelengths are marked by black dots and the wing wavelengths are marked by arrows. The line at the bottom of the plot is the difference between the two spectra. This shows that while the intensities of the wing wavelengths stays relatively constant, the intensities of the core wavelengths vary with the solar cycle.

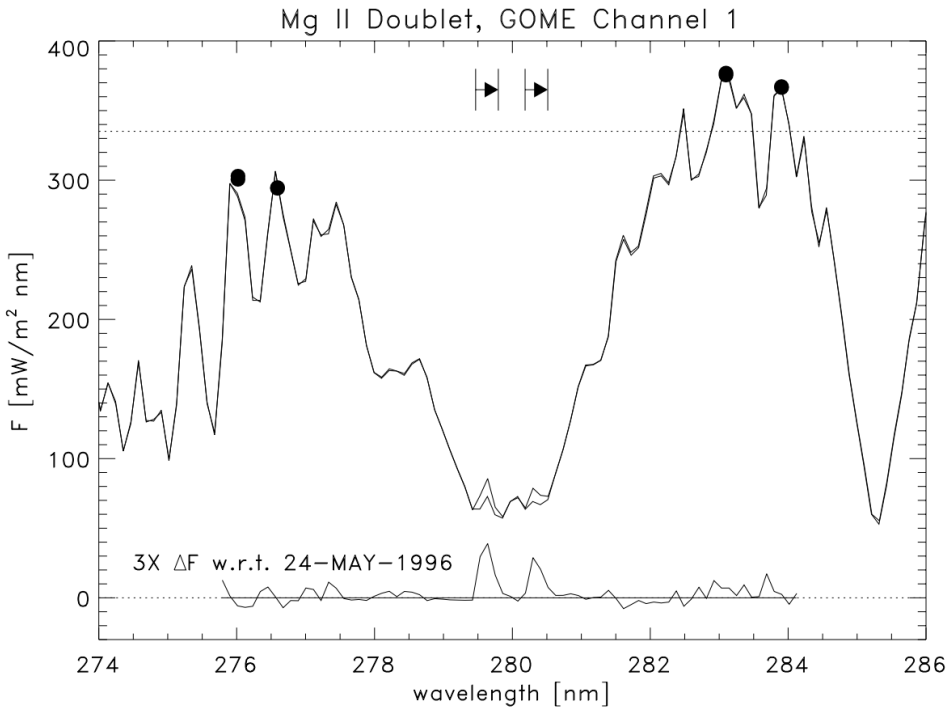

Figure 3.3: The Mg doublet on May 24, 1996 and on December 1, 1998, measured by GOME. The wing values are the black dots and the regions of integration for the core values are shown by arrows. The difference between the two measurements is also shown. Figure 5 from Weber (1999).

Data from SCIAMACHY are available from 2002 to 2012. SCIAMACHY measured wavelengths from 240 nm to 2380 nm with a spectral resolution of 0.2 nm (Skupin et al., 2004). The SCIAMACHY wing values were calculated using the same method described for GOME. The SCIAMACHY core value is the mean of the maxima of parabolas fit to each of the h and k emission lines (Skupin et al., 2004). The Mg II index is once again the core to wing ratio. As with GOME, the index is calculated from daily measurements of the solar irradiance taken with a diffuser plate.

Beginning in 2007 the GOMESCIA index also contains data from GOME-2. GOME-2 has a resolution of 0.3 nm near 280 nm, which is too low of a resolution for the h and k emissions to be resolved (Snow et al., 2014). In order to determine the Mg index the resolution of the data is changed to 1.2 nm by smoothing the spectrum. Then the index is calculated using the equation

$$I = \frac{4(E_{279.8} + E_{280.0} + E_{280.2})}{3(E_{276.6} + E_{276.8} + E_{283.2} + E_{283.4})} \tag{3.1}$$

where each E_i is the irradiance at wavelength i.

The portion of the GOMESCIA Mg II index used in this study is presented in figure 3.4. It covers 14 years, from January 1, 2002 to December 31, 2015. The solar cycle modulation is clearly visible, with a minimum in 2009 coinciding with the solar activity minimum. The high frequency oscillations in the index correspond to the solar rotation period of 25 to 32 days.

3.3 ECMWF Temperature

Stratospheric temperature values are available from the European Centre for Medium-Range Weather Forecasts (ECMWF) ERA-Interim reanalysis. The reanalysis combines observations from a variety of sources with a global forecast model to estimate the state of the atmosphere. The model is constrained by observations: in the case of stratospheric temperature the observations are mainly from the Advanced Microwave Sounding Unit-A (AMSU-A) and the Stratospheric Sounding Unit (SSU) (Uppala et al., 2005). The temperature values are available every six hours for 60 altitudes from 0.01 to 64.5 km (Dee et al., 2011).

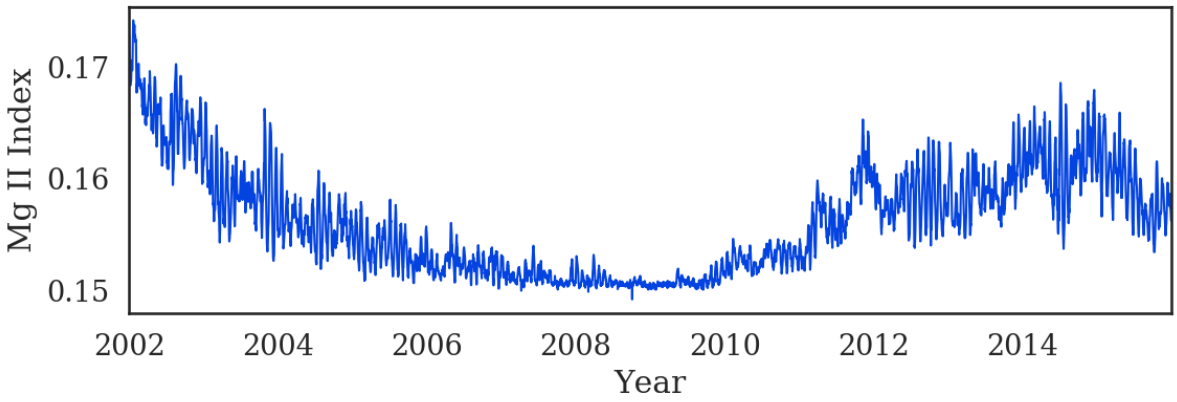

Figure 3.4: The GOMESCIA Mg II index from January 1, 2002 to December 31, 2015.

3.4 Pre-Processing: Solar UV Variability

Each of the temperature, ozone, aerosol, and solar data sets needed some initial processing before any analysis techniques could be applied. The goal of the pre-processing was to deal with gaps in the data and to get the data sets in the same form used by previous studies to allow for direct comparison.

The OSIRIS ozone measurements consist of altitude profiles corresponding to a specific latitude and longitude. The focus of the analysis is the tropics, as that is the region of maximum ozone photolysis and therefore most likely to respond to changes in solar UV irradiance. All measurements from 20°N to 20°S were selected and the daily zonal mean was calculated for profiles of OSIRIS ozone number density from 19.5 km to 60.5 km for each day from January 1, 2002 to December 31, 2015. The anomaly is the difference from the mean value of a time series. It was found at each altitude by subtracting the mean of the ozone density at that altitude. Any values more than 3 standard deviations from the mean were considered to be outliers and removed. Data gaps were filled with linear interpolation. In the later part of the data set there were occasionally gaps of more than a few days that needed to be filled: this would have resulted in a loss of periodicity information that would decrease the magnitude of any signal or correlation values during these times. The resulting time series at each altitude was smoothed with a 6-day running mean to remove small day-to-day

variations. Six days was chosen to match the smoothing used in Dikty et al. (2010). The smoothed ozone anomaly for each day and altitude can be seen in figure 3.5. The alternating regions of positive and negative anomaly are caused by the QBO. An identical processing was applied to the ECMWF temperature and OSIRIS aerosol extinction values. The smoothed temperature anomaly is shown in figure 3.6, while the smoothed aerosol anomaly is given in figure 3.7. Aerosol parameters are only retrieved up to 35.5 km. The high anomalies below 30 km in the aerosol time series correspond to volcanic eruptions.

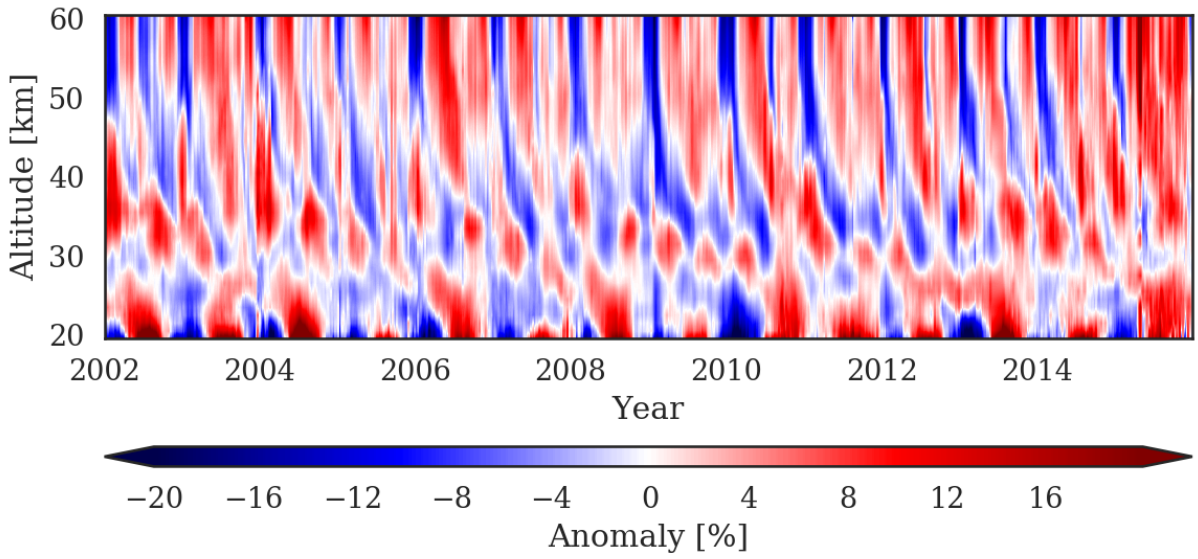

Figure 3.5: The OSIRIS daily zonal mean ozone anomaly from January 1, 2002 to December 31, 2015.

A 35-day running mean was subtracted from the data in order to filter out any signals with periods greater than 35 days. These include the seasonal cycle and the QBO. The 35-day running mean also removes any modulation by the 11-year solar cycle. This filtering makes it easier to detect periods on the order of 27 days. The 35-day filter was used in previous studies, such as Hood (1986), Zhou et al. (2000), and Dikty et al. (2010). Figure 3.8 shows the ozone, temperature, and Mg II anomalies after the subtraction of a 35-day running mean for five altitudes during 2004. The temperature anomaly is multiplied by a factor of 10 so that it can be seen on the same scale as the ozone and Mg II anomalies.

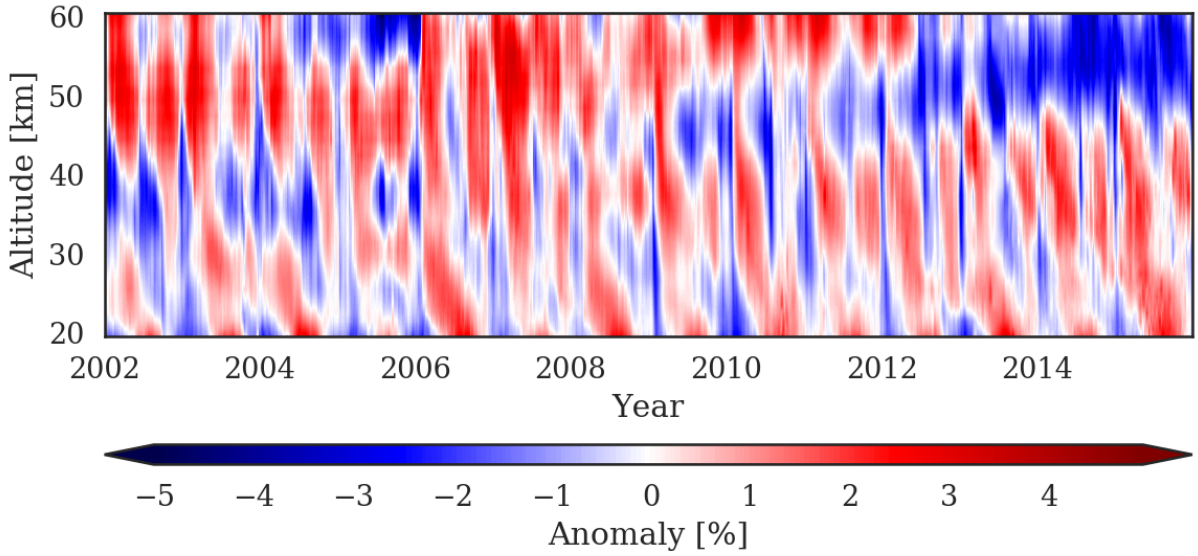

Figure 3.6: The ECMWF daily zonal mean temperature anomaly from January 1, 2002 to December 31, 2015.

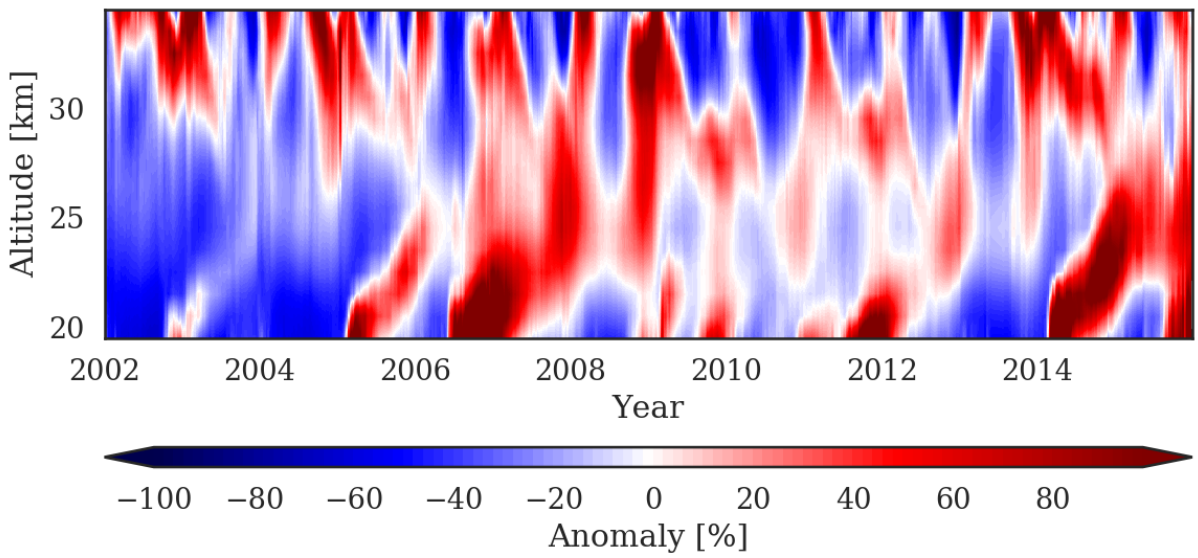

Figure 3.7: The OSIRIS daily zonal mean aerosol anomaly from January 1, 2002 to December 31, 2015.

Figure 3.8 shows that the Mg II index oscillates with a period of about one month. The Mg II and ozone anomalies are sometimes in phase (January to March) and sometimes out of phase (July to August). The period of the oscillation in the ozone anomaly changes with

both altitude and time. The amplitude of the ozone anomaly increases with altitude. The ozone and temperature anomalies are out of phase at all altitudes, as expected (section 2.3). As with ozone, the period of the temperature oscillation varies with time and altitude.

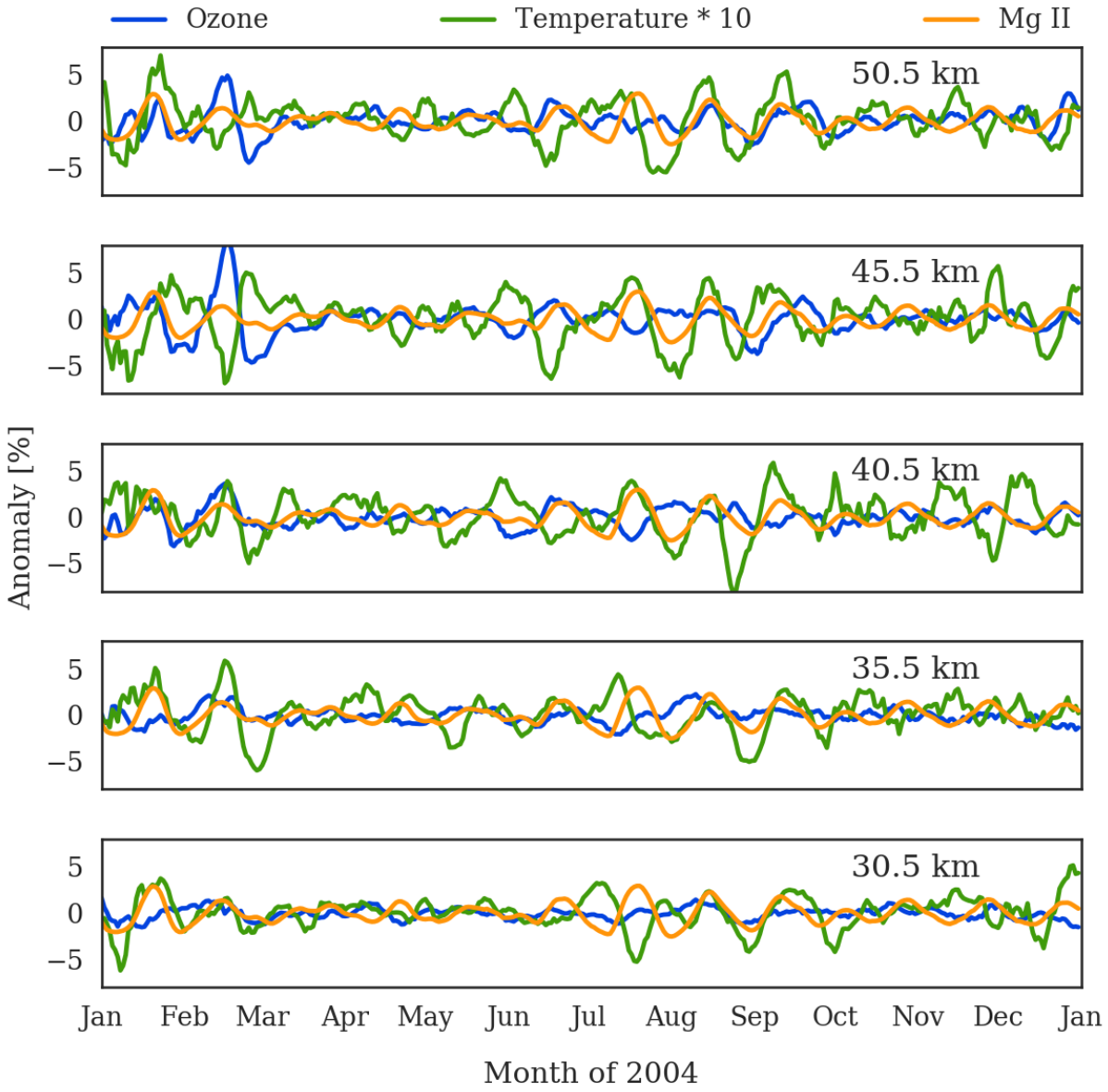

Figure 3.8: The daily mean OSIRIS ozone, ECMWF temperature, and GOMESCIA Mg II anomalies after the subtraction of a 35-day filter at 50.5, 45.5, 40.5, 35.5, and 30.5 km during 2004. The temperature anomaly is multiplied by 10 to be on the same scale as the ozone and Mg II anomalies.

3.5 Cosmic Rays

GCRs are measured by ground-based neutron monitors that count the secondary cosmic rays intercepted by a detector. In order for a secondary cosmic ray to be detected by a neutron monitor it must have an energy above a certain cut-off value- the exact value depends on the geomagnetic latitude of the monitor (Alanko et al., 2003). This cut-off value is called the geomagnetic rigidity. It describes the level of GCR shielding provided by the Earth's magnetic field (Smart and Shea, 2005). The geomagnetic rigidity is a function of the secondary cosmic ray particle's kinetic energy and has units of GeV.

Daily data from the Moscow neutron monitor (IZMIRAN, 2016) were used for comparison with the aerosol parameters. This neutron monitor counts particles with energy from 10 to 20 GeV. The anomaly in the neutron monitor count from 2002 to 2015 was found by subtracting and dividing by the mean. The resulting anomaly values are shown in figure 3.9. The anomaly is higher during periods of lower solar activity (when magnetic shielding is lower), as can be seen when comparing with the Mg II index in figure 3.4. The sharp decreases in the anomaly correspond to strong Forbush decreases.

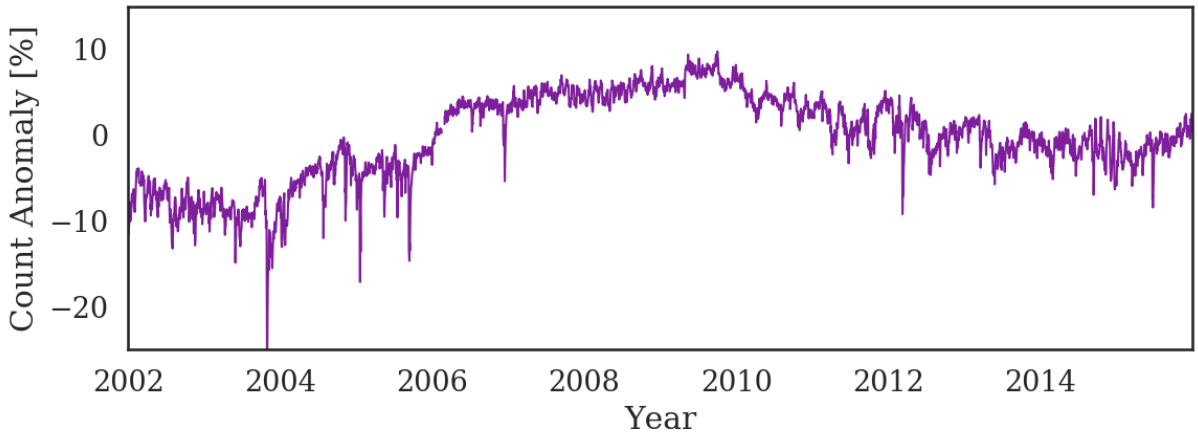

Figure 3.9: Daily mean anomaly in Moscow neutron monitor count from 2002 to 2015 before the application of a high-pass filter.

The 11-year cycle in cosmic rays was removed by the subtraction of a 35-day running mean. Laken and Calogović (2013) used a 21-day filter with an epoch of -20 to 20 days in their study with cloud coverage. As the present work is focused on aerosols, which can take

up to a month to respond to changes in the stratosphere, the epoch was instead chosen to be -14 to 35 days, and a 35-day high-pass filter was applied to the Moscow neutron monitor count so that any shorter signals were not removed. The corresponding OSIRIS aerosol extinction and Ångstrom exponent data were processed in the same way for each altitude from 20 to 35 km. Figure 3.10 shows the resulting aerosol extinction and Ångstrom exponent anomaly time series at 30.5 km. The Ångstrom exponent data are only available until 2012. Both parameters show some oscillation between regions of positive and negative anomaly. There are sharp decreases in both the aerosol extinction and Ångstrom exponent, however both parameters also have sharp increases so these variations cannot be immediately attributed to FDs.

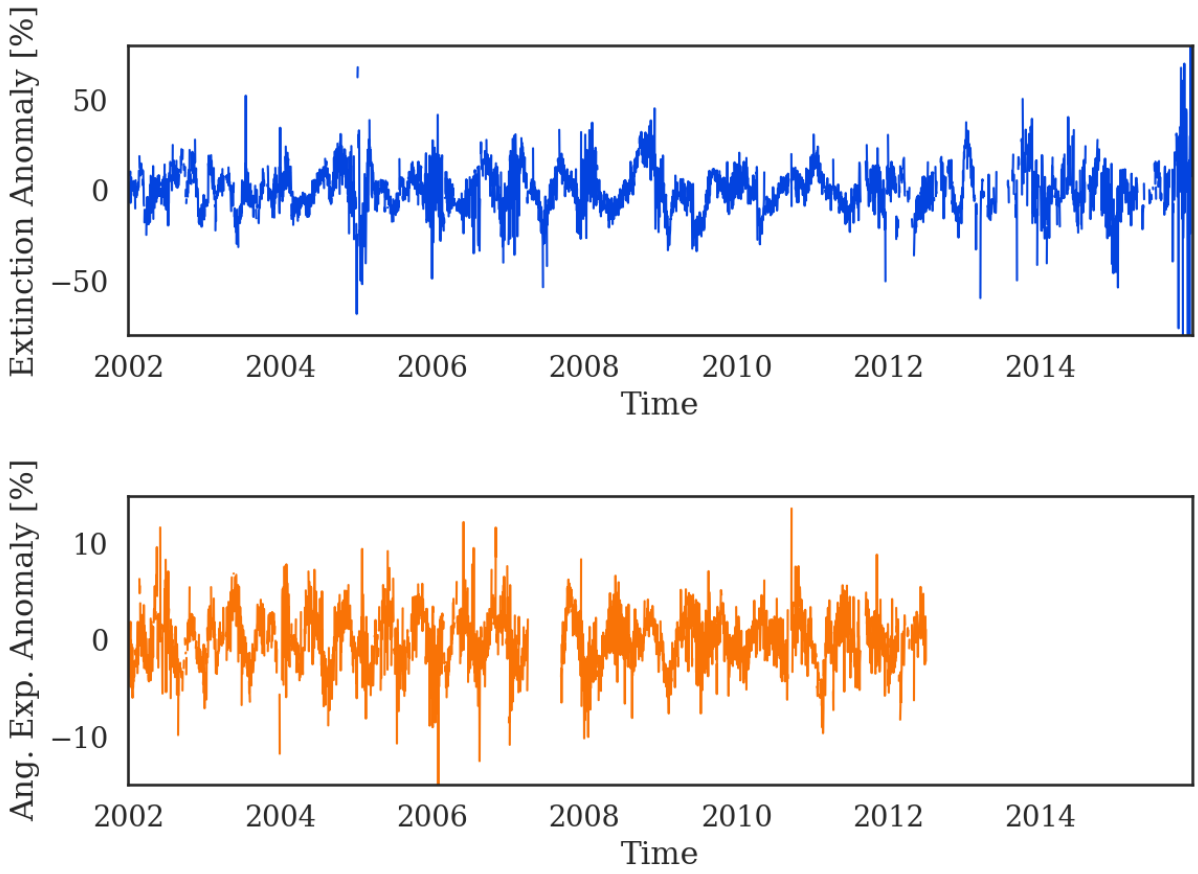

Figure 3.10: Daily mean anomaly in OSIRIS aerosol extinction (top) and OSIRIS Ångstrom exponent (bottom) at 30.5 km after the application of a 35-day high-pass filter.

Previous studies have focused on FDs that occurred before 2006. As OSIRIS began operation in 2002 a list of more recent FDs was desirable. The IZMIRAN (Institute of Terrestrial Magnetism, Ionosphere and Radio Wave Propagation) database was used in order to achieve this (IZMIRAN, 2018). The IZMIRAN database contains a list of FD onset times from 1957 to 2016, along with associated space weather parameters. FDs are classified according to their magnitude, called MagM in the IZMIRAN listings. The magnitude is the maximum cosmic ray variation (difference between maximum and minimum anomalies) during a FD event for particles with 10 GeV rigidity obtained from a global neutron monitor network. Event magnitudes in the IZMIRAN database are as small as 0.4. As was done with previous works such as Laken et al. (2011), a magnitude of at least 3.0 was required for events used in this study.

All events from the IZMIRAN database with a magnitude of at least 3.0 from 2002 to 2015 were identified in the 35-day filtered Moscow neutron monitor count anomaly. Event onset times were shifted so that the maximum decrease was aligned with day zero of the epoch, as was done in most previous studies. While the re-alignment was done automatically, a manual inspection of each event was performed afterwards in order to remove any events containing multiple FDs of comparable magnitude, as these would interfere with the analysis. The resulting list of 45 events from 2002 to 2015 is given in table 3.1. In the table the IZMIRAN onset is the event onset date listed in the IZMIRAN database, the shifted onset is the event onset date corresponding to the maximum decrease in the neutron monitor count, and the IZMIRAN MagM is the event magnitude. The majority of events occurred during periods of high solar activity due to the association between FDs and coronal mass ejections. The largest FD is associated with the well known Halloween storm on October 31, 2003. For the epoch analysis the events were combined into the matrix shown in figure 3.11. Each row in the matrix is one epoch- the event numbers in the figure correspond to the row numbers in table 3.1. Each column is one day of the epoch, from 14 days before the event onset to 35 days after.

A similar event matrix was produced for each altitude of the OSIRIS aerosol extinction and Ångstrom exponent data. The resulting matrix for aerosol extinction at 30.5 km is shown in figure 3.12. There is no consistent decrease in the aerosol extinction anomaly between the

events. Several of the later events are also missing large amounts of data, which will decrease the confidence in the epoch analysis presented in chapter 5.

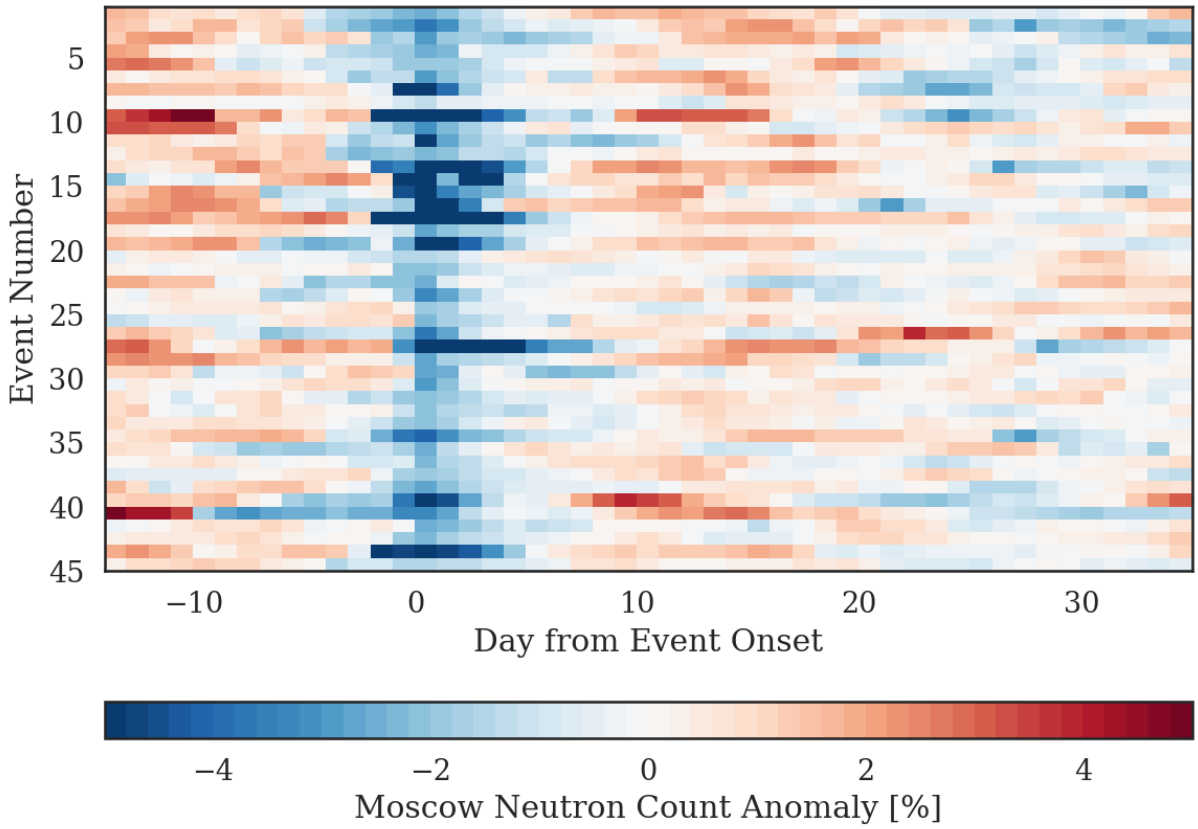

Figure 3.11: Forbush decrease event matrix for Moscow neutron monitor count anomaly. The event number corresponds to the row number in table 3.1.

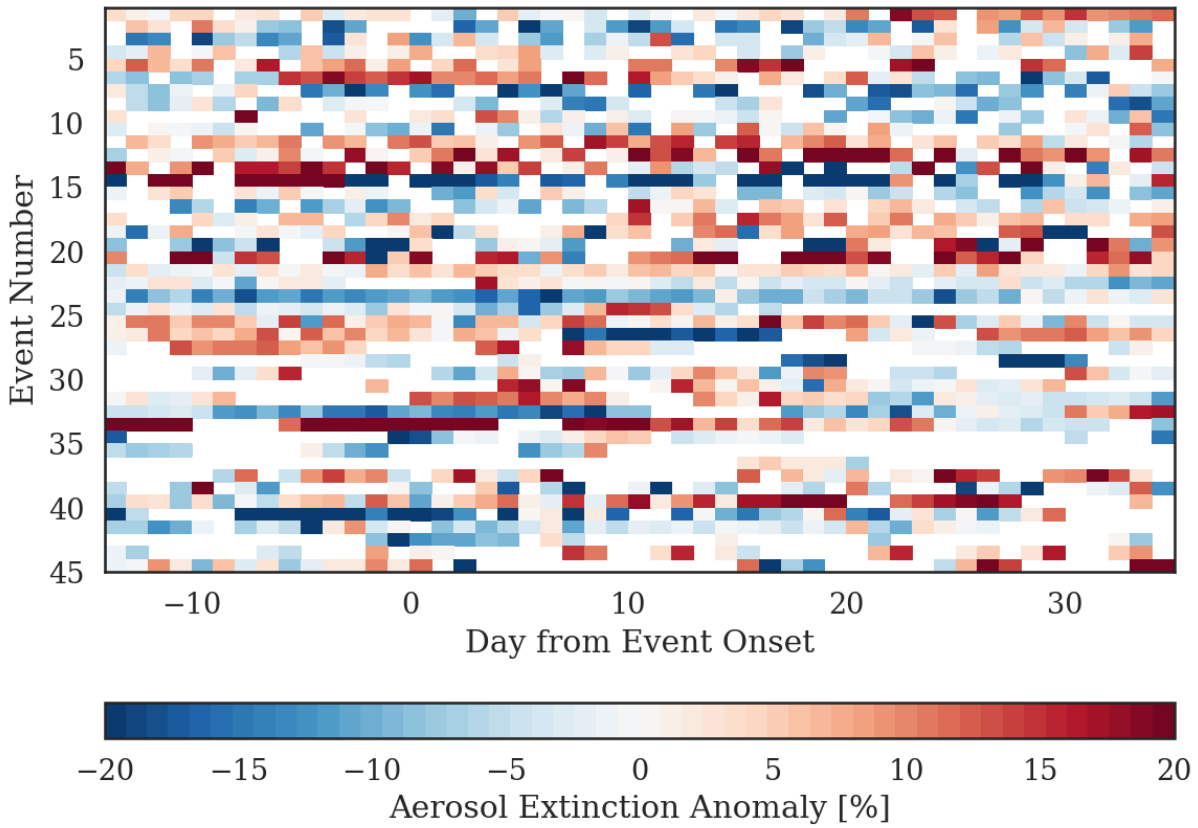

Figure 3.12: Forbush decrease event matrix for OSIRIS aerosol extinction at 30.5 km. The event number corresponds to the row number in table 3.1.

Table 3.1: Forbush decrease events used in the analysis. IZMIRAN Onset is the event onset date listed in the IZMIRAN database, Shifted Onset is the event onset date corresponding to the maximum decrease in the neutron monitor count, and IZMIRAN MagM is the event magnitude given in the IZMIRAN database.

	IZMIRAN Onset	Shifted Onset	IZMIRAN MagM
1	2002-02-04	2002-02-02	3.1
2	2002-03-18	2002-03-24	6.4
3	2002-04-17	2002-04-20	9.2
4	2002-05-23	2002-05-23	9.6
5	2002-08-18	2002-08-28	6.5
6	2003-01-26	2003-01-27	3.3

7	2003-05-29	2003-05-31	9.1
8	2003-08-17	2003-08-18	5.4
9	2003-10-30	2003-10-31	29.7
10	2003-11-20	2003-11-24	13.7
11	2004-07-26	2004-07-27	15.5
12	2004-09-13	2004-09-18	5.6
13	2004-11-09	2004-11-10	10.7
14	2005-01-18	2005-01-19	11.7
15	2005-05-15	2005-05-16	16.4
16	2005-07-17	2005-07-17	4.3
17	2005-09-11	2005-09-13	14.7
18	2006-07-09	2006-07-11	3.9
19	2006-12-14	2006-12-15	12.1
20	2007-01-29	2007-02-16	3.3
21	2010-08-03	2010-08-05	5.1
22	2011-04-11	2011-04-08	3.1
23	2011-06-22	2011-06-24	4.8
24	2011-08-05	2011-08-06	5.2
25	2011-10-24	2011-10-25	8.7
26	2012-01-22	2012-02-01	5.1
27	2012-03-08	2012-03-09	14.8
28	2012-04-04	2012-04-06	4
29	2012-07-14	2012-07-15	10.3
30	2012-09-04	2012-09-05	3.6
31	2012-10-11	2012-10-13	3.7
32	2012-11-23	2012-11-25	4.4
33	2013-01-16	2013-01-20	3.4
34	2013-03-17	2013-03-19	6.7

35	2013-05-31	2013-05-26	3.5
36	2013-07-12	2013-07-13	3
37	2014-04-18	2014-04-20	4.4
38	2014-06-17	2014-06-20	4.3
39	2014-09-12	2014-09-13	7.9
40	2014-12-21	2015-01-01	8.4
41	2015-03-17	2015-03-17	5.4
42	2015-05-06	2015-05-07	3.7
43	2015-06-22	2015-06-25	10.7
44	2015-09-07	2015-09-12	3.2
45	2015-11-06	2015-11-07	5.1

Chapter 4

Results: Ozone and Temperature

The OSIRIS ozone and ECMWF temperature data were analyzed with a variety of signal processing techniques to investigate the existence of a solar rotation signal. The focus was on the 27-day rotation period rather than the 11-year solar cycle, as OSIRIS has only taken one solar cycle worth of measurements. OSIRIS has observed more than 150 solar rotations, so there can be more confidence in any results on that time scale. A FFT was employed as a preliminary test for signals with periodicities near 27 days in each time series. A CWT was used to explore how the signal varied in both the frequency and time domains, making it possible to determine if solar rotation periodicities occurred only during certain times. A cross correlation was applied to determine the similarity of variations in the datasets. The cross correlation was applied to each possible pairing of the OSIRIS ozone, ECMWF temperature, and GOMESCIA Mg II data. Finally, a linear regression was performed to determine the response of ozone to changes in solar flux. The effect of temperature variations was also considered by adding an extra term into the regression model. The linear regression results were used to estimate the variation of ozone over the 11-year solar cycle. All results are presented and discussed in this chapter, as well as compared with the results from previous studies, with a focus on the findings for SCIAMACHY ozone presented in Dikty et al. (2010).

Within the analysis three time periods were considered: 2002-2015, 2003-2008, 2009-2015. The 2002-2015 period contains all the complete years of OSIRIS data that were available at the onset of this project. It is represented by an orange line in relevant plots. The 2003-2008 period was chosen to correspond to the range covered by SCIAMACHY ozone data in Dikty et al. (2010) for the purpose of direct comparison. This period corresponds to the declining phase of solar cycle 23. It is represented by a blue line in the relevant plots. The 2009-2015 period was used to examine how the relation between solar radiation and ozone has changed

since the Dikty et al. (2010) study was performed. It covers the beginning of solar cycle 24 and is represented by a green line in all relevant plots.

4.1 Fourier Transform

The Fourier transform takes a signal in the time domain and transforms it into the frequency domain. This facilitates the study of the fundamental frequencies, and hence oscillation periods, of the signal. The power spectrum resulting from the FFT algorithm applied to the Mg II index for each of the three time ranges is presented in figure 4.1. There are obvious peaks in the signal power at periods ranging from 25 to 30 days, with the maximum signal occurring at approximately 27 days. This matches the expected values for the solar rotation period, and confirms that the Mg II index appropriately represents variations in solar UV flux.

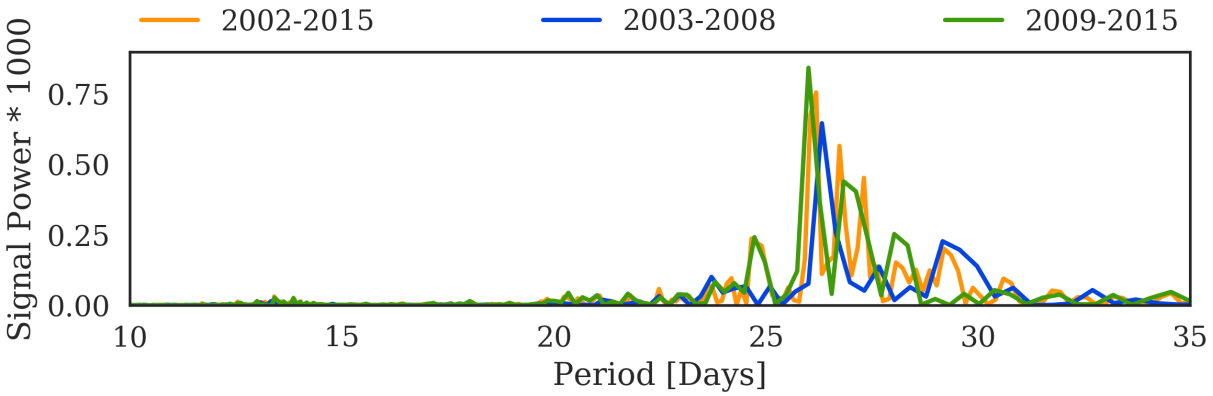

Figure 4.1: Signal power of daily GOMESCIA Mg II index anomaly at periods from 10 to 35 days for three time ranges: 2002-2015 (orange), 2003-2008 (blue), 2009-2015 (green).

The FFT power spectrum of OSIRIS ozone at 30.5, 35.5 km, 40.5 km, 45.5 km, and 50.5 km for the three time ranges is shown in figure 4.2. Each of the time ranges has peaks in the power spectrum with periods corresponding to the solar rotation period at altitudes above 40.5 km. The peaks become more distinct from the background at the higher altitudes. The 2003-2008 period has peaks from 26 to 30 days above 40.5 km. There are also peaks present from 26 to 30 days at lower altitudes, but with weaker signal powers. The 2009-2015 time

range has peaks around 27, 29, and 33 days at 50.5 km. The 2002-2015 period is essentially a combination of the two shorter time ranges so it peaks in the same places.

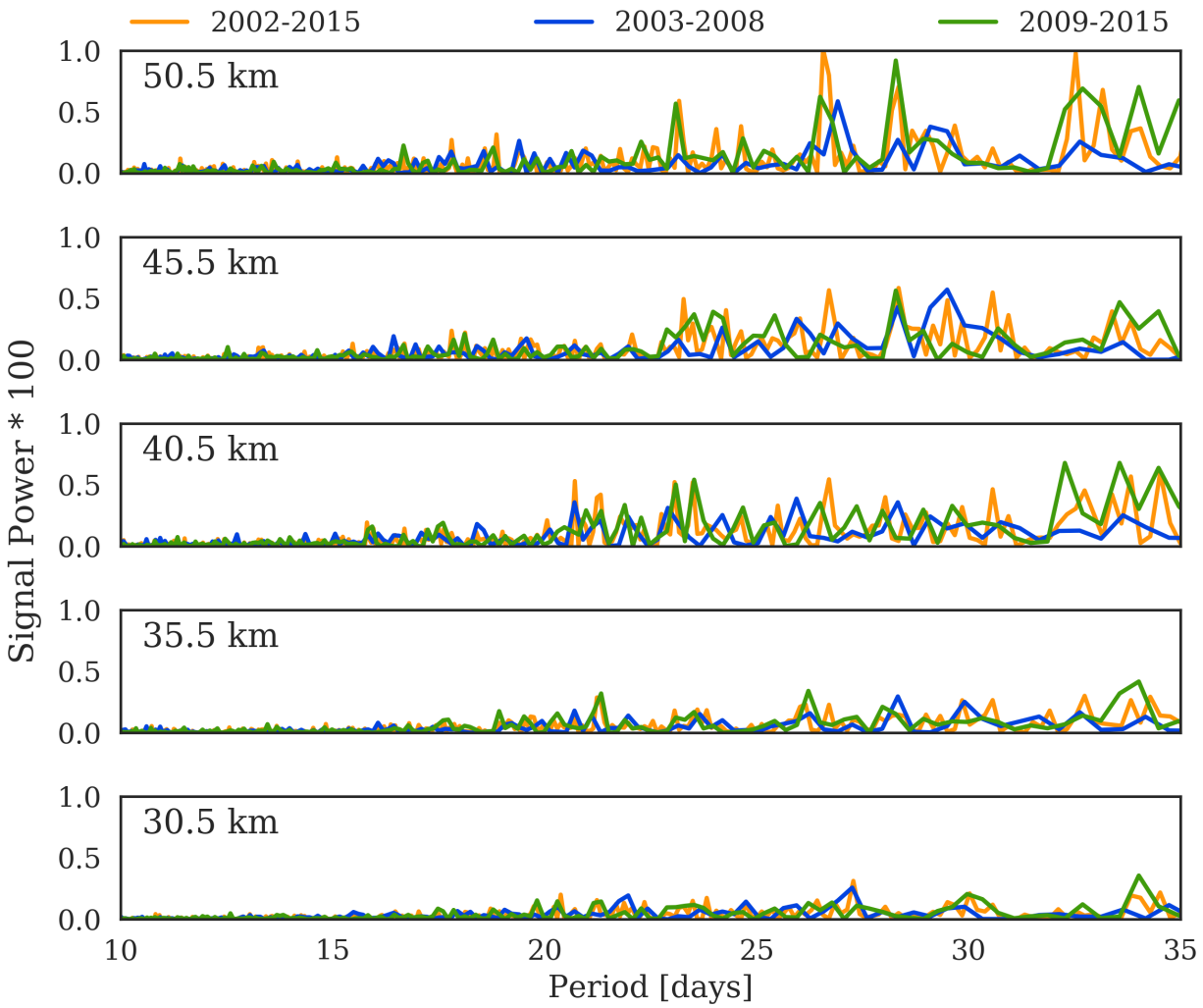

Figure 4.2: FFT power spectrum of daily zonal average OSIRIS ozone at 30.5, 35.5 km, 40.5 km, 45.5 km, and 50.5 km for three time ranges: 2002-2015 (orange), 2003-2008 (blue), 2009-2015 (green).

Dikty et al. (2010) found peaks at 26 and 28 days at 35 km and at altitudes above 45 km in their analysis of SCIAMACHY ozone (top panel of figure 4.3). They also found that there was not one distinct period in the signal, but rather a number of spikes in the range of 25 to 32 days. Overall the FFT power spectrum of OSIRIS ozone data from 2003-2008 is very similar to the FFT power spectrum of SCIAMACHY ozone data for the same years.

The FFT algorithm was also applied to the daily mean ECMWF temperature anomaly-

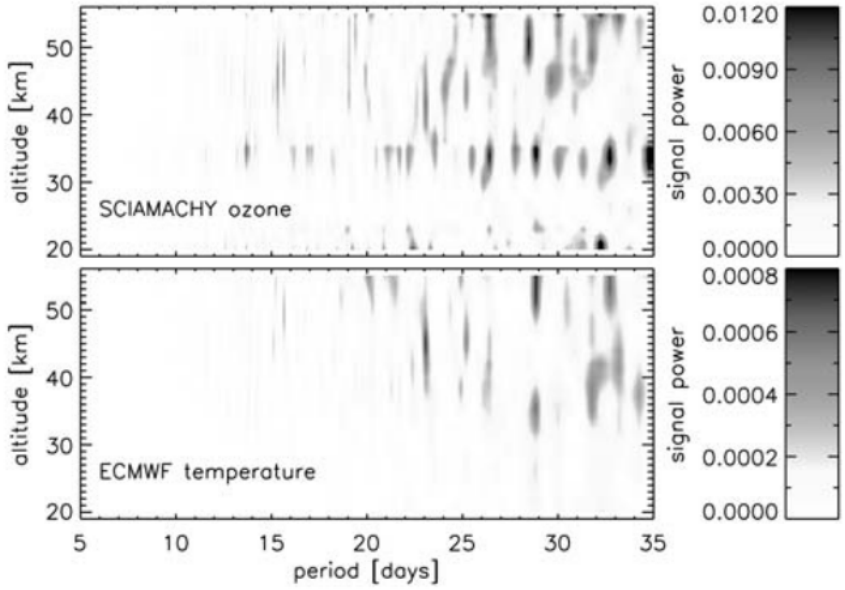

Figure 4.3: FFT power spectrum of daily zonal average SCIAMACHY ozone from 2003-2008 (top) and daily zonal average ECMWF temperature from 2003-2008 (bottom). Figure 4 of Dikty et al. (2010).

the results for five altitudes are presented in figure 4.4. In this case the signal power was more than one order of magnitude smaller than the ozone signal power due to the smaller temperature anomaly. The strongest signals were at 27, 28, 30, and 32 days for all altitudes during the 2009-2015 time range. From 2003-2008 there are peaks at 29 and 33 days, with the strongest signal at 35.5 km. The results should be identical to those from Dikty et al. (2010) as the same ECMWF data were used. Dikty et al. (2010) found peaks at 29 days at 35 km and 50 km, and at 23 days at 45 km (bottom panel of figure 4.3). Each of these peaks also shows up in the blue lines of figure 4.4. This similarity provides verification that the FFT and initial data processing of the OSIRIS ozone data were performed in a manner consistent with Dikty et al. (2010).

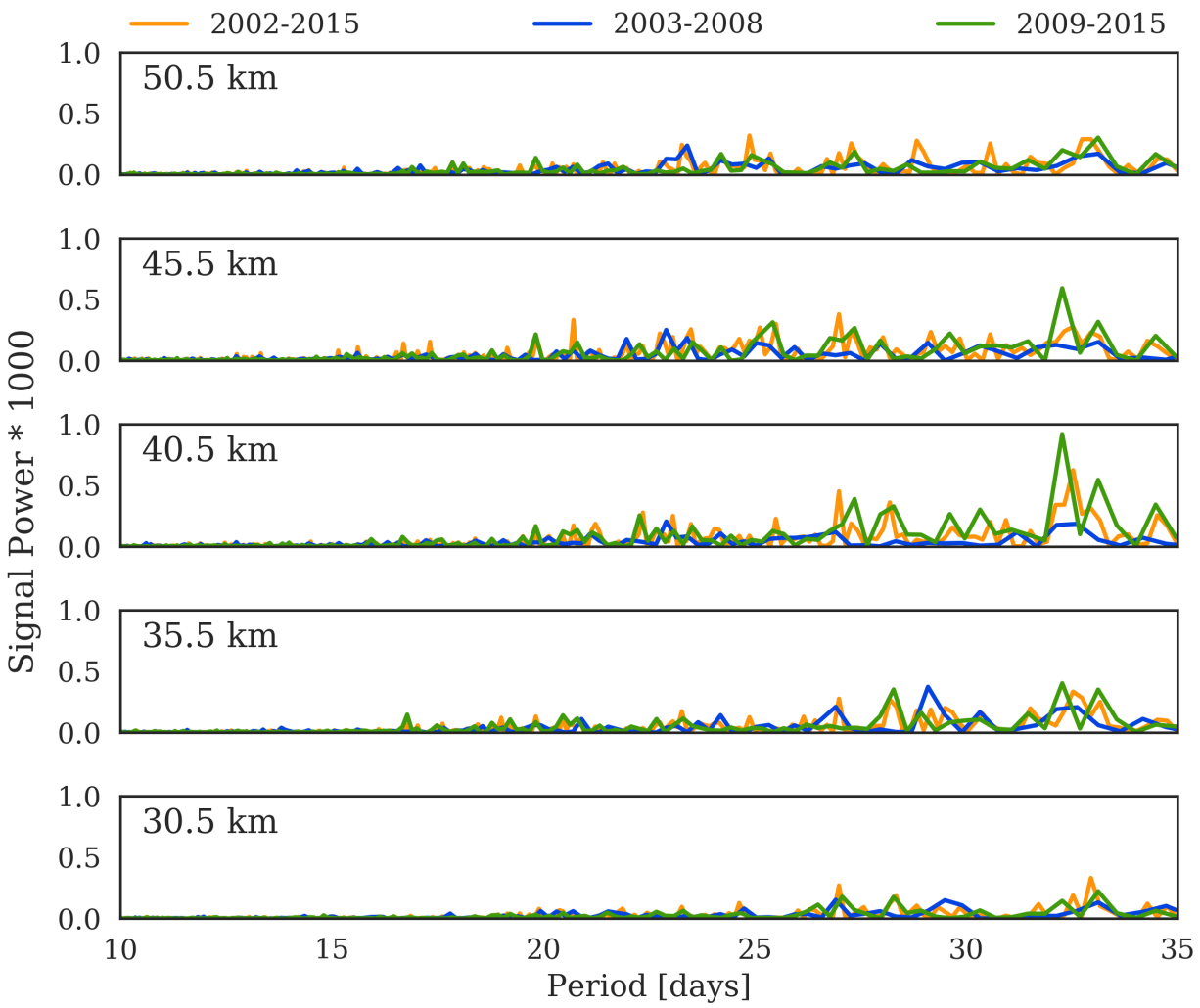

Figure 4.4: FFT power spectrum of daily zonal average ECMWF temperature at 30.5, 35.5 km, 40.5 km, 45.5 km, and 50.5 km for three time ranges: 2002-2015 (orange), 2003-2008 (blue), 2009-2015 (green).

4.2 Continuous Wavelet Transform

A wavelet transform provides more information than a Fourier transform, as the output shows how the frequencies of a signal vary over time. This is useful as the magnitude of any variations on the 27-day time scale are likely to depend on the phase of the 11-year solar cycle. The CWT of the Mg II index is shown in the left panel of figure 4.5. The dashed black lines on either side of the figure mark the cone of influence. Any values outside of these

lines may have an inaccurate signal power. The solid black contour lines represent the 95% confidence level. There is a clear signal with periods from 25 to 32 days during the maxima of solar cycles 23 (2002-2005) and 24 (2012-2015). The right panel of figure 4.5 shows the same power spectrum with each time step normalized to a signal power between zero and one. This normalization allows the 25 to 32 day signal in the Mg II index to be clearly observed at all points in time. The amplitude of the oscillation is much smaller during the solar cycle minimum so the signal power during these years is too low to be visible in the left panel of figure 4.5 with the chosen scale.

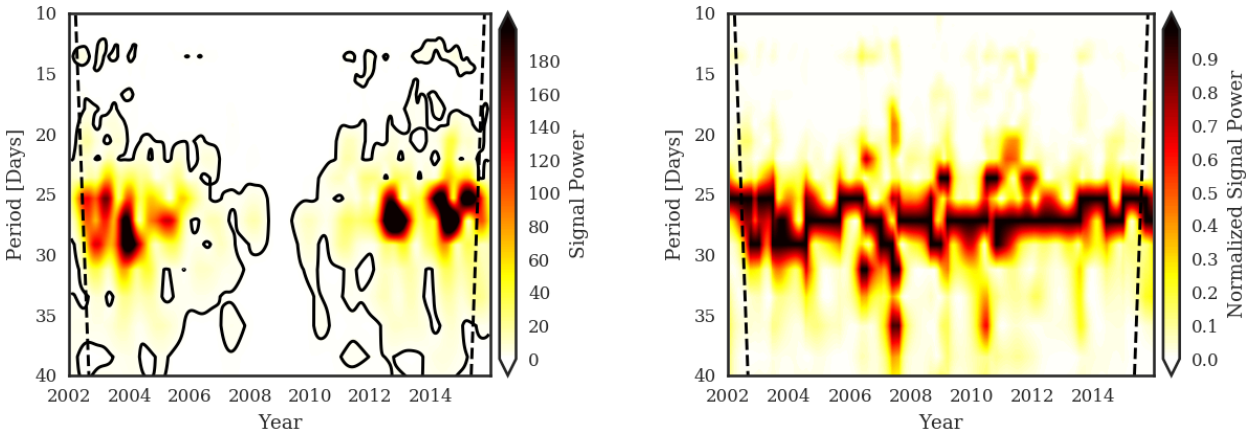

Figure 4.5: Left: Power spectrum from a CWT of GOMESCIA Mg II index. The solid black contour lines represent the 95% confidence level and the dashed black lines denote the cone of influence. Right: Power spectrum from a CWT of GOMESCIA Mg II index with each time step normalized to have a signal power between zero and one.

A CWT was applied to the OSIRIS ozone anomaly at each altitude from 19.5 to 60.5 km. The resulting power spectra for 30.5, 45.5, and 55.5 km are compared to the equivalent plots from Dikty et al. (2010) in figure 4.6. The strongest signal with a period from 25 to 32 days is observed at the end of 2003 and in 2004 at all altitudes above 30.5 km. This corresponds to a time of maximum power in the Mg II wavelet. There are also weaker, but statistically significant, signals with the appropriate periods from 2006 to 2009 when the signal in the solar proxy is relatively weak. As with the FFT, the signal power does not peak at a single period, but is high for the whole range of periods from 25 to 32 days.

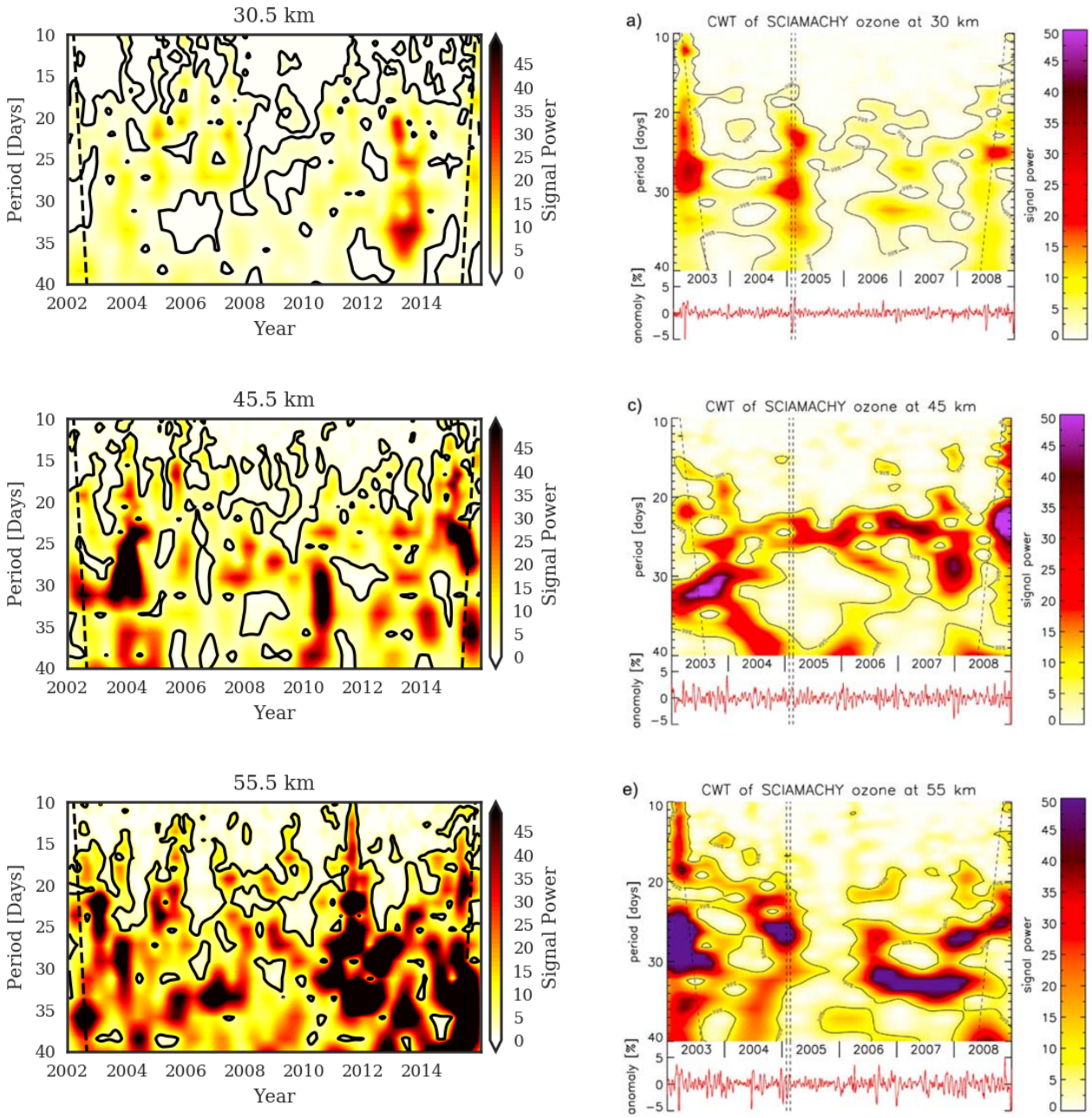

Figure 4.6: Left column: CWT power spectrum of OSIRIS daily ozone anomaly at 30.5, 45.5, and 55.5 km from 2002 to 2015. The solid black contour lines represent the 95% confidence level and the dashed black lines denote the cone of influence. Right column: CWT power spectrum of SCIAMACHY ozone anomaly at 30 km, 45 km, and 55 km from 2003 to 2008. Figures in right column from Dikty et al. (2010).

Dikty et al. (2010) found peaks in the SCIAMACHY ozone CWT at 25 days for altitudes between 42 and 47 km, but no clear peaks at lower altitudes. Above 47 km there were stronger signals with peaks covering periods from 23 to 32 days in 2004, 2006, and 2007. This peak in 2004 is very clear in the OSIRIS ozone CWT power spectrum at altitudes above 35 km. Figure 4.6 shows that all of the signals in the CWT from Dikty et al. (2010) at 45 km and 55 km appear in the OSIRIS ozone CWT as well.

After 2009 the observed signals in the OSIRIS ozone CWT are less clearly in the range of 25 to 32 days. The CWT shows that OSIRIS ozone observations only oscillate with a period that could be attributed to solar rotation during certain years. At other times the signal either dissipates or becomes unclear. At most altitudes the strongest signals with periods from 25 to 32 days occur at times when the CWT of the Mg II index also shows a strong signal, corresponding to the solar cycle maximum (2003-2005 and 2012-2015).

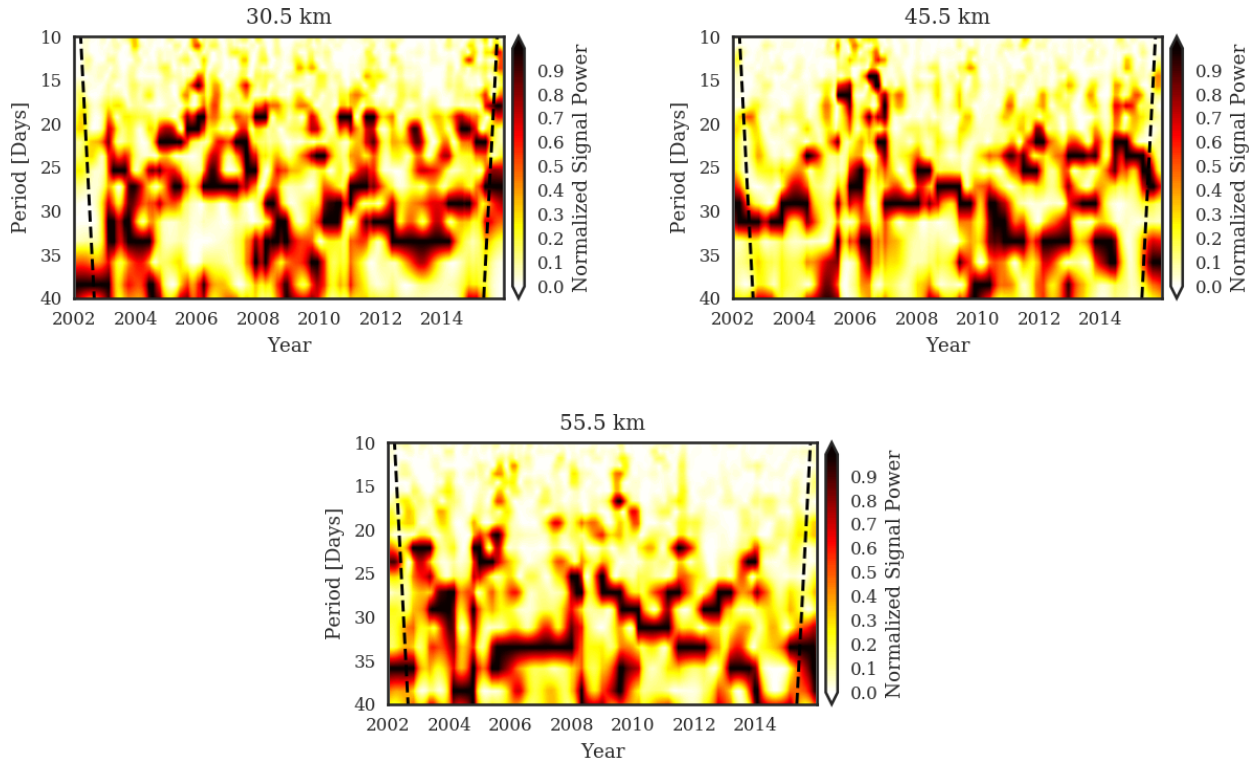

Figure 4.7: CWT power spectrum of OSIRIS daily ozone anomaly at 30.5, 45.5, and 55.5 km from 2002 to 2015 normalized between zero and one at each point in time. The dashed black lines denote the cone of influence.

Figure 4.7 shows the same OSIRIS ozone CWT power spectra at 30.5, 45.5, and 55.5 km with the signal power at each point in time (each vertical slice) normalized between zero and one. In these images there are visible signals during all years, but many of the signals occur at periods less than 25 days and greater than 32 days. The signals with periods that could be attributed to solar rotation are the same as those in the un-normalized CWT (figure 4.6): during 2003-2004 and 2006-2009 at 45.5 km. There is also a possible solar rotation signal at 55.5 km from 2010-2013.

The CWT of ECMWF temperature anomalies is shown in figure 4.8. The left column contains the results at 30.5, 45.5, and 55.5 km from 2002 to 2015. As with the ozone wavelet transform, the presence of any signals with the appropriate periods changes over time. At 30.5 km there is a signal with a period of 29 days in 2008. At 35.5 km there are signals with periods of 28 days in 2004 and 2008. All altitudes show a signal covering periods from 30 to 40 days in 2015. This signal is also present in the OSIRIS ozone CWT (figure 4.6). At 40.5 km there is a signal from 30 to 35 days in 2007 and 2010. At 45.5 and 50.5 km there are signals in 2006 and 2010. At 55.5 km the strongest signals with periods near 27 days are in 2003 and 2006.

The ECMWF temperature CWT results from Dikty et al. (2010) for three altitudes from 2003 to 2008 are in the right column of figure 4.8. Dikty et al. (2010) found a 30 day signal at 30 km in 2008 and a 35 day signal at 30 km in 2004. At 45 km Dikty et al. (2010) found a signal with a period of 23 to 35 days from 2004 to 2006 which was also apparent in the SCIAMACHY ozone CWT (figure 4.6). There was no clear signal in their temperature CWT at 55 km, but rather signals with periods varying from 20 to 35 days from 2004 to 2007. These same signals are all observed in the wavelet transforms of ECMWF temperature performed as part of the present analysis, and shown in the left column figure 4.8. These results are expected to be the same as Dikty et al. (2010) since the ECMWF data are the same. Post-2008 the temperature CWT results show only weak signals at 35.5 and 55.5 km (left column of figure 4.8). At 45.5 km the Dikty et al. (2010) results show many regions of high signal power, but these regions do not have clear periods (second panel in right column of figure 4.8).

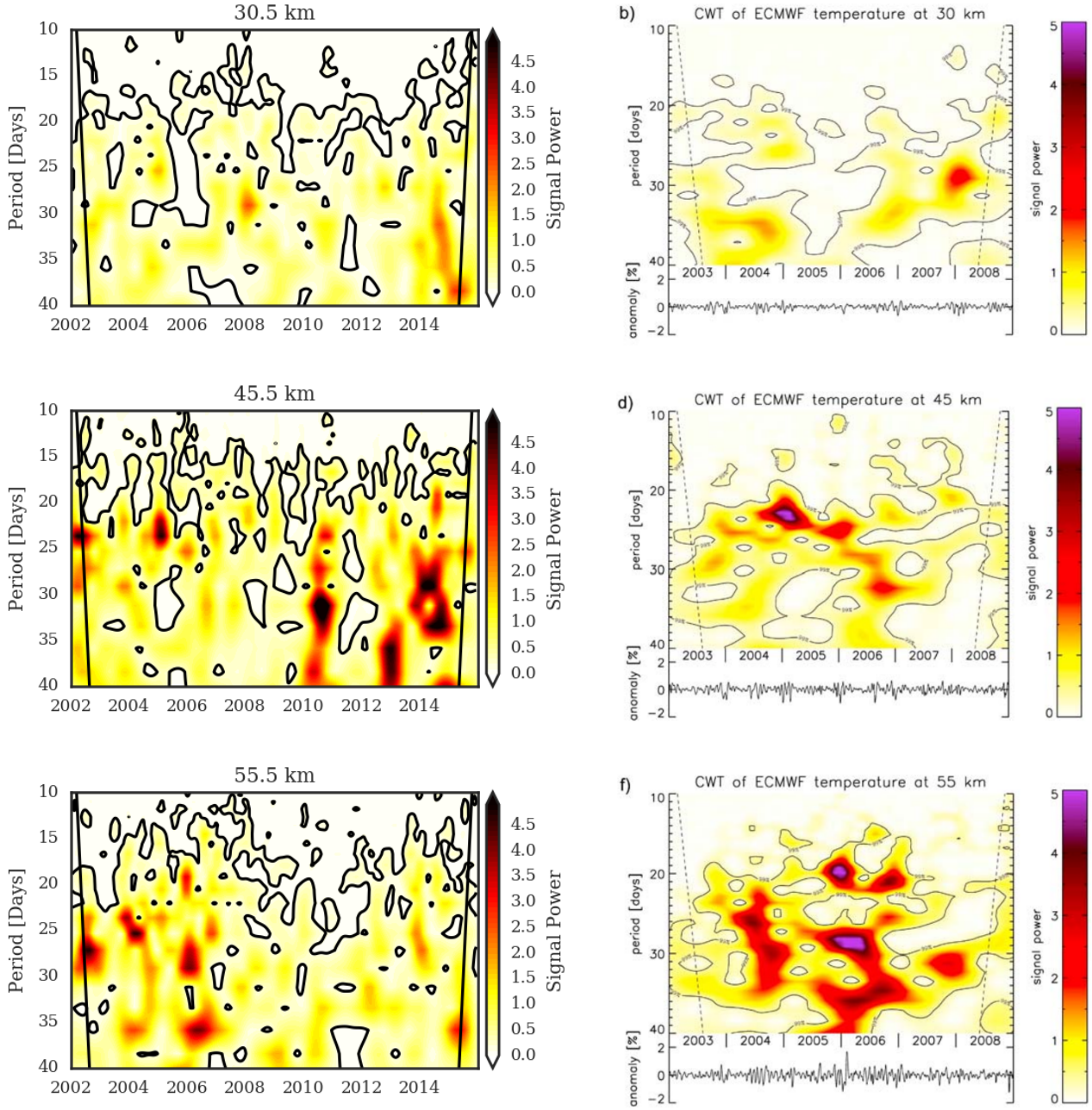

Figure 4.8: Left column: CWT power spectrum of ECMWF daily temperature anomaly at 30.5, 45.5, and 55.5 km from 2002 to 2015. The solid black contour lines represent the 95% confidence level and the dashed black lines denote the cone of influence. Right column: CWT power spectrum of ECMWF temperature anomaly at 30 km, 45 km, and 55 km from 2003 to 2008. Figures in right column from Dikty et al. (2010).

4.3 Correlation

A cross correlation quantifies the degree of similarity between two signals at each point in time as one signal is shifted relative to the other. A cross correlation between the Mg II index and OSIRIS ozone anomalies from 2002 to 2015 showed that the maximum correlation between the two parameters occurred at a lag of zero days (no shifting required) for all altitudes above 30 km.

Figure 4.9 shows the correlation coefficient at zero lag between Mg II and OSIRIS ozone concentration as a function of altitude for the three time periods of interest. The shaded regions denote the 95% confidence levels. The correlations are statistically significant above 30 km in the case of the 2002 to 2015 (orange) and 2003 to 2008 (blue) periods, and significant from 30 km to 45 km and above 52 km in the case of the 2009 to 2015 period (green). In this case "statistical significance" means the correlation coefficients have p-values less than 0.05 so there is a less than 5% chance that the signals are not correlated at these altitudes. From figure 4.9 it is clear that the degree of correlation between the Mg II solar proxy and the OSIRIS ozone concentration depends on the time period examined. From 2002 to 2015 the maximum correlation coefficient is 0.16 at 36.5 km, from 2003 to 2008 the maximum correlation coefficient is 0.33 at 50.5 km, and from 2009 to 2015 the maximum correlation coefficient is 0.15 at 37.5 km. The 2003 to 2008 time range also has a second peak correlation of 0.22 at 34.5 km.

Dikty et al. (2010) found a maximum correlation of 0.25 between SCIAMACHY ozone and the Mg II index at 35 km from 2003 to 2008. They observed that the maximum correlation value changed over time by comparing the correlation coefficients for various three month periods. During the sub-period of 2003 and 2004 they found a maximum correlation of 0.38, while during 2006 and 2007 they found an insignificant correlation at most altitudes.

Other studies have examined the level of correlation between stratospheric ozone and a solar proxy. Hood (1986) found a maximum correlation coefficient of 0.6 at 40 km with SBUV ozone from 1978 to 1980 (solar cycle 21), while Zhou et al. (2000) found a correlation of 0.37 near 36 km with SBUV/2 ozone and Hood and Zhou (1998) found a correlation of 0.35 at 35 km with UARS/MLS ozone, both for the years 1991 to 1994 (solar cycle 22). Bossay et al.

(2015) found the maximum correlation between MLS ozone and solar flux to be 0.29 from 1991 to 1994, and 0.16 near 34 km from 2004 to 2007. These results, in combination with those from Dikty et al. (2010) and those from OSIRIS presented here suggest the level of correlation between ozone and solar flux is decreasing over time.

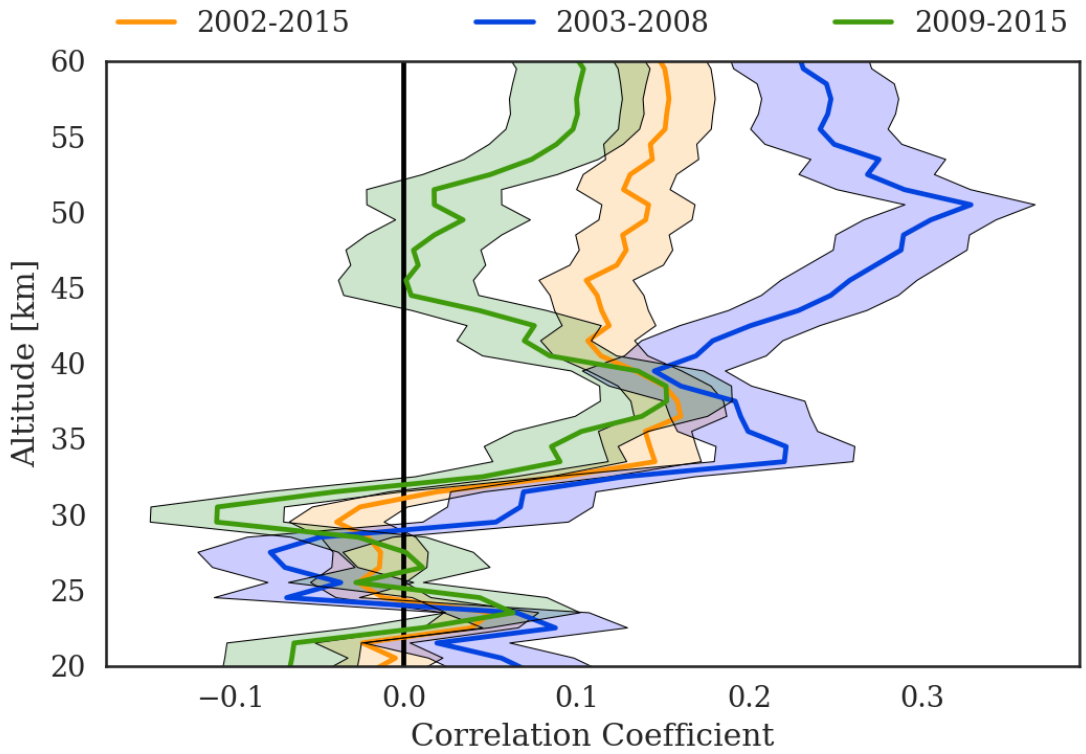

Figure 4.9: Correlation coefficient at zero lag between daily tropical OSIRIS ozone anomaly and GOMESCIA Mg II index anomaly at altitudes from 20 to 60 km for three time periods: 2002-2015 (orange), 2003-2008 (blue), and 2009-2015 (green). The shaded areas denote the 95% confidence levels.

The correlation coefficient at zero lag between the GOMESCIA Mg II index and ECMWF temperature anomaly as a function of altitude is presented in figure 4.10. In general, the degree of correlation increases with altitude. Temperature and Mg II are anti-correlated below 40 km during the 2009-2015 period. The magnitudes of the correlation coefficients are comparable to those between Mg II and OSIRIS ozone above 30 km. Dikty et al. (2010) correlated ECMWF temperature with SCIAMACHY ozone from 2003-2008 and found similar correlation coefficients to those from the present analysis. In addition, they observed higher correlation values during years closer to solar maximum (2003 and 2004) than during years

closer to solar minimum (2006 and 2007). They also found an anti-correlation between temperature and Mg II below 30 km.

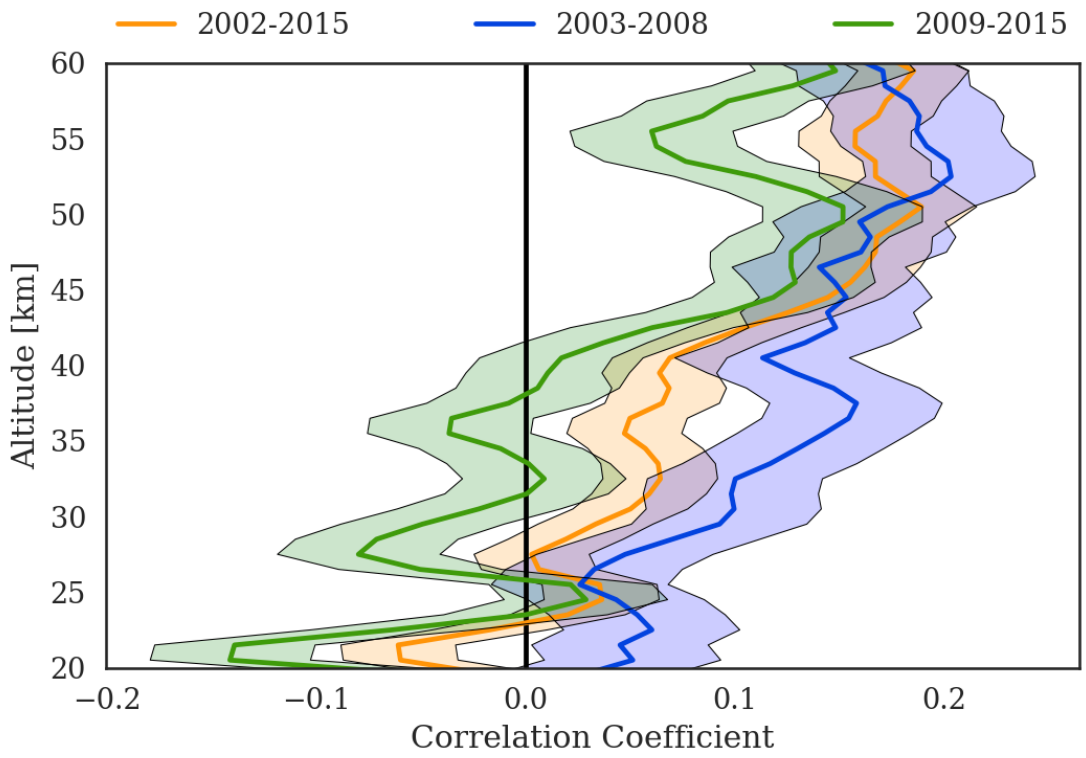

Figure 4.10: Correlation coefficient at zero lag between daily tropical ECMWF temperature anomaly and GOMESCIA Mg II index anomaly at altitudes from 20 to 60 km for three time periods: 2002-2015 (orange), 2003-2008 (blue), and 2009-2015 (green). The shaded areas denote the 95% confidence levels.

4.4 Sensitivity

Sensitivity is defined as the percent change in ozone corresponding to a 1% change in solar flux. For comparison with other studies the Mg II index was scaled to the solar flux at 205 nm for this portion of the analysis using the fact that a 1% change in the GOMESCIA Mg II index corresponds to a 0.61% change in the 205 nm flux (Dikty et al., 2010). The sensitivity is equivalent to the slope of a linear regression model in which solar flux is the independent variable and ozone is the dependent variable.

The top panel of figure 4.11 shows the sensitivity of ozone to a 1% change in the solar flux at 205 nm for each of the three time periods of interest. The response of ozone to solar

flux is generally positive above 30 km, which is the region where ozone is photochemically controlled. For all time periods the sensitivity reaches a maximum near 35 km, and then again above 50 km. The maximum ozone sensitivity near 35 km for OSIRIS ozone is 0.09%/% from 2002 to 2015. During the period of 2003 to 2008 the OSIRIS ozone sensitivity increases to 0.12%/% at 35 km and 0.22%/% at 50 km. During the 2009 to 2015 period the sensitivity decreases to insignificant values between 45 km and 50 km, however the peak near 35 km has a sensitivity of 0.1%/%.

Dikty et al. (2010) determined the sensitivity of SCIAMACHY ozone to changes in the 205 nm solar flux for their complete data set (2003-2008), as well as for two shorter periods near solar maximum (2003-2004) and solar minimum (2006-2007). Their results are shown in the bottom panel figure 4.11. For the 2003-2008 dataset the sensitivity peaks at 35 km and again at 55 km, with values of 0.19%/%. Near solar maximum the peak value was 0.20%/%, and near solar minimum the peak value at 35 km dropped to 0.13%/%, while the peak value at 54 km remained at 0.19%/%.

The results from OSIRIS and SCIAMACHY are quite similar. Both sets of ozone measurements show peaks in the sensitivity at about 35 km, with values that change very little when ozone from a different set of years is used in the analysis. The peak value at 35 km for OSIRIS ozone from 2003 to 2008 is 0.07%/% smaller than the peak value for SCIAMACHY ozone, however the OSIRIS ozone has its largest response to changes in solar flux at 50 km. This value of 0.22%/% is larger then the SCIAMACHY ozone sensitivity at that altitude.

Along with correlation, sensitivity is the most common way the effect of solar variability on stratospheric ozone has been quantified in previous studies. Bossay et al. (2015) examined ozone from UARS/MLS during solar cycle 22 (1991-1994) and ozone from Aura/MLS during solar cycle 23 (2004-2007). They found a maximum sensitivity of 0.4%/% at 35 km during solar cycle 22, and a maximum sensitivity of 0.2%/% at 35 km during solar cycle 23. They also see a peak near 50 km during the 2004-2007 period. Fioletov (2009) used SBUV and SBUV/2 ozone from 1979 to 2005 and found a maximum sensitivity of 0.4%/% near 40 km.

The top panel of figure 4.12 shows that the response of temperature to changes in solar flux is an order of magnitude smaller than the response of ozone to solar flux (the maximum value is around 0.03%/%), while the bottom panel of figure 4.12 shows that response of

ozone to changes in temperature is high: −2%/% at 40 km. This led Zhou et al. (2000) to consider a multiple linear regression model in which ozone depended upon both solar flux and temperature. Zhou et al. (2000) used SBUV ozone measurements and NCEP temperature observations from solar cycles 21 and 22. They found a single peak in the ozone sensitivity near 43 km with a maximum value of 0.46%/% during solar cycle 22. The inclusion of temperature in the regression only affected the response of ozone to solar flux from about 35 km to 45 km. Zhou et al. (2000) also found that ozone sensitivity to temperature was greater during solar cycle 22 than during solar cycle 21. Including a temperature term in the OSIRIS ozone regression increases the sensitivity of ozone to solar flux for all three time periods from 35 km to 50 km by approximately 0.04%/%.

When Zhou et al. (2000) compared their regression models to the measured ozone data they found that the temperature model provided a better fit. The correlation between the data and the model increased from 0.51 to 0.87 with the inclusion of a temperature factor. Figure 4.13 compares the regression models to the OSIRIS ozone anomaly for the 2003 to 2008 period at 35.5 km. The temperature and solar model (light blue line) provides a much better fit to the amplitude of the ozone variations than the solar only model (dark blue line). The correlation between the model and the data at 35.5 km is 0.20 without temperature and 0.53 with temperature. These correlations are lower than what Zhou et al. (2000) found, however in both cases the inclusion of temperature in the model increases the correlation with ozone observations by 0.3.

Fioletov (2009) used the sensitivity of ozone to the Mg II index over the 27-day solar rotation period to estimate how stratospheric ozone would vary over the course of an 11-year solar cycle. The approximate increase in the Mg II index from solar minimum to solar maximum was found to be 0.015 units, corresponding to a change of about 10%. The sensitivity describes how ozone responds to a 1% change in solar flux so it can be easily scaled to show the percent change in ozone corresponding to a 10% change in solar flux. Fioletov (2009) used this scaling and found a peak of 2% change in ozone from solar minimum to solar maximum at 40 km in SBUV ozone from 1979 to 2005. This is shown by the orange circles in the top panel of figure 4.14.

The OSIRIS ozone measurements span just over one solar cycle. During this time the Mg

II index has its maximum values at the beginning of 2002 and in mid 2014. The minimum value occurs near the end of 2008. The difference from the average solar minimum value to the average solar maximum value of the Mg II index is 0.015 units. This is the same maximum to minimum difference found by Fioletov (2009). A value of 0.015 units corresponds to a 9.7% variation in the Mg II index from 2002 to 2015.

Earlier in this analysis the OSIRIS ozone sensitivity was calculated after the ozone anomaly time series was filtered by the subtraction of a 35-day running mean. This filter would have removed any solar cycle signal that was present and therefore can not be used when determining the percent change in ozone from solar minimum to solar maximum. The maximum OSIRIS ozone response to a 1% change in the 205 nm flux without the 35-day filter is 0.36 at 35 km. This corresponds to a change of 3.5% from solar minimum to solar maximum.

The bottom panel of figure 4.14 shows the percent change in OSIRIS ozone from solar minimum to solar maximum for altitudes from 19.5 to 60.5 km. The shape of the profile is somewhat different from the findings in Fioletov (2009), and the values span a slightly larger range. The orange circles in the top panel of figure 4.14 show that Fioletov (2009) found a single peak structure with a maximum at 40 km and minima at 50 km and 30 km. The bottom panel of figure 4.14 shows that there are indeed minima at 50 km and 30 km, but the percent change in OSIRIS ozone begins to increase again above and below those points. The values at 50 km and 30 km also become negative in figure 4.14, while in Fioletov (2009) they have values of 0.5%. Results from OSIRIS agree better with the model results given by the black lines in the top panel of figure 4.14 than with the estimate by Fioletov (2009). In particular, the dashed line showing results from Egorova et al. (2004) has a maximum value near 32 km and becomes negative near 45 km.

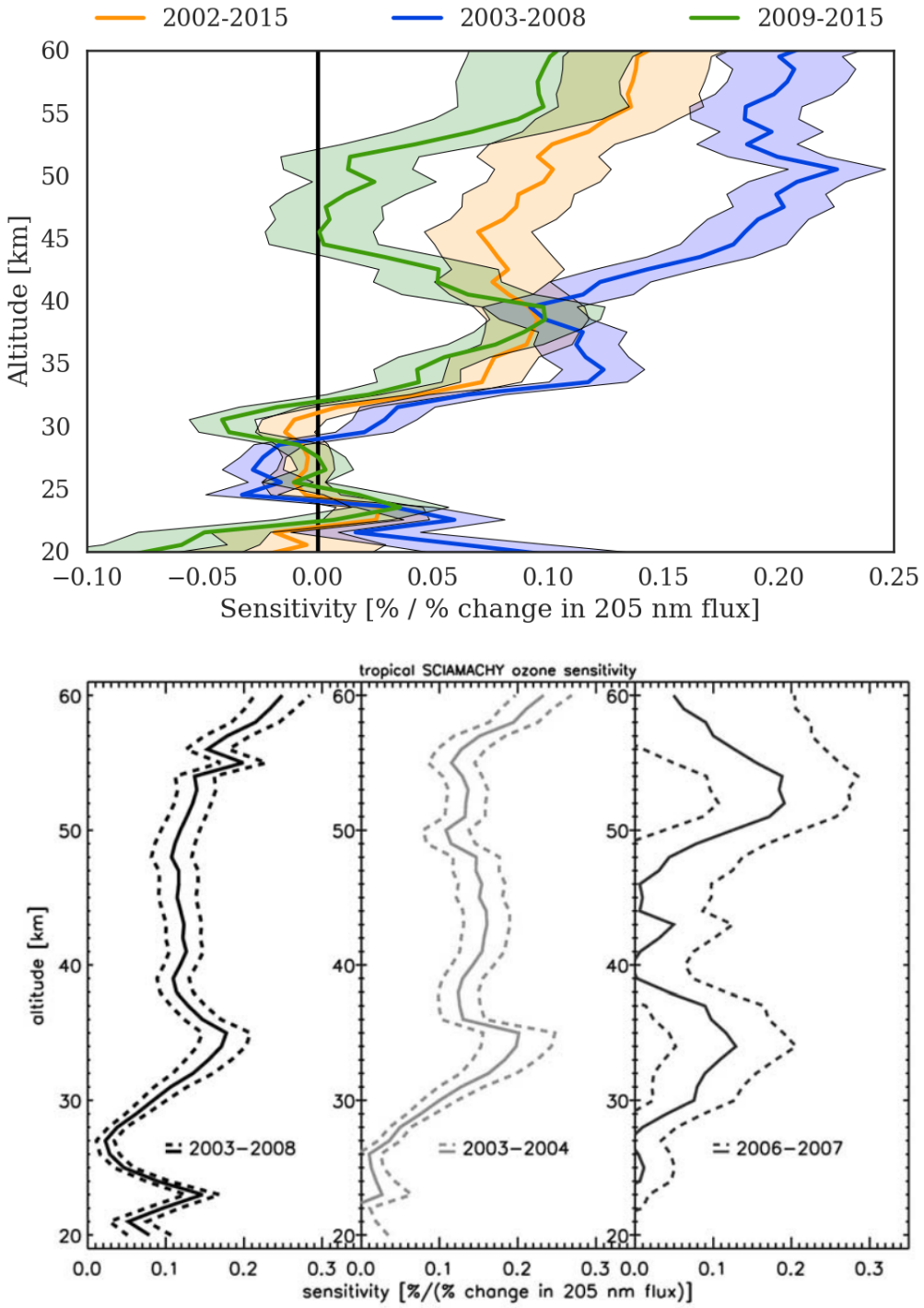

Figure 4.11: Top: Sensitivity of OSIRIS ozone to a 1% change in solar flux at 205 nm for three time periods: 2002-2015 (orange), 2003-2008 (blue), and 2009-2015 (green). The shaded regions denote the 2σ uncertainty level. Bottom: Sensitivity of SCIAMACHY ozone to a 1% change in solar flux at 205 nm for three different time periods. The dashed lines denote the 2σ uncertainty level. Bottom panel is figure 11 of Dikty et al. (2010).

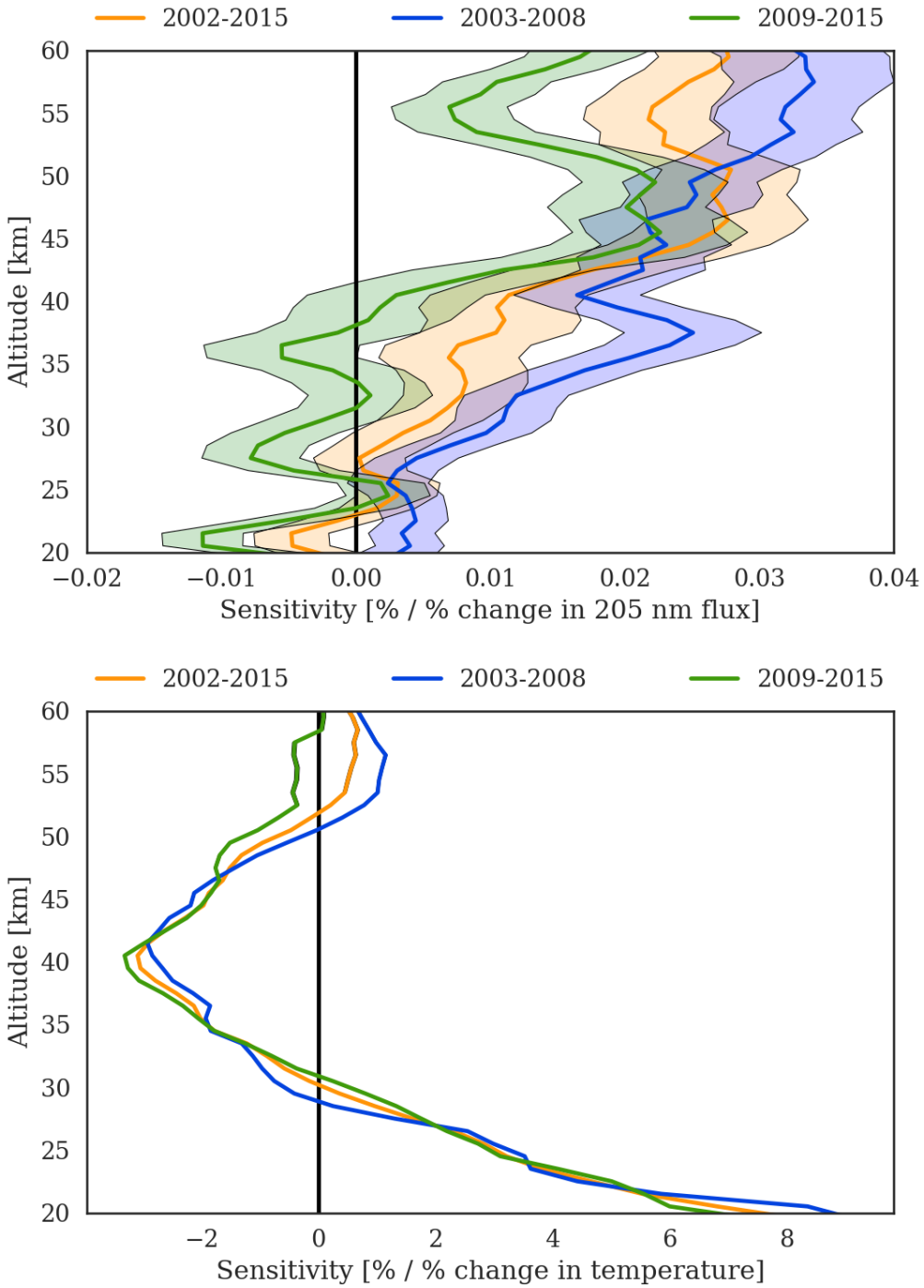

Figure 4.12: Top: Sensitivity of ECMWF temperature to a 1% change in solar flux at 205 nm for three time periods: 2002-2015 (orange), 2003-2008 (blue), and 2009-2015 (green). The shaded regions denote the 2σ uncertainty level. Bottom: Sensitivity of OSIRIS ozone to a 1% change in ECMWF temperature for the same three time periods.

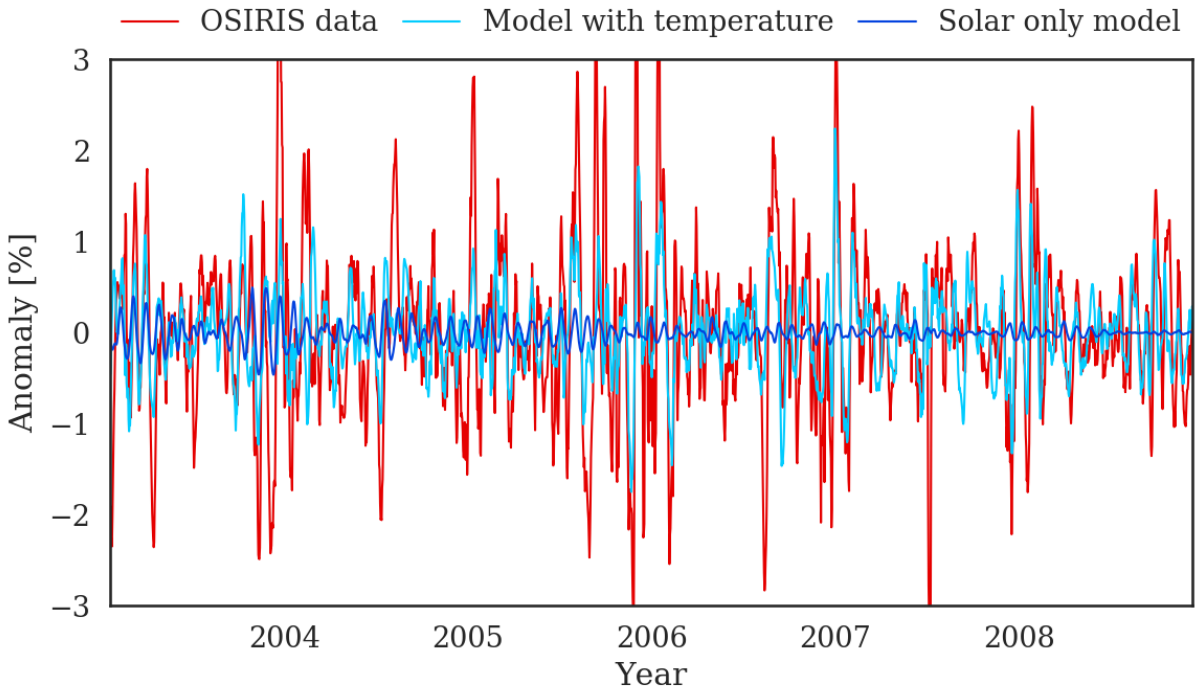

Figure 4.13: Results from a linear regression model fitting solar flux at 205 nm to OSIRIS ozone at 35.5 km from 2003 to 2008 both with (light blue) and without (dark blue) a temperature term in the model. The red line is the OSIRIS ozone anomaly at 35.5 km.

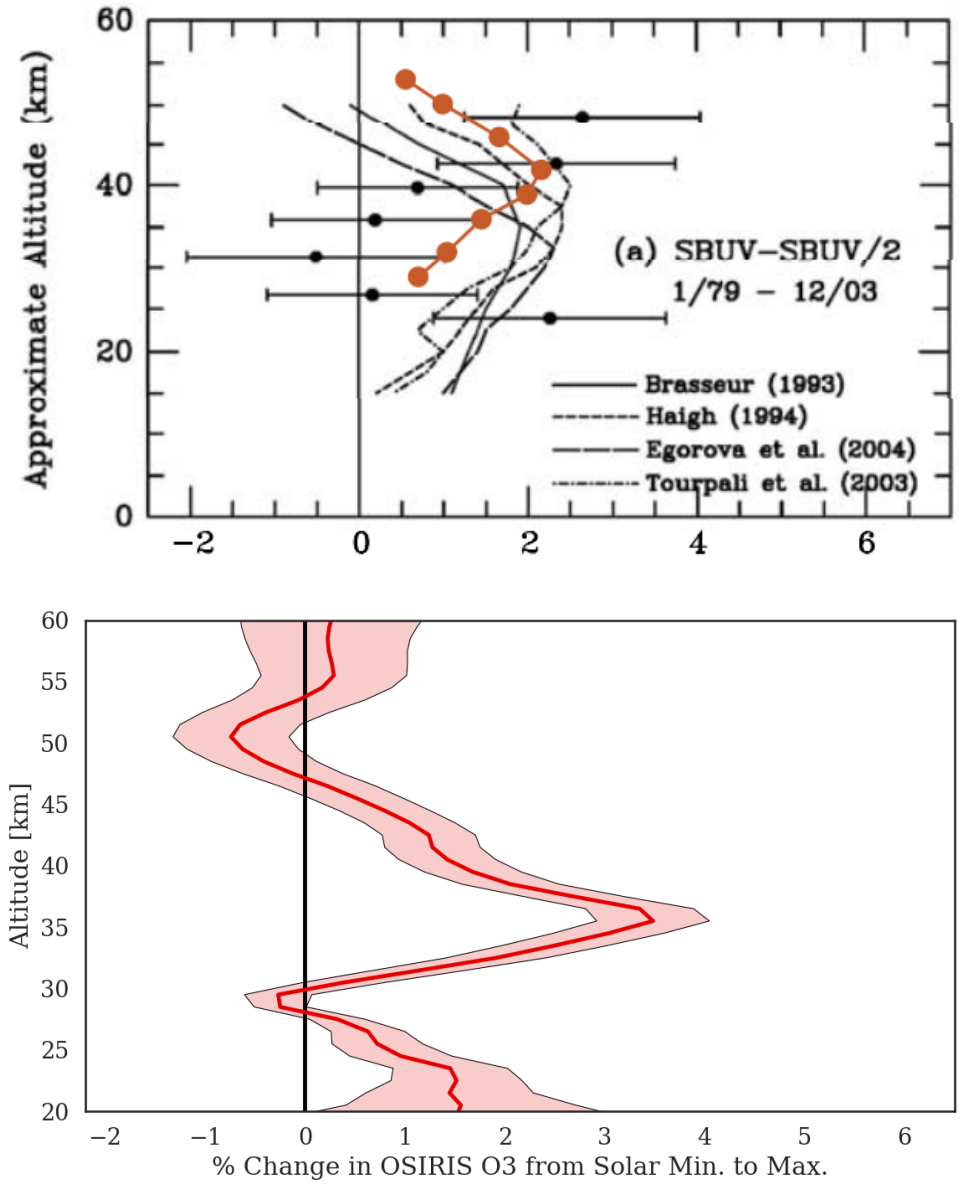

Figure 4.14: Top: The black circles are the percent change in SBUV and SBUV/2 ozone from solar minimum to solar maximum during the years 1979 to 2003. The black lines show the percent change in ozone from solar minimum to maximum as determined by four different modelling studies. The orange circles are the estimated variation in SBUV and SBUV/2 ozone from solar minimum to maximum calculated by Fioletov (2009) using the 27-day ozone sensitivity. Image is figure 9 of Fioletov (2009). Bottom: Percent change in OSIRIS ozone from solar minimum to solar maximum as a function of altitude for the years 2002 to 2015. The shaded region denotes the 2σ uncertainty level. The values are calculated by scaling the 27-day ozone sensitivity.

Chapter 5

Results: Aerosol

The direct effect of variations in solar irradiance on stratospheric aerosol has not been previously studied. Carbonyl sulfide is photodissociated by UV radiation in the stratosphere to produce sulfur, which through a series of reactions can result in H_2SO_4. The production of H_2SO_4 aerosol particles from volcanically injected SO_2 does not depend on photolysis, so it is unclear whether or not a noticeable effect of solar UV variability on aerosol can be observed. This connection was investigated with the same signal processing techniques applied to ozone in the previous chapter: FFT, CWT, correlation with Mg II, and simple linear regression.

More commonly, researchers have studied the effect of GCRs on aerosol formation. GCRs are thought to increase aerosol production through ionization of the atmosphere. GCR flux is anti-correlated with the solar cycle, which would result in a negative response of aerosol extinction (corresponding to fewer aerosol particles) to an increase in solar irradiance. A superposed epoch analysis of short decreases in the amount of GCRs reaching the atmosphere, known as Forbush decreases, was used to examine the effect of cosmic rays on aerosol extinction and particle size.

5.1 Effect of Solar UV Variability

The power spectrum resulting from a CWT applied to the OSIRIS aerosol extinction anomaly is dominated by three signals in 2005, 2007, and 2015 that have periods spanning 10 to 40 days and appear at most altitudes. These strong signals are likely due to volcanic activity. The left panel of figure 5.1 shows the CWT at 31.5 km, which has a dominant signal in 2005. The right panel of figure 5.1 shows the CWT power spectrum of OSIRIS aerosol extinction with each time step normalized to be between zero and one. This normalization allows signals

with lower powers than the 2005 signal to be visible. There is a signal from 2012 to 2014 with periods from 25 to 35 days that could be associated with solar rotation. This signal is present at altitudes from 27.5 to 31.5 km, but otherwise the normalized power spectra for altitudes from 20 to 35 km do not show any signals with appropriate periods.

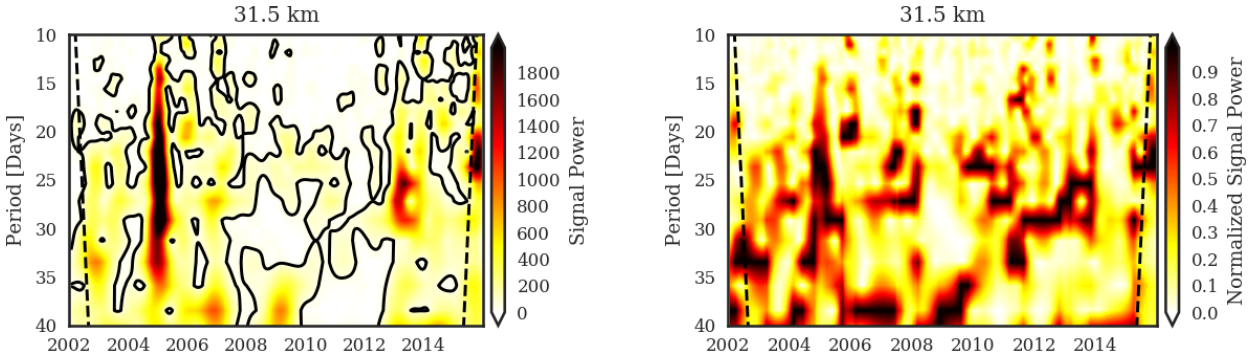

Figure 5.1: Left: Power spectrum from a CWT of OSIRIS aerosol extinction at 31.5 km. The solid black contour lines represent the 95% confidence level and the dashed black lines denote the cone of influence. Right: Power spectrum from a CWT of OSIRIS aerosol extinction at 31.5 km with each time step normalized to have a signal power between zero and one.

The FFT power spectrum of the OSIRIS aerosol extinction anomaly for three time ranges (2002-2015, 2003-2008, and 2009-2015) and three altitudes (25.5, 30.5, and 32.5 km) is shown in figure 5.2. The signal power increases greatly with altitude. The strongest signals have periods in the range of 20 to 30 days, and at 25.5 km the 2002-2015 time series shows a peak at a period of 27 days. When considering the FFT of OSIRIS ozone in the previous chapter it was observed that solar variability only had an effect on the ozone concentration above 35 km, in the region where ozone production is photochemically controlled. As the aerosol extinction values are only retrieved below 35 km there are likely non-chemical effects influencing the results, in addition to the aforementioned volcanic activity.

Figure 5.3 shows the results of a cross correlation between the OSIRIS aerosol extinction anomaly and the GOMESCIA Mg II anomaly. The level of correlation between OSIRIS aerosol extinction and Mg II at zero lag is insignificant from 22 to 32 km (coefficients between -0.05 and -0.02 for each of the three time ranges). Unlike the correlation of OSIRIS ozone and Mg II, the maximum level of correlation between aerosol extinction and Mg II does not occur

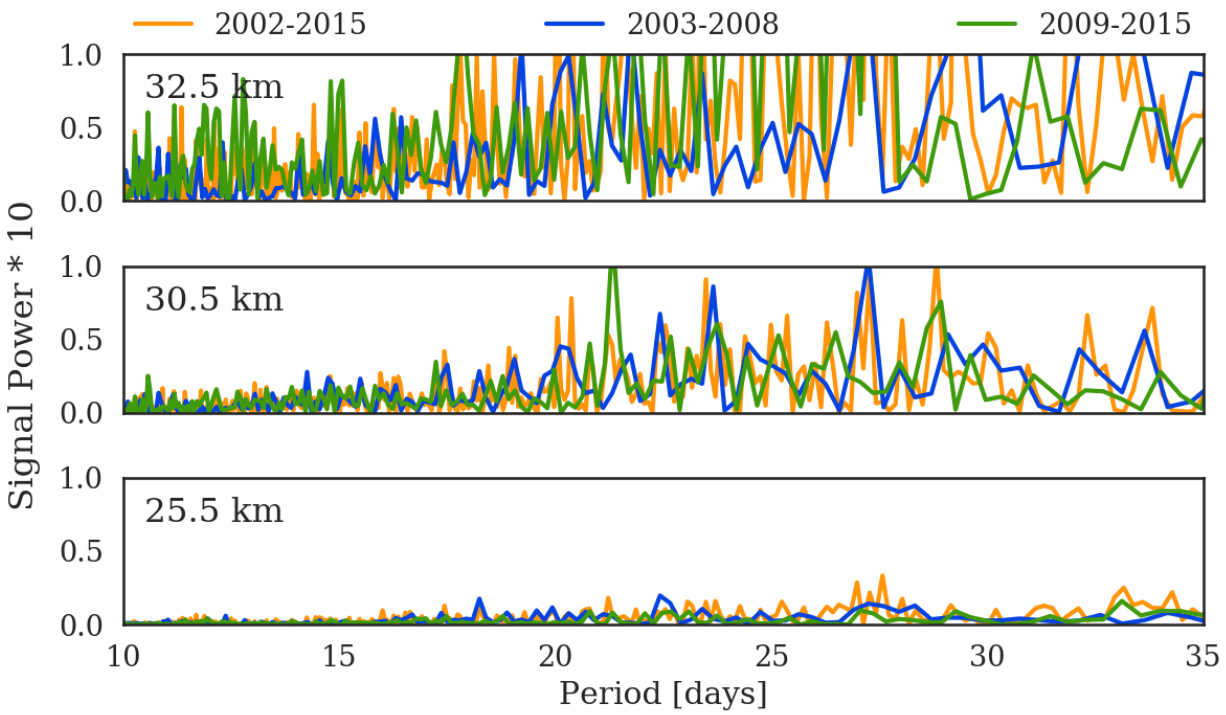

Figure 5.2: FFT power spectrum of daily zonal average OSIRIS aerosol extinction anomaly at 25.5, 30.5, and 32.5 km for three time periods: 2002-2015 (orange), 2003-2008 (blue), and 2009-2015 (green).

at a lag of zero days: the amount of lag depends on altitude and the time period examined.

Figure 5.4 shows the sensitivity of OSIRIS aerosol extinction to a 1% change in solar flux at 205 nm for three time ranges. From 23 to 31 km each time period shows a negative sensitivity, decreasing from about -0.04 %/% to -0.15 %/% as altitude increases. Above and below these altitudes there are large differences in sensitivity between the three time periods. The lowest altitudes are the most affected by volcanic activity, while the highest altitudes of the retrieved aerosol extinction have a larger error.

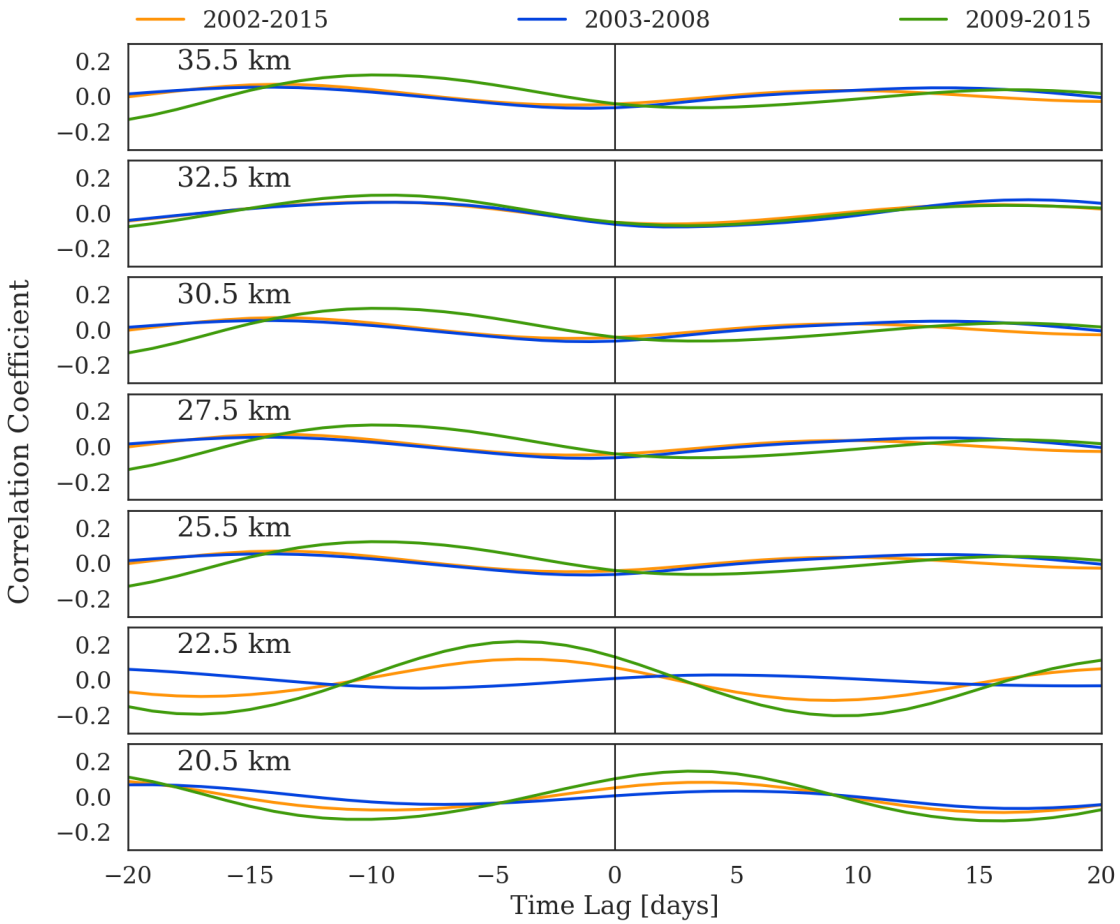

Figure 5.3: Correlation coefficient between OSIRIS aerosol extinction anomaly and GOMESCIA Mg II anomaly for lags from -20 to 20 days and seven altitudes from 20.5 to 35.5 km. The cross-correlation was done for three time periods: 2002-2015 (orange), 2003-2008 (blue), and 2009-2015 (green).

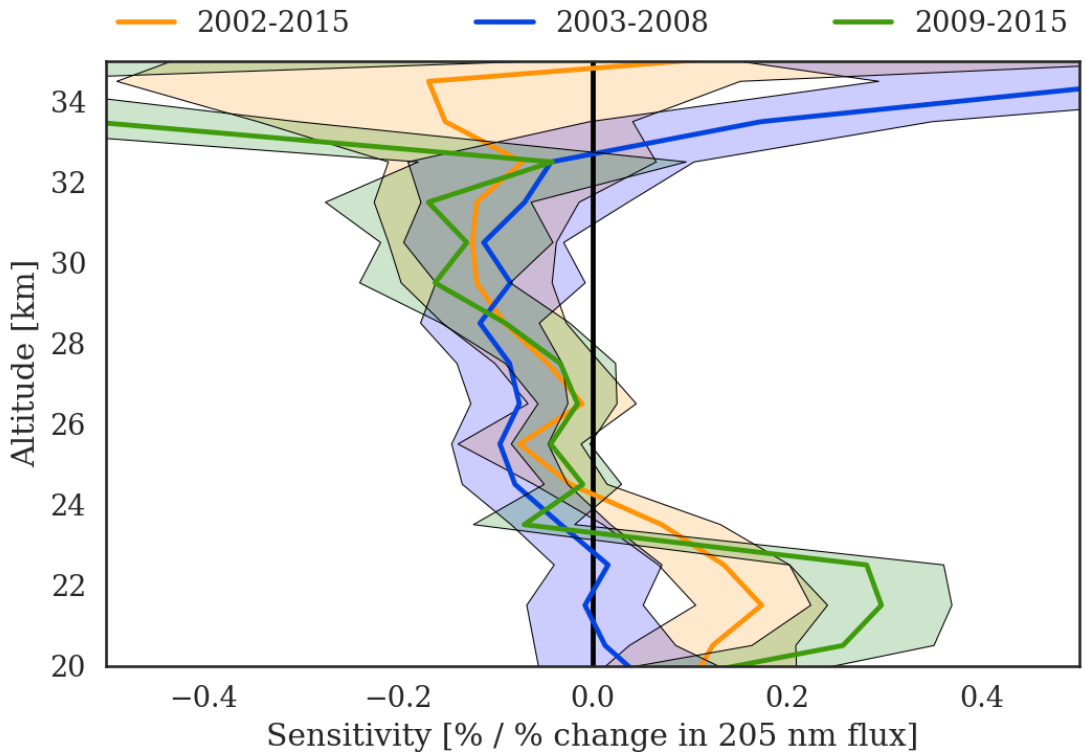

Figure 5.4: Percent change in OSIRIS aerosol extinction per 1% change in 205 nm flux for three time periods: 2002-2015 (orange), 2003-2008 (blue), and 2009-2015 (green). The shaded regions denote the 2σ uncertainty level.

5.2 Effect of GCRs

The negative response of aerosol to increases in solar flux could be due to the decrease in cosmic rays, ionization, and nucleation that occurs during periods of higher solar activity. Figure 5.5 shows the cross correlation between the OSIRIS aerosol extinction anomaly and the anomaly in the Moscow neutron monitor count for seven altitudes and three time periods. The maximum correlation coefficient occurs at a lag of about 4 days at all altitudes. The 2002 to 2015 and 2003 to 2008 time ranges show a positive correlation between GCRs and aerosol extinction, with a maximum of 0.15 at 22.5 km. The 2009 to 2015 period has an opposite variation in the correlation coefficient.

A superposed epoch analysis was applied to the FD events identified in the Moscow neutron monitor counts from 2002 to 2015. The superposed epoch as a function of time from the event onset is presented in figure 5.6. The red line is the mean, the blue lines are the

standard error, and the dashed black lines denote the 95% significance level. Any variations in the mean that fall outside the dashed black lines can be considered significant with 95% confidence. There is an average decrease of 4% at day zero of the epoch. There is a second insignificant decrease near day 25 as some of the events had smaller FDs occurring after the main FD.

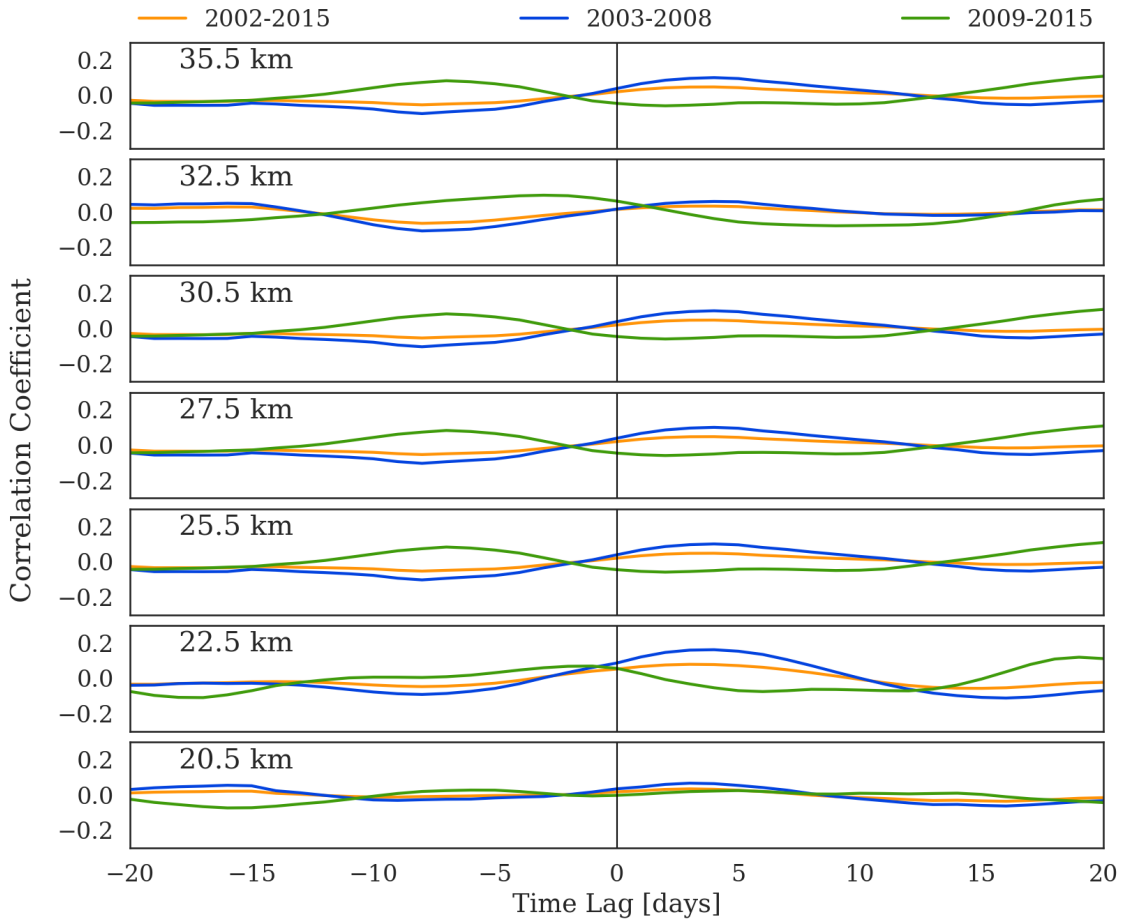

Figure 5.5: Correlation coefficient between daily tropical OSIRIS aerosol extinction anomaly and Moscow neutron monitor count anomaly for lags from -20 to 20 days and seven altitudes from 20.5 to 35.5 km. The cross-correlation was done for three time periods: 2002-2015 (orange), 2003-2008 (blue), and 2009-2015 (green).

Figures 5.7 and 5.8 show the average aerosol extinction in the tropics during FDs at 30.5 km and 32.5 km. At 30.5 km there are no statistically significant variations. At 32.5 km there is a slightly significant increase in the extinction at 20 days. An increase in extinction

is not expected in relation to an FD. A decrease in nucleation should result in a decrease in optical depth, and therefore a decrease in extinction.

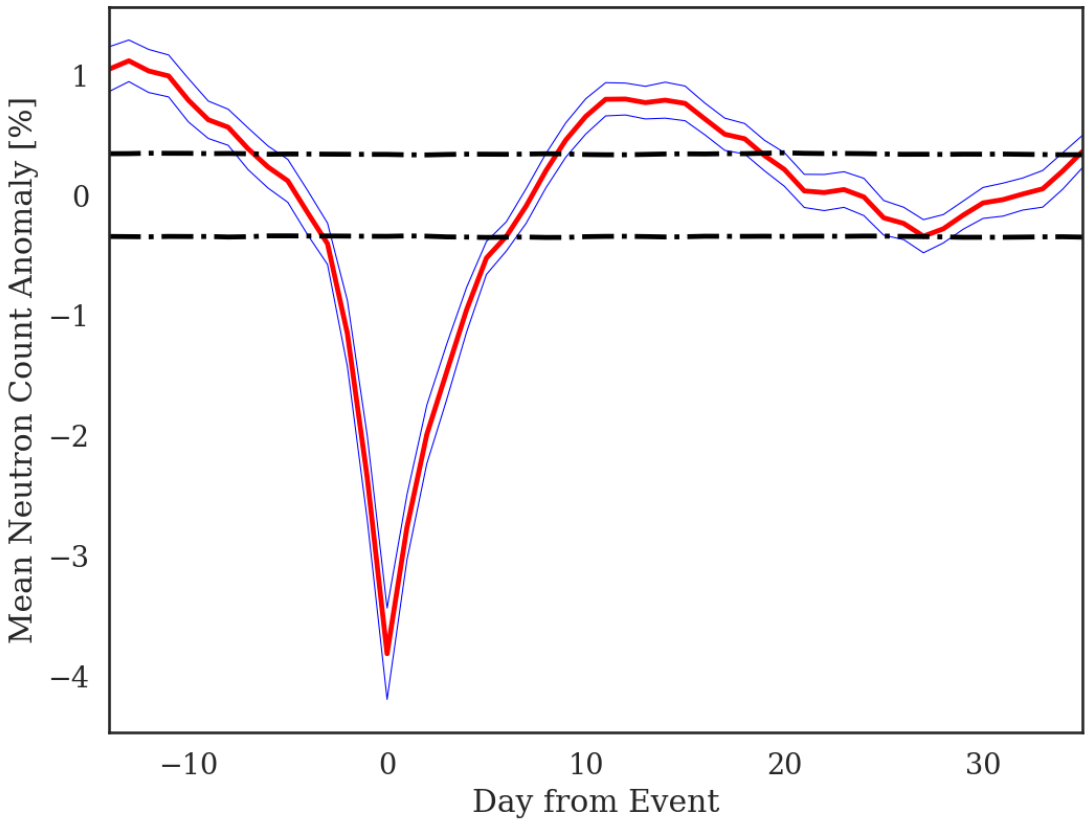

Figure 5.6: Average cosmic ray flux observed by the Moscow neutron monitor before, during, and after 45 Forbush decreases. The red line is the mean neutron count anomaly, the blue lines mark the standard error, and the dashed black lines denote the 95% confidence level.

The Ångstrom exponent has only been processed for OSIRIS measurements up until mid 2012, covering 28 of the 45 identified FD events. Figure 5.9 shows that the average Ångstrom exponent at 30.5 km decreases by almost 2% 11 days after the FD. At 34.5 km (figure 5.10) there are decreases in the Ångstrom exponent 1 day before and 1 day after the FD. A decrease in Ångstrom exponent corresponds to an increase in particle size which is the result expected for a decrease in cosmic rays. Although the signs are correct and the decreases pass the significance test it is unlikely they are real signatures of an effect: the

decrease in the Ångstrom exponent should occur the same number of days from the FD at each altitude. The higher altitudes were examined as the data there are least likely to be contaminated by volcanic eruptions, however the earlier investigation into the effect of solar irradiance on aerosol extinction does show a large variation in the aerosol sensitivity above 30 km which could be affecting the results of the epoch analysis (5.4). Lower altitudes (20 to 30 km) also do not show any consistent, significant, decrease in the Ångstrom exponent or aerosol extinction.

The significance testing is not exact for two reasons. The first reason is that the probability distributions resulting from the randomly chosen events are not exactly Gaussian, so using ± 1.96 to represent the 5% and 95% levels is not correct, however the difference is small. The other issue is that while the samples for the significance test are chosen randomly, the actual events were manually filtered to remove any epoch containing multiple large Forbush decreases. This was not done in the case of the random events and therefore the simulation is not an exact replication of the way the data were processed.

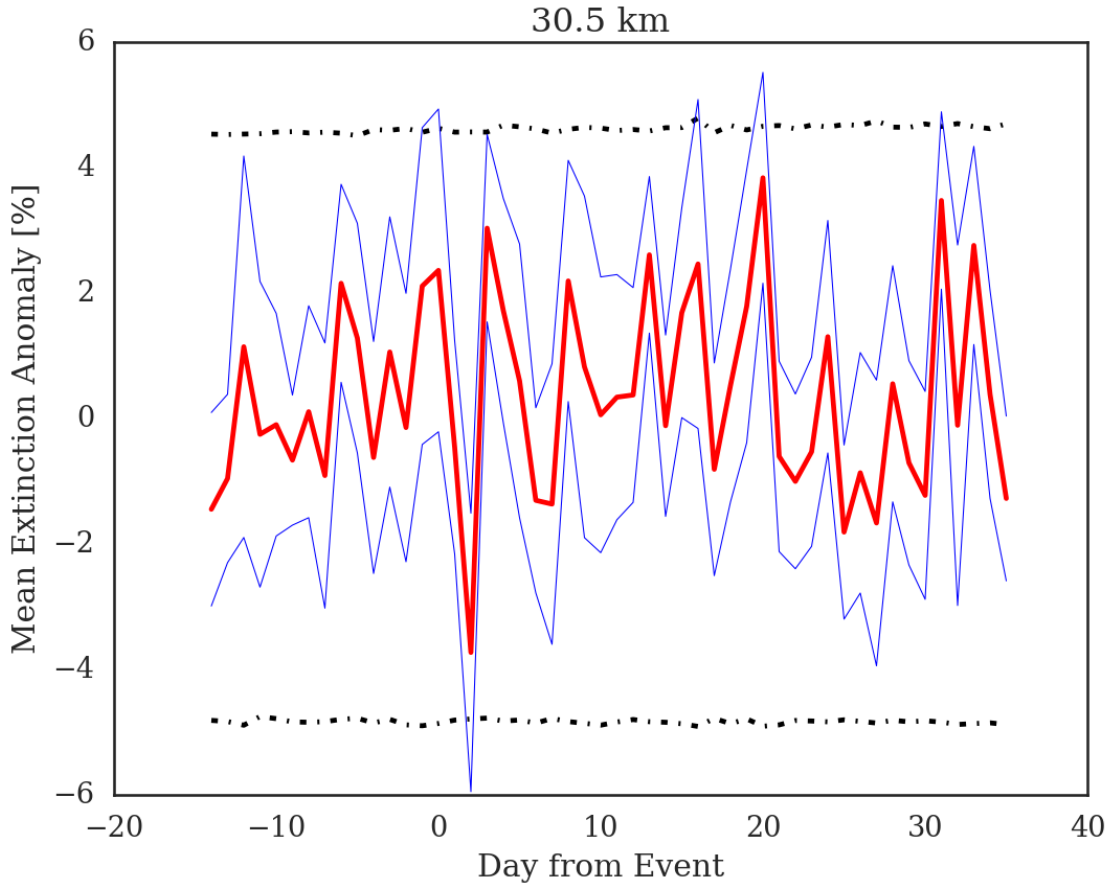

Figure 5.7: Average OSIRIS aerosol extinction anomaly in the tropics at 30.5 km before, during, and after 45 Forbush decreases. The red line is the mean aerosol extinction anomaly, the blue lines mark the standard error, and the dashed black lines denote the 95% confidence level.

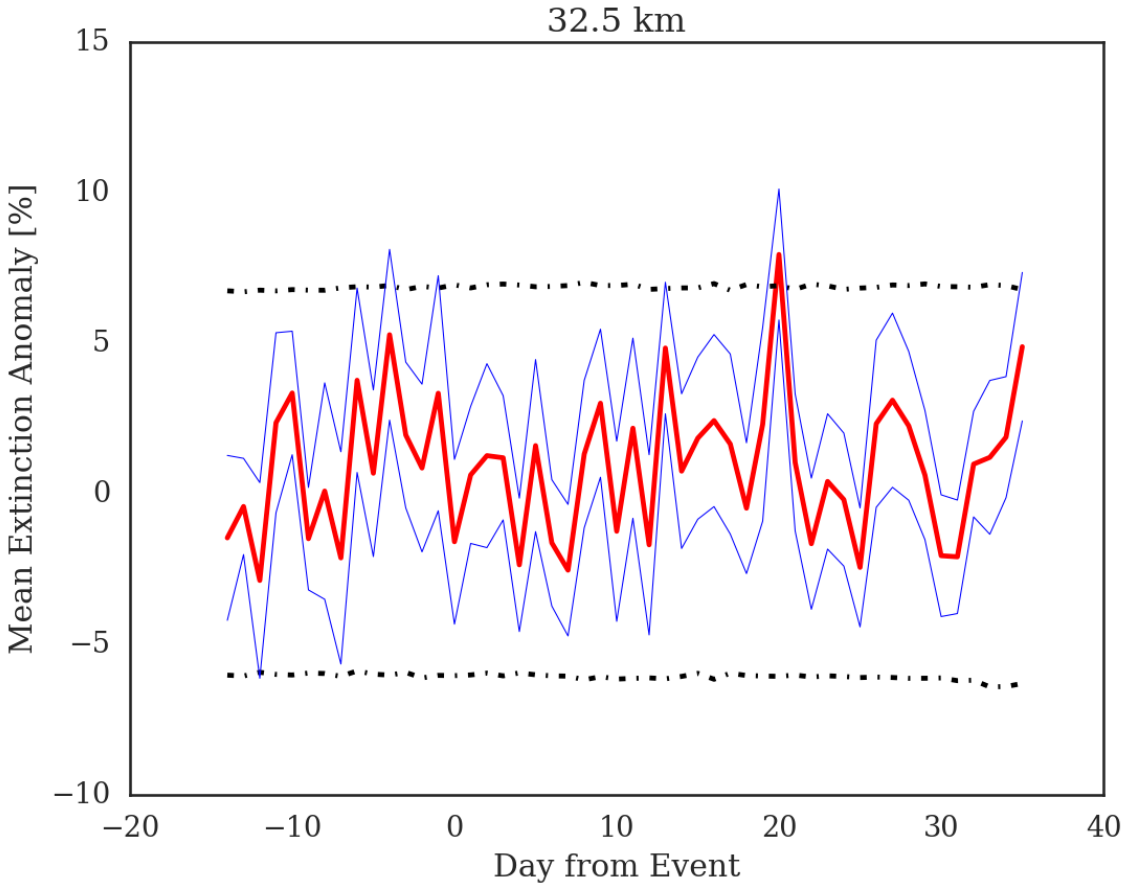

Figure 5.8: Average OSIRIS aerosol extinction anomaly in the tropics at 32.5 km before, during, and after 45 Forbush decreases. The red line is the mean aerosol extinction anomaly, the blue lines mark the standard error, and the dashed black lines denote the 95% confidence level.

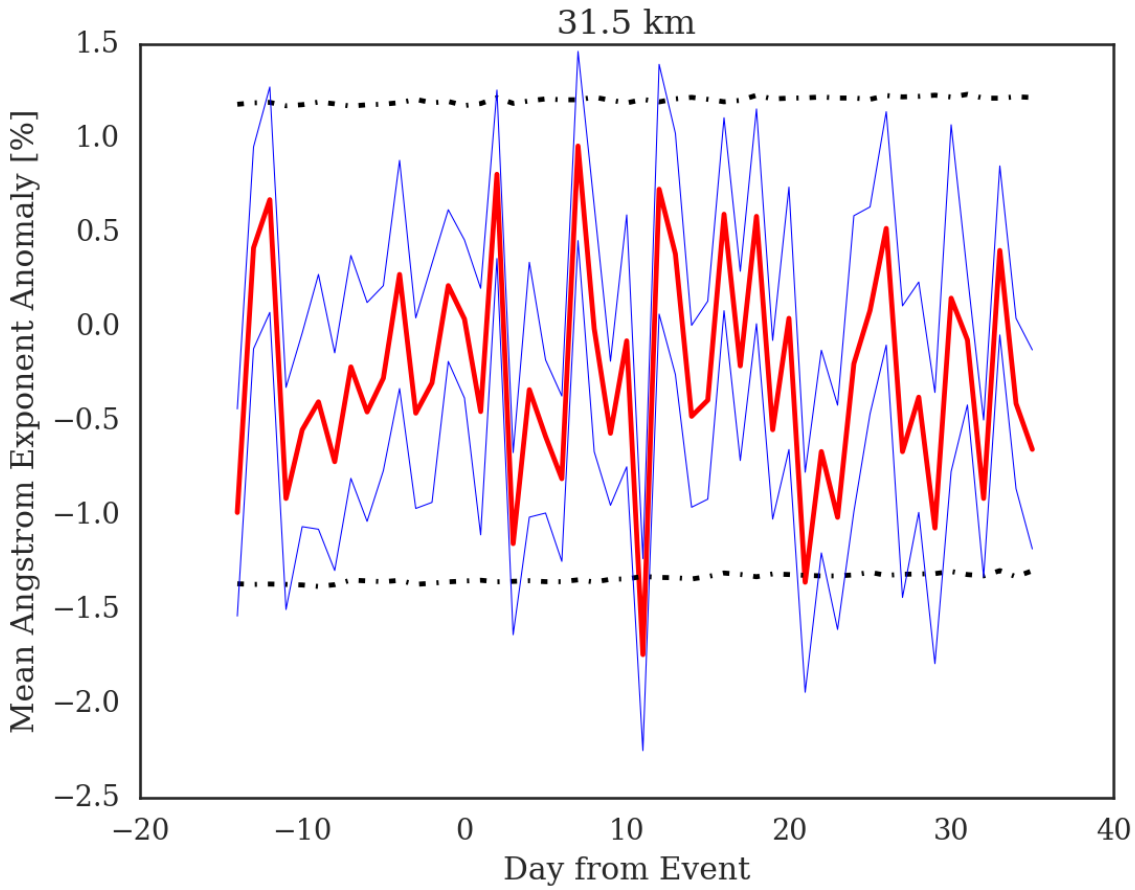

Figure 5.9: Average OSIRIS Ångstrom exponent anomaly in the tropics at 31.5 km before, during, and after 28 Forbush decreases. The red line is the mean Ångstrom exponent anomaly, the blue lines mark the standard error, and the dashed black lines denote the 95% confidence level.

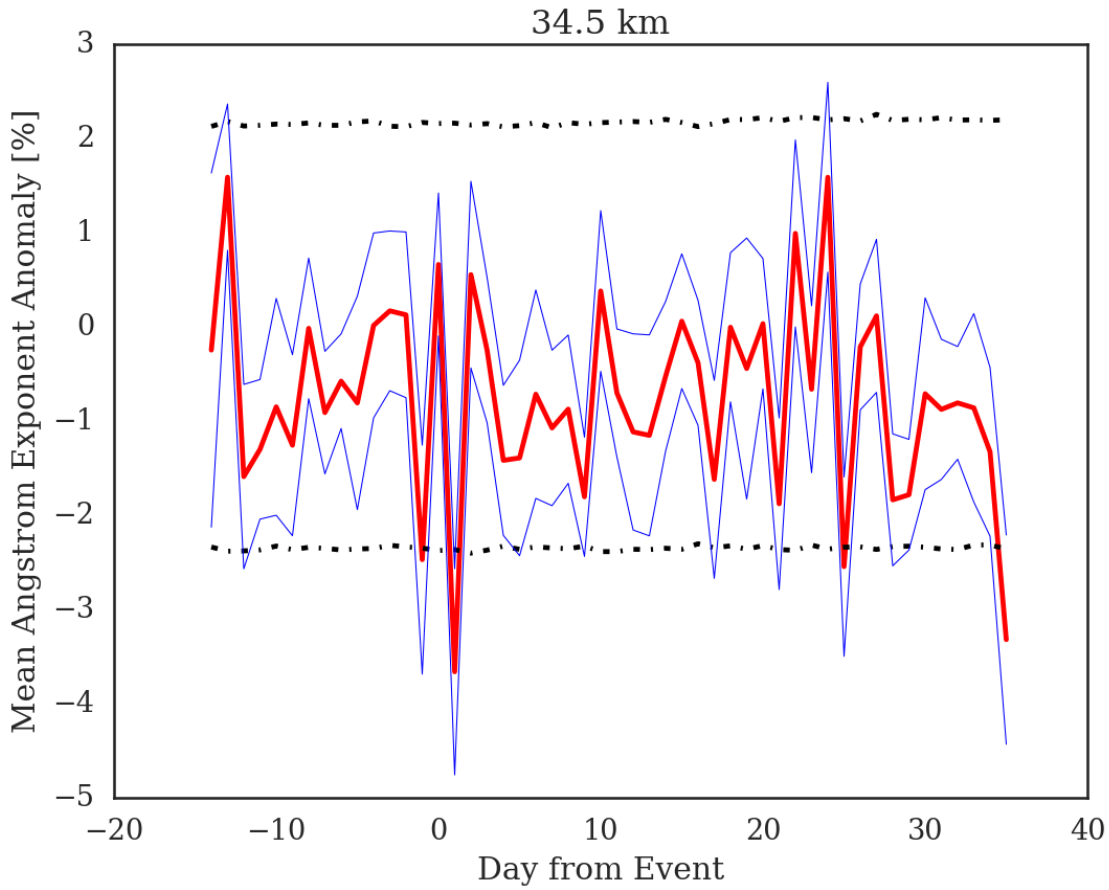

Figure 5.10: Average OSIRIS Ångstrom exponent anomaly in the tropics at 34.5 km before, during, and after 28 Forbush decreases. The red line is the mean Ångstrom exponent anomaly, the blue lines mark the standard error, and the dashed black lines denote the 95% confidence level.

Chapter 6

Conclusion

The effect of solar UV variability on OSIRIS ozone and aerosol observations was explored, and the results were compared with those from other instruments. Past studies with ozone have used only three to six years of data, with minimal overlap between instruments. Fourteen years of OSIRIS measurements provide valuable information about how ozone varies over a complete solar cycle, which can be applied to climate models. Variations in aerosol have been linked to changes in GCRs over the solar cycle: OSIRIS aerosol data products have been examined to determine if this is indeed the case. The contribution of aerosols to the global climate is not well understood, so it is useful to know if there is an observable solar cycle influence.

A CWT and FFT were used to search for periods near 27 days in OSIRIS ozone and ECMWF temperature anomalies that could be caused by variations in UV irradiance from sunspots and faculae as they are directed towards and away from the Earth by the Sun's rotation. The OSIRIS ozone FFT and CWT power spectra showed periods in the range of 25 to 32 days above 40 km, with the exact values depending on the altitude and time period examined. The strongest signal occurred at the end of 2003 and beginning of 2004, which was a particularly strong period of solar activity. The Mg II index also has high CWT and FFT signal power centred on 27 days during this time. The signal analysis of both OSIRIS ozone and ECMWF temperature agreed with results from Dikty et al. (2010) from 2003 to 2008. In the following years there are still signals observed in the OSIRIS ozone and ECMWF temperature CWT power spectra, however they cover a wider range of periods (20 to 35 days) and cannot be attributed to solar UV variations with any certainty.

The degree of correlation between OSIRIS ozone and the Mg II index depends on the time period examined. The activity level of solar cycle 23 was declining from 2003 to 2008.

During this time the maximum correlation coefficient was 0.22 at 34.5 km. During the same time Dikty et al. (2010) found a maximum correlation between SCIAMACHY ozone and the Mg II index of 0.25 at 35 km. Dikty et al. (2010) also observed a higher correlation coefficient during 2003 and 2004 than 2006 and 2007, corresponding to periods of higher and lower solar activity, respectively. From 2009 to 2015 the maximum correlation coefficient between OSIRIS ozone and Mg II was only 0.15 at 37.5 km. Earlier studies with ozone from solar cycles 21 and 22 found correlations as high as 0.6, which suggests the effect of solar irradiance on ozone number density is decreasing over time. The maximum of solar cycle 24 had the lowest number of recorded sunspots since satellite observations of ozone began (Schröder et al., 2017), while solar cycle 23 had a longer than usual minimum and multiple days without sunspots (Nandy et al., 2011). It is likely that this decrease in the number of sunspots (and associated faculae) is responsible for the decreased solar signal in ozone during solar cycles 23 and 24 compared to solar cycles 21 and 22.

The sensitivity of OSIRIS ozone to a 1% change in solar flux at 205 nm is 0.12% at 35.5 km and 0.22% at 55.5 km from 2003 to 2008. Dikty et al. (2010) found the maximum sensitivity of SCIAMACHY ozone to be 0.19% at both 35 and 50 km for the same set of years. OSIRIS ozone sensitivity from 2009-2015 show a similar peak value at 35 km, but are lower otherwise, and even insignificant from 40 to 55 km. As with the correlation coefficient, the sensitivity of ozone to variations in solar flux was higher in studies using data from solar cycles 21 and 22. The maximum of solar cycle 23 had fewer sunspots than the maxima of cycles 21 and 22, and cycle 24 has had fewer sunspots than cycle 23. Based on this observed trend, the ozone sensitivity to variations in solar flux is lower when solar activity is lower. Dikty et al. (2010) also found a greater ozone sensitivity during solar maximum years than during solar minimum years which supports this conclusion. The change in OSIRIS ozone from solar minimum to solar maximum was estimated to be 3.5% at 35.5 km.

The inclusion of the temperature effect on ozone in the regression model used to find the ozone sensitivity increased the correlation between the regression model and the data from 0.20 to 0.53. This demonstrates that the effect of solar variability on ozone cannot be considered in isolation. Including a temperature term in the model makes the ozone sensitivity to UV variations larger, so ignoring temperature in the correlation analysis means

the observed effect of changes in solar flux on ozone concentration is smaller than it could be, at least above 35 km where ozone and temperature are highly anti-correlated.

The similarity between the OSIRIS results and those from SCIAMACHY provides verification of the results in Dikty et al. (2010) and validates of the usage of OSIRIS ozone data products for this type of study. The long OSIRIS time series showed that the effect of solar irradiance on ozone was stronger during the last half of solar cycle 23 than during the first half of solar cycle 24. OSIRIS is still in operation and solar cycle 24 is nearly at an end so it will soon be possible to see how ozone varies over the course of a complete solar cycle from a single instrument. It would also be interesting to use the merged SAGE-OSIRIS-OMPS ozone data set, covering from 1984 to 2016, to get better estimates of the ozone variation over multiple solar cycles.

A future area of research is to model the relationship between odd oxygen (O_3+O), temperature, and solar flux in the stratosphere to gain a better understanding of the observed results. Ozone and atomic oxygen are highly coupled and it is the production of odd oxygen, not just ozone, that depends on the photolysis of molecular oxygen. It is possible to write continuity equations relating variations in the production rate of O_2 to variations in the concentration of odd oxygen at different altitudes. By using OSIRIS ozone concentrations as an input it would be possible to calculate the expected response of odd oxygen or ozone to changes in solar flux based on known chemical reaction rates. The outputs of this model would provide greater understanding of the observed response of ozone to changes in solar flux at different altitudes.

Another interesting thing to look at is the effect of sudden increases or decreases in solar UV flux on ozone. Sudden decreases in solar irradiance, perhaps caused by a large sunspot coming into view of the Earth, could be used in an epoch analysis as an additional way to determine the average ozone response to changes in solar flux.

The effect of solar irradiance on OSIRIS aerosol data is less clear than its effect on ozone. The signal analysis is contaminated by volcanic eruptions at lower altitudes and by large variations in the aerosol extinction anomaly at higher altitudes. The extinction is anti-correlated with Mg II at most altitudes, and has a negative response to changes in solar flux from 23 to 31 km.

Forbush decreases were not found to have a significant effect on the OSIRIS aerosol extinction. A marginally significant decrease in the OSIRIS Ångstrom exponent was found at a few altitudes, however the day of the decrease varied relative to the FD and sometimes even occurred before the FD.

Overall, the OSIRIS aerosol data products are challenging to use for studying the effect of solar irradiance on stratospheric aerosols unless the much stronger volcanic signals can be removed. The null result in the FD study agrees with many recent works showing that GCR do not have an observable effect on particle nucleation, however it is unclear whether or not the OSIRIS result is implying this connection does not exist or due to difficulties with the data. Further investigation is required.

References

Alanko, K., Usoskin, I., Mursula, K., & Kovalstov, G. (2003). Heliospheric modulation strength: Effective neutron monitor energy. *Advances in Space Research*, *32*(4), 615–620.

Baldwin, M. P., Gray, L. J., Dunkerton, T. J., Hamilton, K., Haynes, P. H., Randel, W. J., Holton, J. R., Alexander, M. J., Hirota, I., Horinouchi, T., Jones, D. B. A., Kinnersley, J. S., Marquardt, C., Sato, K., & Takahashi, M. (2001). The quasi-biennial oscillation. *Reviews of Geophysics*, *39*(21), 179–229. doi:10.1029/1999RG000073

Bertello, L., Ulrich, R., & Boyden, J. (2010). The Mount Wilson Ca II K plage index time series. *Solar Physics*, *264*, 31–44.

Bossay, S., Bekki, S., Marchand, M., Poulain, V., & Toumi, R. (2015). Sensitivity of tropical stratospheric ozone to rotational UV variations estimated from UARS and Aura MLS observations during the declining phases of solar cycles 22 and 23. *Joural of Atmospheric and Solar-Terrestrial Physics*, *130*(131), 96–111.

Bourassa, A. E., Degenstein, D. A., & Llewellyn, E. J. (2008). SASKTRAN: A spherical geometry radiative transfer code for efficient estimation of limb scattered sunlight. *Journal of Quantitative Spectroscopy and Radiative Transfer*, *109*(1), 52–73.

Bourassa, A. E., Degenstein, D. A., Randel, W. J., Zawodny, J. M., Kyölä, E., McLinden, C. A., Sioris, C. E., & Roth, C. Z. (2014). Trends in stratospheric ozone derived from merged SAGE II and Odin-OSIRIS satellite observations. *Atmospheric Chemistry and Physics*, *14*, 6983–6994. doi:10.5194/acp-14-6983-2014

Brasseur, G. P., & Solomon, S. (2005). *Aeronomy of the middle atmosphere* (3rd ed.). Atmospheric and Oceanic Sciences Library. Dordrecht, The Netherlands: Springer.

Brewer, A. W. (1949). Evidence for a world circulation provided by the measurements of helium and water vapour distribution in the stratosphere. *Quarterly Journal of the Royal Meteorological Society*, *75*(326), 351–363.

Chapman, S. (1930). A theory of upper-atmospheric ozone. *Memoirs of the Royal Meteorological Society*, *3*(26), 103–125.

Dee, D. P., Uppala, S. M., Simmons, A. J., Berrisford, P., Poli, P., Kobayashi, S., Andrae, U., Balmaseda, M. A., Balsamo, G., Bauer, P., Bechtold, P., Beljaars, A. C. M., van de Berg, L., Bidlot, J., Bormann, N., Delsol, C., Dragani, R., Fuentes, M., Geer, A. J., Haimberger, L., Healy, S. B., Hersbach, H., Hólm, E. V., Isaksen, L., Kållberg, P., Köhler, M., Matricardi, M., McNally, A. P., Monge-Sanz, B. M., Morcrette, J.-J.,

Park, B.-K., Peubey, C., de Rosnay, P., Tavolato, C., Thépaut, J.-N., & Vitart, F. (2011). The ERA-Interim reanalysis: Configuration and performance of the data assimilation system. *Quarterly Journal of the Royal Meteorological Society*, *137*(656), 553–597. doi:10.1002/qj.828

Devore, J. L., & Berk, K. N. (2012). *Modern mathematical statistics with applications* (2nd ed.). New York: Springer.

Dikty, S., Weber, M., von Savigny, C., Sonkaew, T., Rozanov, A., & Burrows, J. P. (2010). Modulations of the 27 day solar rotation signal in stratospheric ozone from Scanning Imaging Absorption Spectrometer for Atmospheric Cartography (SCIAMACHY). *Journal of Geophysical Research*, *115*(D00I15).

Dobson, G. M. B. (1956). Origin and distribution of the polyatomic molecules in the atmosphere. *Proceedings of the Royal Society of London. Series A, Mathematical and Physical Sciences*, *236*(1205), 187–193.

Donnelly, R. F., White, O. R., & Livingston, W. C. (1994). The solar Ca II K index and the Mg II core-to-wing ratio. *Solar Physics*, *152*(1), 69–76.

Egorova, T., Rozanov, E., Manzini, E., Haberreiter, M., Schmutz, W., Zubov, V., & Peter, T. (2004). Chemical and dynamical response to the 11-year variability of the solar irradiance simulated with a chemistry-climate model. *Geophysical Research Letters*, *31*(6). doi:10.1029/2003GL019294

Finger, F. G., Nagatani, R. M., Gelman, M. E., Long, C. S., & Miller, A. J. (1995). Consistency between variations of ozone and temperature in the stratosphere. *Geophysical Research Letters*, *22*(24), 3477–3480.

Fioletov, V. E. (2009). Estimating the 27-day and 11-year solar cycle variations in tropical upper stratospheric ozone. *Journal of Geophysical Research*, *114*(D02302).

Forbush, S. E. (1938). On cosmic-ray effects associated with magnetic storms. *Terrestrial Magnetism and Atmospheric Electricity*, *43*(3), 203–218. doi:10.1029/TE043i003p00203

Foukal, P., Fröhlich, C., Spruit, H., & Wigley, T. M. L. (2006). Variations in solar luminosity and their effect on the earth's climate. *Nature*, *443*, 161–166.

Fröhlich, C. (2013). Total solar irradiance: What have we learned from the last three cycles and the recent minimum? *Space Science Review*, *176*, 237–252.

Fröhlich, C., & Lean, J. (2004). Solar radiative output and its variability: Evidence and mechanisms. *The Astronomy and Astrophysics Review*, *12*, 273–320.

Gray, L. J., Rumbold, S. T., & Shine, K. P. (2009). Stratospheric temperature and radiative forcing response to 11-year solar cycle changes in irradiance and ozone. *Journal of the Atmospheric Sciences*, *66*, 2402–2416. doi:10.1175/2009JAS2866.1

Harrison, R., & Stephenson, D. (2006). Empirical evidence for a nonlinear effect of galactic cosmic rays on clouds. *Proceedings of the Royal Society of London A: Mathematical, Physical and Engineering Sciences*, *462*(2068), 1221–1233. doi:10.1098/rspa.2005.1628

Heath, D. F., & Schlesinger, B. M. (1986). The Mg 280 nm doublet as a monitor of changes in solar ultraviolet irradiance. *Journal of Geophysical Research*, *91*(D8), 8672–8682.

Heber, B., Fichtner, H., & Scherer, K. (2006). Solar and heliospheric modulation of galactic cosmic rays. In Y. Calisesi, R.-M. Bonnet, L. Gray, J. Langen, & M. Lockwood (Eds.), *Solar variability and planetary climates* (Chap. 1, pp. 81–93). The Netherlands: Springer.

Hinds, W. C. (1999). *Aerosol technology* (2nd ed.). New York: John Wiley and Sons.

Hood, L. L. (1986). Coupled stratospheric ozone and temperature responses to short-term changes in solar ultraviolet flux: An analysis of Nimbus 7 SBUV and SAMS data. *Journal of Geophysical Research*, *91*(D4), 5264–5276.

Hood, L. L., & Zhou, S. (1998). Stratospheric effects of 27-day solar ultraviolet variations: An analysis of UARS MLS ozone and temperature data. *Journal of Geophysical Research*, *103*(D3), 3629–3638.

IZMIRAN. (2016). Moscow neutron monitor. Retrieved from http://cr0.izmiran.ru/mosc/main.htm

IZMIRAN. (2018). Catalogue of the Forbush-effects and interplanetary disturbances. Retrieved from http://spaceweather.izmiran.ru/eng/dbs.html

Junge, C. E., Chagnon, C. W., & Manson, J. E. (1961). Stratospheric aerosols. *Journal of Meteorology*, *18*, 81–108.

Kirkby, J. (2007). Cosmic rays and climate. *Surveys in Geophysics*, *28*(5), 333–375. doi:10.1007/s10712-008-9030-6

Koskinen, H. E. J. (2011). *Physics of space storms* (1st ed.). Heidelberg: Springer.

Kremser, S., Thomason, L. W., Hobe, M., Hermann, M., Deshler, T., Timmreck, C., Toohey, M., Stenke, A., Schwarz, J. P., Weigel, R., Fueglistaler, S., Prata, F. J., Vernier, J.-P., Schlager, H., Barnes, J. E., Antuña-Marrero, J.-C., Fairlie, D., Palm, M., Mahieu, E., Notholt, J., Rex, M., Bingen, C., Vanhellemont, F., Bourassa, A., Plane, J. M. C., Klocke, D., Carn, S. A., Clarisse, L., Trickl, T., Neely, R., James, A. D., Rieger, L., Wilson, J. C., & Meland, B. (2016). Stratospheric aerosol—Observations, processes, and impact on climate. *Reviews of Geophysics*, *54*(2), 278–335. doi:10.1002/2015RG000511

Krissansen-Totton, J., & Davies, R. (2013). Investigation of cosmic ray–cloud connections using MISR. *Geophysical Research Letters*, *40*(19), 5240–5245. doi:10.1002/grl.50996

Kristjánsson, J. E., Stjern, C. W., Stordal, F., Fjæraa, A. M., Myhre, G., & Jónasson, K. (2008). Cosmic rays, cloud condensation nuclei and clouds – a reassessment using MODIS data. *Atmospheric Chemistry and Physics*, *8*(24), 7373–7387. doi:10.5194/acp-8-7373-2008

Laken, B., Kniveton, D., & Wolfendale, A. (2011). Forbush decreases, solar irradiance variations, and anomalous cloud changes. *Journal of Geophysical Research: Atmospheres*, *116*(D9). D09201. doi:10.1029/2010JD014900

Laken, B., & Calogović, J. (2013). Composite analysis with Monte Carlo methods: An example with cosmic rays and clouds. *Journal of Space Weather and Space Climate*, *3*, A29. doi:10.1051/swsc/2013051

Lean, J. (1987). Solar ultraviolet irradiance variation: A review. *Journal of Geophysical Research*, *92*, 839–868.

Liou, K. N. (2002). *An introduction to atmospheric radiation* (2nd ed.). International Geophysics Series. San Diego, California: Academic Press.

Llewellyn, E., Lloyd, N. D., Degenstein, D. A., Gattinger, R. L., Petelina, S. V., Bourassa, A. E., Wiensz, J. T., Ivanov, E. V., McDade, I. C., Solheim, B. H., McConnell, J. C., Haley, C. S., von Savigny, C., Sioris, C. E., McLinden, C. A., Griffioen, E., Kaminski, J., Evans, W. F. J., Puckrin, E., Strong, K., Wehrle, V., Hum, R. H., Kendall, D. J. W., Matsushita, J., Murtagh, D. P., Brohede, S., Stegman, J., Witt, G., Barnes, G., Payne, W. F., Piche, L., Smith, K., Warshaw, G., Deslauniers, D. L., Marchand, P., Richardson, E. H., King, R. A., Wevers, I., McCreath, W., Kyrola, E., Oikarinen, L., Leppelmeier, G. W., Auvinen, H., Megie, G., Hauchecorne, A., Lefevre, F., de La Noe, J., Ricaud, P., Frisk, U., Sjoberg, F., von Scheele, F., & Nordh, L. (2004). The OSIRIS instrument on the Odin spacecraft. *Canadian Journal of Physics*, *82*, 411–422. doi:10.1139/p04-005

Marsh, N., & Svensmark, H. (2000). Low cloud properties influenced by cosmic rays. *Physics Review Letters*, *85*, 5004–5007. doi:10.1103/PhysRevLett.85.5004

McCormack, J. P., & Hood, L. L. (1996). Apparent solar cycle variations of upper stratospheric ozone and temperature: Latitude and seasonal dependences. *Journal of Geophysical Research*, *101*(D15), 20933–20944.

McIntosh, S. W., Wang, X., Leamon, R. J., Davey, A. R., Howe, R., Krista, L. D., Malanushenko, A. V., Markel, R. S., Cirtain, J. W., Gurman, J. B., Pesnell, W. D., & Thompson, M. J. (2014). Deciphering solar magnetic activity. I. on the relationship between the sunspot cycle and the evolution of small magnetic features. *The Astrophysical Journal*, *792*(1), 12.

Mlynczak, M. G., & Solomon, S. (1991). Middle atmsophere heating by exothermic chemical reactions involving odd-hydrogen species. *Geophysical Research Letters*, *18*(1), 37–40.

Nandy, D., Muñoz-Jaramillo, A., & Martens, P. C. H. (2011). The unusual minimum of sunspot cycle 23 caused by meridional plasma flow variations. *Nature*, *471*(90).

Petty, G. W. (2006). *A first course in atmospheric radiation* (2nd ed.). Madison, Wisconsin: Sundog Publishing.

Press, W. H. (1988). *Numerical recipes in C : The art of scientific computing*. Cambridge [Cambridgeshire] ; New York: Cambridge University Press.

Radick, R. R. (2004). Long-term solar variability: Evolutionary time scales. In *Solar variability and its effects on climate* (pp. 5–14). doi:10.1029/141GM02

Rogerson, P. A. (2015). *Statistical methods for geography* (4th ed.). London: SAGE.

Schröder, K.-P., Mittag, M., Schmitt, J. H. M. M., Jack, D., Hempelmann, A., & González-Pérez, J. N. (2017). Carrington cycle 24: The solar chromospheric emission in a historical and stellar perspective. *Monthly Notices of the Royal Astronomical Society*, *470*(1), 276–282. doi:10.1093/mnras/stx1147

Seinfeld, J. H., & Pandis, S. N. (2006). *Atmospheric chemistry and physics: From air pollution to climate change* (2nd ed.). Hoboken, New Jersey: John Wiley and Sons.

Skupin, J., Weber, M., Bovensmann, H., & Burrows, J. P. (2004). *The Mg II solar activity proxy indicator derived from GOME and SCIAMACHY*. ESA Publications Division.

Smart, D., & Shea, M. A. (2005). A review of geomagnetic cutoff rigidities for earth-orbiting spacecraft. *Advances in Space Research*, *36*, 2012–2020. doi:10.1016/j.asr.2004.09.015

Snow, M., Weber, M., Machol, J., Viereck, R., & Richard, E. (2014). Comparison of magnesium II core-to-wing ratio observations during solar minimum 23/24. *Journal Space Weather Space Climate*, *4*(A06).

Soukharev, B. E., & Hood, L. L. (2006). Solar cycle variations of stratospheric ozone: Multiple regression analysis of long-term satellite data sets and comparisons with models. *Journal of Geophysical Research*, *111*(D20314).

Svensmark, H., & Friis-Christensen, E. (1997). Variation of cosmic ray flux and global cloud coverage- A missing link in solar-climate relationships. *Journal of Atmospheric and Solar-Terrestrial Physics*, *59*(11), 1225–1232.

Svensmark, J., Enghoff, M., Shaviv, N., & Svensmark, H. (2016). The response of clouds and aerosols to cosmic ray decreases. *Journal of Geophysical Research: Space Physics*, *121*, 8152–8181. doi:10.1002/2016JA022689

Tapping, K. F. (2013). The 10.7 cm solar radio flux. *Space Weather*, *10*, 394–406.

Thomas, S. R., Owens, M. J., & Lockwood, M. (2014). Galactic cosmic rays in the heliosphere. *Astronomy and Geophysics*, *55*(5), 5.23–5.24. doi:10.1093/astrogeo/atu214

Thompson, M. J., Toomre, J., Anderson, E. R., Antia, H. M., Berthomieu, G., Burtonclay, D., Chitre, S. M., Christensen-Dalsgaard, J., Corbard, T., DeRosa, M., Genovese, C. R., Gough, D. O., Haber, D. A., Harvey, J. W., Hill, F., Howe, R., Korzennik, S. G., Kosovichev, A. G., Leibacher, J. W., Pijpers, F. P., Provost, J., Rhodes, E. J., Schou, J., Sekii, T., Stark, P. B., & Wilson, P. R. (1996). Differential rotation and dynamics of the solar interior. *Science*, *272*(5266), 1300–1305. doi:10.1126/science.272.5266.1300

Torrence, C., & Compo, G. P. (1998). A practical guide to wavelet analysis. *Bulletin of the American Meteorological Society*, *79*(1), 61–78.

Uppala, S., Kallberg, P., Simmons, A., Andrae, U., Da Costa Bechtold, V., Fiorino, M., Gibson, J., Haseler, J., Hernandez, A., Kelly, G., Li, X., Onogi, K., Saarinen, S., Sokka, N., Allan, R., Andersson, E., Arpe, K., Balmaseda, M., Beljaars, A., Van De Berg, L., Bidlot, J., Bormann, N., Caires, S., Chevallier, F., Dethof, A., Dragosavac, M., Fisher, M., Fuentes, M., Holme, E., Hoskins, B., Isaksen, L., Janssen, P., Jenne, R.,

McNally, A., Mahfouf, J., Morcrette, J.-J., Rayner, N., Saunders, R., Simon, P., Sterl, A., Trenberth, K., Untch, A., Vasiljevic, D., Viterbo, P., & Woollen, J. (2005). The ERA-40 re-analysis. *Quarterly Journal of the Royal Meteorological Society*, *131*(612), 2961–3012. doi:10.1256/qj.04.176

Weber, M. (1999). Solar activity during solar cycle 23 monitored by GOME. *Proc. European Symposium on Atmospheric Measurements from Space*, 18–22.

Zhou, S., Miller, A., & Hood, L. (2000). A partial correlation analysis of the stratospheric ozone response to 27-day solar UV variations with temperature effect removed. *Journal of Geophysical Research*, *105*(D4), 4491–4500.